Thèse n° 8564

Fatigue of reinforced UHPFRC members and monitoring of fatigue action effects on bridges

Présentée le 20 mai 2021

Faculté de l'environnement naturel, architectural et construit
Laboratoire de maintenance, construction et sécurité des ouvrages
Programme doctoral en génie civil et environnement

pour l'obtention du grade de Docteur ès Sciences

par

Bartłomiej Wojciech SAWICKI

Acceptée sur proposition du jury

Prof. T. Keller, président du jury
Prof. E. Brühwiler, directeur de thèse
Dr F. Toutlemonde, rapporteur
Prof. J. Bien, rapporteur
Prof. E. Chatzi, rapporteuse

École
polytechnique
fédérale
de Lausanne

2021

Acknowledgement

The four-year-long journey through my doctoral studies was an exciting and challenging one.

First and foremost, I would like to express my gratitude to professor Eugen Brühwiler. He did not merely provide me with all necessary tools, resources and case studies indispensable for this research. More importantly, prof. Brühwiler restored my faith in importance of civil engineering matter and helped me in rediscovering the creativity and potential which can benefit our discipline. He has shown me the new world of possibilities and gave motivation for further work.

The last four years would not have been so interesting without the INFRASTAR European Marie Skłodowska-Curie project. It was thanks to the scientific coordinator Dr Odile Abraham and the project manager Dr Hakim Ferria that INFRASTAR run so smoothly and was definitely an added value to my doctoral studies. I would like to acknowledge all the supervisors, advisors and fellows, especially ones with whom I have had a chance to cooperate: prof. John Sørensen, Mariia Nesterova and Antoine Bassil. Many thanks to EIFFAGE team for hosting me for three months in Paris, especially to Christian Clergue and Ludovic Picard.

MCS lab was a great place to work thanks to its team. I'd like to express my gratitude to: dr Emmanuel Denarié for providing me with knowledge on UHPFRC and spending his time on multiple fruitful discussions; Florence Grandjean for taking care of all administrative stuff during many international trips and being always helpful; Christophe Loraux for teaching me how to live and work in Switzerland; Xiujiang Shen aka Gianni for sharing office, lab, meals and trips with me; Md Hafiz and Amir Hajiesmaeili for discussing cultural differences and politics; Philippe Schiltz and Numa Bertola for deliberations about peculiarities of engineering over glass of beer in SAT; and to Jian Zhan and all the Chinese visitors through all these years for introducing to me the culture of the Middle Kingdom which I hope to visit one day.

An important part of my research took part in the laboratory. Thankfully, Sylvain Demierre and Gilles Guignet were always there and willing to help. Many thanks to the team of Structural Engineering Group technicians for friendly atmosphere, especially to Frédérique, Gérald, Serge and Armin. Un gros merci à toute l'équipe!

Finally, I wold like to thank all my colleagues, friends from Lausanne and Warsaw, and family for their support during these four difficult years. A zwłaszcza dziękuję mojemu Kotkowi za cierpliwość, kocham Cię skarbie.

Foreword

In January 2017, Bartłomiej (Bartek) Sawicki joined my research group as a doctoral student (ESR) of the ITN (Innovative Training Network) Project "Infrastar" (Marie Skłodowska-Curie grant agreement No 676139), a project within the European Union's Horizon 2020 research and innovation program.

The objective of his doctoral research was to develop knowledge and methods to prevent fatigue failure of bridges. To achieve this goal, Bartek Sawicki investigated aspects from both the demand (S) and resistance (R) sides. The S-part focuses on the reduction of uncertainties by means of structural monitoring of fatigue action effects, i.e. measurement of deformation of bridge elements, to learn more about the effective solicitation of bridges under daily road traffic. The R-part of his thesis concentrates on the structural response and fatigue resistance of UHPFRC (Ultra-High Performance Fiber Reinforced Cementitious Composite material), a novel type of building material with a large application potential. Results of the R-part are already applied to both new UHPFRC structures and concrete bridges strengthened with UHPFRC, in particular with respect to fatigue resistance.

In both laboratory experiments and structural monitoring campaigns, Bartek Sawicki gained novel knowledge in UHPFFRC material and bridge behaviour. Developments and findings in analytical and numerical modelling relied on the adaptation and extension of existing methods, solving problems that were not tackled before.

With his doctoral thesis, Bartek Sawicki provides the proof of his capabilities to conduct a scientific study and to solve complex scientific questions by applying scientific methods. Overall, his thesis delivers novel scientific findings useful for the implementation in structural engineering. The high value of Bartek Sawicki's research work is also evident from his publications record.

Bartek has shown passion for research and willingness to cooperation. Importantly, his collaboration with other doctoral students (ESRs) from foreign universities involved in the EU ITN-"Infrastar" research project through secondments, lead to true synergy, demonstrating the importance of exchanges among researchers and their institutions.

In the name of the whole MCS Team, I thank him for his constant and thorough investment to the thesis topic as well as for his professional skills and personal qualities.

Lausanne, December 2020 Professor Eugen Brühwiler

Abstract

The objective of this thesis is to develop knowledge and methods to prevent fatigue failure of bridges. The Fatigue Limit State is investigated from both the demand (S) and resistance (R) side.

The S-part focuses on reduction of uncertainties through monitoring of fatigue action effects:

- Analysis of 28-month-long high-frequency monitoring of a slab's portion of a prestressed concrete road bridge demonstrated that the stress ranges due to traffic loading and temperature action can be of similar magnitudes. Furthermore, they should be treated together as their combination can be fatigue-relevant.

- The monitoring duration influences the reliability of results, which are further extrapolated to obtain the Cumulative Fatigue Damage for the total service duration of a structure. To quantify the associated uncertainty, the monitoring duration-dependent Cumulative Damage correction Factor (CDF) was calibrated. The minimum recommended monitoring duration is 100 days, and for this observation period the correction factor γ_{CDF}=4 for massive structures and γ_{CDF}=20 for temperature-sensitive elements should be applied. After one year of monitoring γ_{CDF} can be reduced to 1.3 and 2.5 respectively. The correction factor is significantly smaller than the one obtained with method suggested by Eurocode, leading to γ_{CDF}=20.

The R-part of this thesis concentrates on a structural response and fatigue resistance of reinforced UHPFRC (R-UHPFRC) and was based on experimental testing of full-scale R-UHPFRC beams. The results can be applied to both new structures and elements strengthened with R-UHPFRC layer:

- It is demonstrated that after loading-unloading cycles, due to modified mechanical properties of a part of UHPFRC element which entered into strain-hardening domain, the distribution of stress in the cross-section is re-arranged, influencing the global structural response. Two important fatigue-relevant conclusions are drawn: I) the stress range in the rebar is much lower than calculated using initial material properties; and II) the portion of UHPFRC is subjected to tensile-compressive rather than to tensile-tensile fatigue stress.

- The fatigue phenomenon of R-UHPFRC member is observed in detail using Distributed Fibre Optics sensing. The strain variation during the fatigue process in both UHPFRC and rebar remained stable for most of the experiment. The rapid increase of strain range occurred at around 90% of the test duration. During the last 1% of the fatigue test, the increase of strain in the reinforcement bar took place while the increase of the beam deflection range ensued during last 1‰ of test duration. Importantly, the failure of reinforcement bar is identical with failure of the member.

- Fourteen beams were exposed to constant amplitude fatigue in four-point bending. It was the largest experimental campaign on R-UHPFRC ever executed. Two-level fatigue verification was proposed:

I) global verification using normalized minimum and maximum load levels and the modified Goodman diagram, contrary to previous methods based on the maximum load and load range; and II) local verification of stress-range in reinforcement bar using the standard S-N curves.

The research work presented in this thesis brings new knowledge in both fatigue demand (S) and resistance (R) of both R-UHPFRC structures and reinforced concrete structures strengthened using UHPFRC. More economic solutions for structures can be obtained, leading to both financial and environmental savings.

Keywords

Fatigue, UHPFRC, monitoring, experimental testing, bridges, concrete

Résumé

L'objectif de cette thèse est de développer des connaissances et des méthodes pour prévenir la rupture en fatigue des ponts. L'État Limite de Fatigue est étudié du côté de la sollicitation (S) et de la résistance (R).

La partie S se concentre sur la réduction des incertitudes des effets de l'action grâce à une campagne de mesures :

- L'analyse d'une surveillance pendant 28 mois d'une partie de la dalle d'un pont routier en béton précontraint a démontré que les plages de contraintes dues aux charges de trafic et à l'action de la température peuvent être d'une ampleur similaire. Cependant, elles doivent être traitées simultanément.

- La durée de la surveillance influence la fiabilité des résultats puisqu'ils sont extrapolés pour obtenir les dommages cumulés dus à la fatigue sur la durée totale de service d'une structure. Pour quantifier l'incertitude associée, un facteur de correction des dommages cumulés (γ_{CDF}), dépendant de la durée de surveillance, a été calibré. La durée minimale recommandée d'une campagne de mesures est de 100 jours. Pour cette période d'observation, γ_{CDF}=4 pour les structures massives et γ_{CDF}=20 pour les éléments sensibles à la température doit être utilisé. Après un an, γ_{CDF} peut être réduit à 1,3 et 2,5 respectivement.

La partie R se concentre sur la réponse structurelle et la résistance à la fatigue du CFUP armé et ont été basée sur des essais expérimentaux. Les résultats peuvent être appliqués à la fois à de nouvelles structures et à des éléments renforcés avec une couche de CFUP :

- Il est démontré qu'après les cycles de chargement-déchargement, à cause de la modification de propriétés mécaniques d'une partie de l'élément qui est entrée dans le domaine de l'écrouissage, la distribution des contraintes est réorganisée. Deux conclusions importantes sont tirées de cette étude : I) la plage de contraintes dans la barre d'armature est beaucoup plus faible que celle calculée à partir des propriétés initiales du matériau ; et II) la partie en CFUP est soumise à une contrainte de traction-compression plutôt qu'à une contrainte de fatigue en traction-traction.

- Le phénomène de fatigue de la poutre en CFUP est observé précisément à l'aide de fibres optiques pour mesures distribuées. La variation des contraintes pendant le processus de fatigue, tant dans CFUP que dans les barres d'armature, est restée stable pendant la majorité de l'expérience. L'augmentation rapide de la plage de contraintes s'est produite à environ 90 % de la durée de l'essai. Pendant le dernier 1% l'augmentation de la contrainte dans la barre d'armature a eu lieu tandis que l'augmentation de la plage de déflection de la poutre s'est produite uniquement pendant le dernier 1‰ de la durée de l'essai.

- Quatorze poutres ont été exposées à une fatigue d'amplitude constante via une flexion en quatre points. Une vérification de la fatigue à deux niveaux a été proposée : I) une vérification globale en

utilisant les niveaux de charges minimum et maximum normalisés ; et II) une vérification locale de la plage de contraintes dans les barres d'armatures en utilisant les courbes S-N standard.

Les travaux de recherche présentés dans cette thèse apportent de nouvelles connaissances à la fois sur la sollicitation (S) et la résistance (R) à la fatigue des structures en CFUP et des structures en béton armé renforcées à l'aide de CFUP. Des solutions plus économiques pour les structures peuvent être obtenues, réduisant les coûts de constructions et les impacts environnementaux.

Mots-clés

Fatigue, CFUP, BFUP, surveillance, essais expérimentaux, ponts, béton

Streszczenie

Celem tej pracy jest rozwój wiedzy i metod zapobiegania zmęczeniowym awariom mostów. Stan graniczny zmęczenia jest badany zarówno od strony efektów oddziaływania (S), jak i nośności (R).

Część S skoncentrowana jest na zmniejszeniu niepewności poprzez bezpośrednie monitorowanie efektów oddziaływania obciążenia zmęczeniowego:

- Analiza 28-miesięcznego ciągłego monitoringu o wysokiej częstotliwości części płyty mostu drogowego z betonu sprężonego wykazała, że zakresy naprężeń wywołanych obciążeniem ruchem drogowym oraz odpowiedzią konstrukcji na zmianę temperatury mogą być podobnej wielkości. Co więcej, powinny one być rozpatrywane łącznie, ponieważ ich kombinacja może mieć znaczenie zmęczeniowe.

- Czas trwania monitoringu wpływa na wiarygodność wyników, które są następnie ekstrapolowane w celu uzyskania kumulatywnego zużycia zmęczeniowego podczas całego okresu użytkowania konstrukcji. W celu ilościowego określenia związanej z tym niepewności pomiarowej, skalibrowano współczynnik kumulatywnego zużycia zmęczeniowego (γ_{CDF}) zależny od czasu trwania monitoringu. Minimalny zalecany czas trwania wynosi 100 dni i dla tego okresu obserwacji należy zastosować współczynnik korekcyjny γ_{CDF} =4 dla masywnych konstrukcji oraz γ_{CDF} =20 dla elementów wrażliwych na temperaturę. Po roku monitorowania γ_{CDF} może być zredukowany odpowiednio do wartości 1,3 i 2,5. Współczynnik ten jest znacznie mniejszy niż uzyskany metodą sugerowaną przez Eurokod, która prowadzi do γ_{CDF} =20.

Część R tej pracy skoncentrowana jest na wytrzymałości zmęczeniowej oraz odpowiedzi konstrukcji wykonanej z UHPFRC zbrojonego stalowymi prętami (R-UHPFRC) i została oparta na badaniach eksperymentalnych pełnowymiarowych belek. Wyniki te mogą być zastosowane zarówno do nowych konstrukcji, jak i elementów wzmocnionych warstwą R-UHPFRC:

- Wykazano, że po cyklach obciążania-odciążania, ze względu na modyfikację właściwości mechanicznych UHPFRC w części elementu która weszła w fazę umacniania poprzez odkształcanie, rozkład naprężeń w przekroju poprzecznym ulega zmianie, wpływając na globalną odpowiedź konstrukcji. Wyciągnięto dwa ważne wnioski istotne z punktu widzenia wytrzymałości zmęczeniowej: I) zakres naprężeń w prętach zbrojeniowych jest znacznie mniejszy niż obliczony na podstawie wyjściowych właściwości materiału; oraz II) część elementu UHPFRC poddawana jest cyklom zmęczeniowym w rozciąganiu-ściskaniu, a nie w rozciąganiu-rozciąganiu.

- Mechanizm zużycia zmęczeniowego elementu R-UHPFRC został szczegółowo zaobserwowany za pomocą geometrycznie ciągłej światłowodowej techniki pomiarowej (Distributed Fibre Optics Sensing). Zakres odkształceń podczas zużycia zmęczeniowego zarówno w UHPFRC jak i prętach zbrojeniowych pozostawał stabilny przez większą część badania. Gwałtowny wzrost zakresu odkształceń wystąpił po około 90% czasu trwania próby zmęczeniowej. Podczas ostatniego 1%

nastąpił wzrost naprężenia w prętach zbrojeniowych, podczas gdy wzrost zakresu ugięcia belki nastąpił dopiero podczas ostatniego 1 ‰ czasu trwania próby. Co ważne, zerwanie pręta ze względu na zużycie zmęczeniowe jest równoznaczne ze zniszczeniem belki.

- Czternaście belek zostało poddanych testom zmęczeniowym o stałej amplitudzie obciążeń przy zginaniu czteropunktowym. Była to największa kampania eksperymentalna na R-UHPFRC jaką kiedykolwiek przeprowadzono. Zaproponowano dwustopniową ocenę wytrzymałości zmęczeniowej: I) weryfikację globalną przy użyciu znormalizowanych minimalnych i maksymalnych poziomów obciążenia oraz zmodyfikowanego wykresu Goodmana, w przeciwieństwie do poprzednich metod opartych na maksymalnym obciążeniu i zakresie obciążeń; oraz II) weryfikację lokalną zakresu naprężeń w prętach zbrojeniowych przy użyciu standardowych wykresów S-N.

Praca badawcza przedstawiona w niniejszej rozprawie dostarcza nowej wiedzy zarówno w zakresie efektów odziaływania obciążeń zmęczeniowych (S), jak i odporności na zmęczenie (R) elementów wykonanych w technologii R-UHPFRC oraz konstrukcji żelbetowych wzmocnionych przy użyciu UHPFRC. Dzięki temu możliwe jest uzyskanie bardziej ekonomicznych rozwiązań konstrukcyjnych, prowadzących zarówno do oszczędności finansowych jak i korzyści dla środowiska.

Słowa kluczowe

Zmęczenie, UHPFRC, BUWW, monitoring, badania eksperymentalne, mosty, beton, Inżynierskie Kompozyty Fibrocementowe, IKF

Contents

List of Figures

List of Tables

List of Equations

Chapter 1 Introduction

On motivations of this work and its layout.

In Western Europe[1], the USA[2], Korea or Japan ageing[3] and poorly maintained infrastructure causes more and more problems due to corrosion and lack of sufficient mechanical resistance. Arguably, the most well-known, but not isolated case of collapse of the bridge within last few years is the catastrophe of Morandi Bridge in Genoa, Italy.

On the other hand, bridges are the most expensive part of the infrastructure chain, and none of the countries can afford total re-construction of all of them both from economic and ecological point of view. The structural and civil engineering sector is responsible for around 40% of the energy use and CO_2 emmisions[4,5], with concrete production alone generating 5% of these emissions and causing sand and gravel to be the most exploited raw materials[6]. Therefore, the resources that we use for the maintenance of structures should be allocated effectively. That is why today we need more effective and efficient ways of verification and, if needed, upgrading of the existing structures. Verification of existing structures is challenging since most of the standards and codes are made for design of new constructions[7]. Upgrading, contrary to strengthening, means that not only the mechanical resistance should be of concern, but also durability, architectural values, etc.[8]; therefore the most modern materials should be used for this task, like the Ultra High Performance Fibre Reinforced Cementitious composites (UHPFRC).

The present research approaches this problem from both sides: demand from structures under fatigue actions and resistance of reinforced UHPFRC (R-UHPFRC) elements under repeated loading. It is shown schematically using the possible workflow during verification and strengthening of structure presented in Figure 1-1. Below, each of the research questions is explained and pinpointed. The main goal of this research is to use the scientific methods to obtain structural engineering solutions, ready to be applied in-situ.

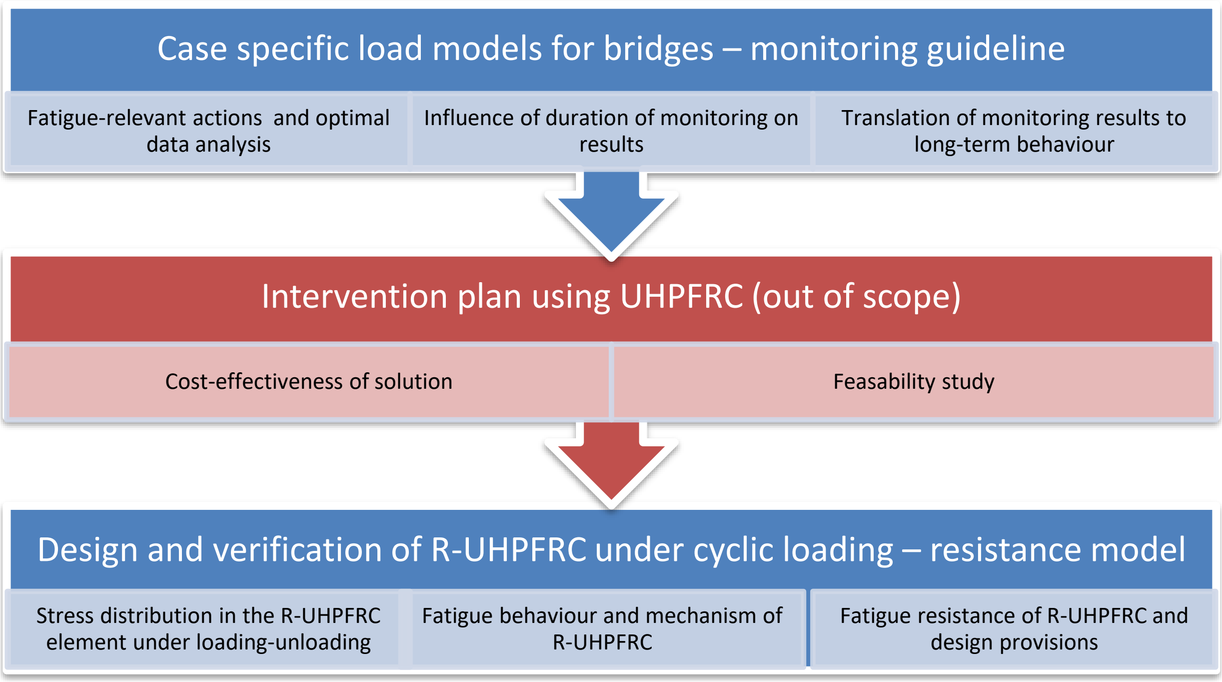

Figure 1-1: Workflow in assessment and upgrading of existing structures.

- **Case specific load models for bridges – monitoring guideline**

  - **Fatigue-relevant actions and optimal data analysis:** the optimal monitoring campaign should be limited only to observation of indicators relevant for the motivation of the campaign. The redundant sensors, data and its analysis should be avoided to limit the overall cost[9]. In case of fatigue, the obvious choice of aim of monitoring are effects of loading due to rail and road traffic. However, the variation of temperature can cause important stress accumulation, especially in massive concrete structures. Are these temperature-induced stresses important from the fatigue point of view? What should be the time window of rainflow analysis for cycle counting to grasp them correctly?

- **Influence of duration of monitoring on results:** the duration of monitoring of action effects influences the results. When the monitoring duration is too short, results may be biased or not representative due to the stochastic nature of actions. What is the nature of this phenomenon in case of road traffic?

- **Translation of monitoring results to long-term behaviour:** for reasons mentioned above, the results of short-term monitoring might not be representative for the whole service duration of the structure. However, on their basis the decisions regarding the following dozens of years need to be drawn. How to translate the short-term observations into long-term conclusions?

- **Design and verification of R-UHPFRC**

  - **Stress distribution in R-UHPFRC element under loading-unloading:** the precise calculation of structural response under given action is crucial for understanding the fatigue mechanism and resistance. Due to nonelastic deformations of UHPFRC under strain-hardening, and because of the perfect bond with reinforcement bar, the stress distribution under loading-unloading action is not obvious. How important is modification of stress distribution under loading-unloading? Is it fatigue-relevant?

  - **Fatigue behaviour and mechanism of R-UHPFRC:** the UHPFRC can contribute significantly to the tensile response of members under bending. Currently, we know how reinforcement and UHPFRC work together under static loading. Some tests have been done on R-UHPFRC in fatigue under direct tension on the small specimens. However, it is still not clear how the UHPFRC and steel reinforcement bars cooperate in tension under bending action with the possibility of strain redistribution. What is the fatigue mechanism of the full-scale member?

  - **Fatigue resistance of R-UHPFRC and proper design**: whether used for strengthening of the existing structure or building of a new one, the R-UHPFRC should not undergo damage, and utmost collapse, due to the fatigue loading. What are the limits that the designer should consider to avoid dangerous situations? What kind of verification should be done?

Outline of the thesis

The following thesis is a continuation and development of two core research topics of the Laboratory for Maintenance and Safety of Structures. The first topic is the response of a structure under real actions imposed on it, predominantly due to the railway and road traffic. Better understanding of the actual deformations and stresses allows for precise verification of existing structures, often with help of the direct monitoring of this response. The current thesis used methods developed in particular by Mark Treacy[10], Christophe Loraux[11] and Vasileios Grigoriou[12].

The second topic is the fatigue response and mechanism of UHPFRC. This relatively novel structural material is useful in rehabilitating, strengthening and upgrading of existing structures. It can be used for new constructions too, reducing the energy and carbon footprint as well as construction cost and time with proper design.

However, it is extremely important to be sure that its application will not lead to new problems in the future. The development of knowledge performed in the current work was possible especially thanks to previous research by Tohru Makita[13], as well as by Christophe Loraux[11], Xiujiang Shen[14] and Andrin Herwig[15].

The part "S", regarding fatigue demands on structure, consists of two chapters.

In **chapter 2** the long-term monitoring of Chillon viaduct is discussed. It helps in answering the research question about **fatigue-relevant actions and optimal data analysis.**

In **chapter 3** the long-term monitoring of Chillon and Crêt de l'Anneau viaducts are analysed using statistical methods. As the two bridges are different from both structural and class-of-road points of view, the findings on the **influence of duration of monitoring on results** and **translation of monitoring results to long-term behaviour** can be generalized.

The part "R" discussing the fatigue resistance of R-UHPFRC consists of three chapters.

In **chapter 4** the inverse analysis methods, non-destructive testing and stress calculation procedures are presented for beams tested under quasi-static loading. Thanks to that, the reference static resistance can be precisely calculated and better understanding of **stress distribution in the R-UHPFRC element under loading-unloading** gained.

In **chapter 5** one of the beams tested in fatigue is discussed in detail. The beam was instrumented with the strain gauges, extensometers and fibre optics for distributed sensing to understand the **fatigue behaviour and mechanism of R-UHPFRC**.

In **chapter 6** all the fatigue tests are discussed together. The constant amplitude **fatigue resistance of R-UHPFRC and design provisions** for structures are discussed to provide methods for dimensioning of the structural elements under fatigue loading.

Finally, in **chapter 7** all the **conclusions** are brought together and synthesized, and the possible **future research work** is outlined.

Chapter 2 Long-term strain measurements of traffic and temperature effects on a RC bridge deck slab strengthened with a R-UHPFRC layer

On fatigue-relevant actions and optimal data analysis

The content of this chapter was published as:

Sawicki, B., Brühwiler, E. Long-term strain measurements of traffic and temperature effects on an RC bridge deck slab strengthened with an R-UHPFRC layer. Journal of Civil Structural Health Monitoring 10, 333–344 (2020). https://doi.org/10.1007/s13349-020-00387-3

Bartłomiej Sawicki was responsible for maintenance of monitoring (since March 2017); data collection, analysis, processing and interpretation; conceptualization and preparation of the first draft; edition of the paper.

The examination of bridges under service conditions is challenging because of multiple actions applied to the structure, such as repetitive loads and temperature variation. Regarding fatigue safety verification, virtually any existing bridge recalculated using current standards fails[7]. This is why monitoring and understanding of the real action effects on bridge elements is important, especially regarding the fatigue.

The Chillon viaducts, in service since 1969, are two parallel structures with a total length of 2.1 km each and spans varying from 92 to 104 meters. This post-tensioned concrete structure was strengthened in 2014/15 by means of a layer of R-UHPFRC cast on top of the deck slab since structural and fatigue safety was of concern. The layer of UHPFRC accommodating steel reinforcement bars was casted to increase the stiffness and structural resistance of the deck slab and the box girder, and to serve as waterproofing layer protecting the existing reinforced concrete[16]. A monitoring campaign was commenced in May 2016 in order to verify the effectiveness of the UHPFRC-strengthening[17]. This method of rehabilitation and strengthening of reinforced concrete bridges has been developed over the last 20 years[18], became an established technique in Switzerland[19,20] and is now emerging in other countries. Similar principle can be used for orthotropic decks of bridges[21–24]

The direct measurement of traffic action effects is a reliable and cost-efficient method of quantification of structural demand. The collected data can be used to verify the safety of existing structures[25,26]. This approach is applicable for fatigue verification of bridges[27,28] where the effects of repeating actions are of importance. Additionally, thanks to direct monitoring, the behaviour under traffic and temperature actions can be analysed leading to better understanding of how the bridge works on the structural level, and to verify the prior assumptions[29,30].

There are numerous monitoring campaigns that led to reduction of uncertainties in structural demand and thus more reliable safety verification. For example, Sousa et al.[29] performed long-term strain monitoring of traffic action effects on the box-girder of the Leziria Bridge. The strain gauges were compensated for the temperature expansion, but the measured temperature-induced strains were neglected. A similar approach was followed by Treacy and Brühwiler[31] in the monitoring of two box-girder highway viaducts. Massicotte and Picard[32] performed extensive monitoring campaign of the massive box-girder of the Grand-Mere Bridge using strain gauges and thermocouples. On the basis of measured temperature gradients, they built a finite element model to assess the thermally induced stresses. However, no verification using strain gauges was done. Chen et al.[33] combined strain and temperature monitoring to quantify temperature induced stresses. Results were further analysed together with acceleration measurements to calculate the reliability of the structure. No long-term dynamic strain measurements were done.

Literature review shows that the contribution of thermally induced stress range to the fatigue damage is disregarded in most monitoring campaigns, albeit it might be significant[30]. The researchers are rather interested in the extreme values of temperature gradient, which is important as well[34–36]. The objective of this chapter is to quantify the structural response of the bridge deck under combined traffic and thermal actions. The quick and computationally efficient method of data analysis from the point of view of fatigue limit state is presented. The relevance of thermally induced stress cycles is discussed as well.

Description of the monitoring system

The monitoring system presented in this chapter is composed of four strain gauges and eight thermocouples. Since the fatigue resistance of reinforced concrete is governed by the steel reinforcing bars[15,37–39], the bottom layer of rebars of the deck slab is instrumented.

The strain gauges are glued in two locations (Figure 2-1). Group 1 is located at mid span, on the central axis of the slab, where the longitudinal and transversal bars are crossing. Group 2 is placed in the distance of around 50 cm from the first one, again at a crossing point of rebars. At each of the two locations, one gauge is glued respectively on the longitudinal and transversal rebars. To do so, the rebars were detected and then the cover concrete was carefully removed to expose the reinforcement.

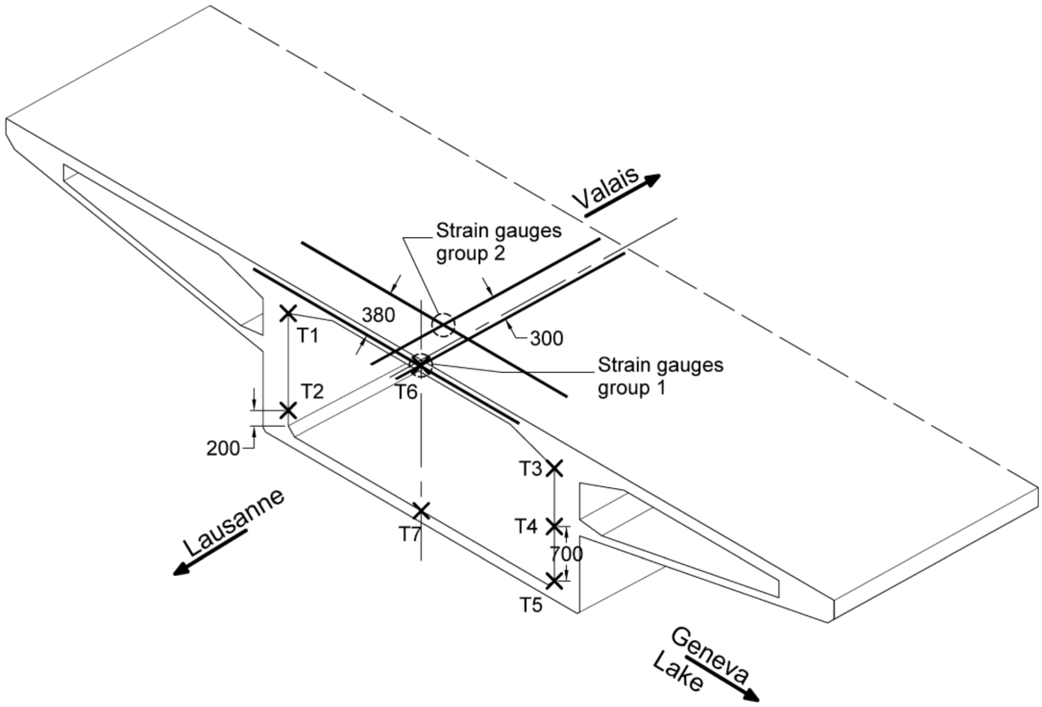

Figure 2-1. Scheme of monitoring; T1 to T7 - thermocouples; dimensions in mm.

The seven thermocouples are glued on the concrete surface along the perimeter of the box girder, inside. Additionally, the air temperature in the box girder is recorded.

The signals from the strain gauges are recorded with a frequency of 100 Hz, while from thermocouples with frequency of 1 Hz. The frequency is chosen to get the minimum file size while not losing any important strain peak due to the traffic. Still, about 200 MB of data is collected daily. The present chapter exploits the data collected between January 20th 2017 and April 10th 2019. Due to technical problems, some days of recording were omitted resulting in 602 full days of monitoring data.

Structural response due to single traffic events

The signal recorded with the DAQ (Data Acquisition System) is composed of the traffic-induced strain ranges and the "thermal wave", as presented in Figure 2-2. To analyse the monitoring results, the two kinds of signals are separated. Since the variation of strains due to the "thermal wave" is much slower than traffic-induced strains, a running average function is used. The signal resulting from this operation presents only the thermal response of the structure. If this signal is subtracted from the original one, only the structural response due to the traffic action is obtained[31]. In this chapter the consequences of this separation are discussed.

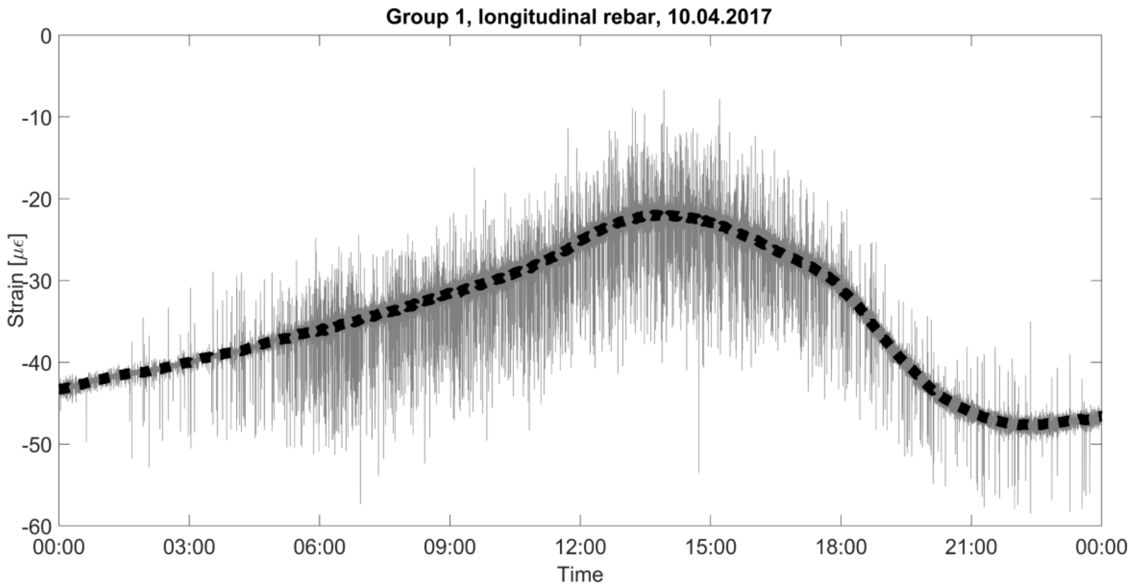

Figure 2-2. Strain recorded during one day on longitudinal rebar, group 1; filtered-out “thermal wave” shown with dotted line.

The structural behaviour of the deck slab under traffic loading is discussed here on the basis of single truck passages for the sake of clarity. Figure 2-3 presents the strain signals recorded by the four strain gauges at the same instance of time, and the truck that could possibly produce this response. Since there is no visual monitoring of the vehicles on the viaduct, the type of truck cannot be determined precisely.

The transversal rebar response is exclusively local, and it is subjected to the tensile cycles due to the passage of each axle. The response of rebars in the longitudinal direction depends on the weight of the passing truck. In the case of a normal 5-axle truck of 40 tonnes of weight or a 50 t crane, the global box-girder response produces compressive stresses in the slab. Thus, in addition to compressive stress, the longitudinal rebar is subjected to tensile local stress under the wheel load, leading to the tensile-compressive reversal stress cycles. However, for an extremely heavy special transport using multi-axle lowboy truck, the global behaviour is so pronounced that there is no tensile stress in the rebar. The response due to each axle is still visible, but the strain is always negative leading to one pronounced compressive cycle rather than multiple tensile cycles. Thanks to the almost equal load distribution among axles, the recorded transversal strains are comparable with the ones from the 40 t truck.

The transversal rebar is more sensitive than the longitudinal one to the position of truck on the traffic lane. The strain differences recorded by the two transversal gauges are much larger than the strain differences obtained from the longitudinal rebars for 40 t and lowboy trucks. However, for the 50 t crane these differences are much smaller, probably because the crane was travelling very close to the fast lane or even on the fast lane.

Overall, the transversal rebar is showing only local response due to axle passage, while the longitudinal bars present a mixture of global and local response under traffic loading. Importantly, the fatigue relevant damage is not directly linked to the truck or axle load, which shows the importance of direct strain and stress measurements in existing bridges to obtain realistic data for fatigue safety verification.

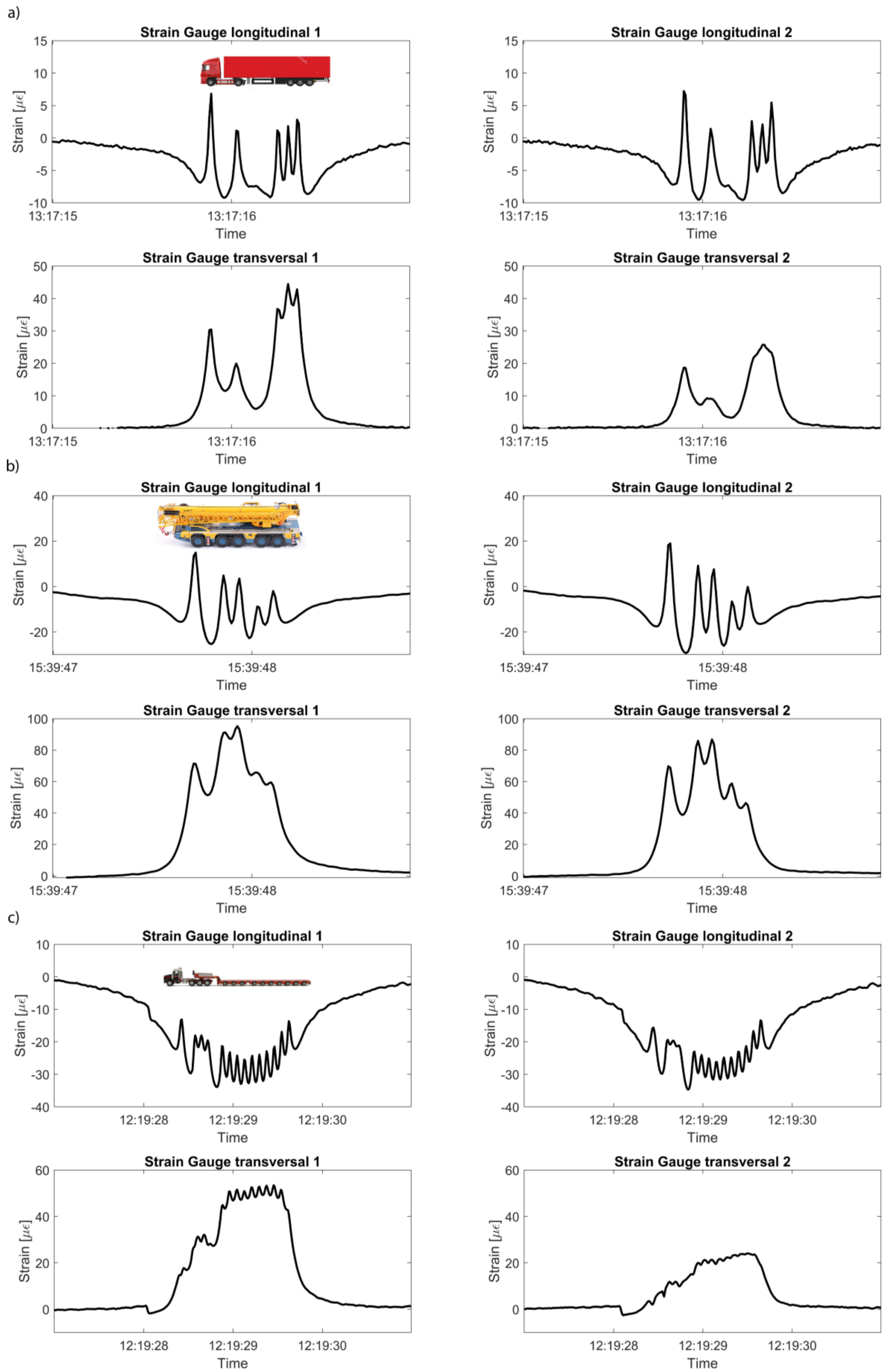

Figure 2-3. a) Typical 5 axle truck, recorded on 10.04.2017; b) 5 axle mobile crane, recorded on 23.06.2017; c) Exceptionally long lowboy track, recorded on 15.03.2018.

Structural response due to temperature variation

Diurnal variation of temperature

The monitored part of the viaduct is oriented approximately along the north-south direction. From the east, it is close to the slope of a mountain and the neighbouring viaduct, while the western part is fully exposed due to the situation next to the lake. The effect of this orientation will be discussed below using the example of a randomly chosen day (10.04.2017). Due to its situation, the structure remains shadowed in the morning, while being exposed to the sun in the afternoon until the sun sets. Since the temperature is measured on the bottom face of the concrete slab and in the box girder, additional delay due to the heat transfer across the slab is observed. Thus, the lowest recorded temperature occurs at around noon (Figure 2-4).

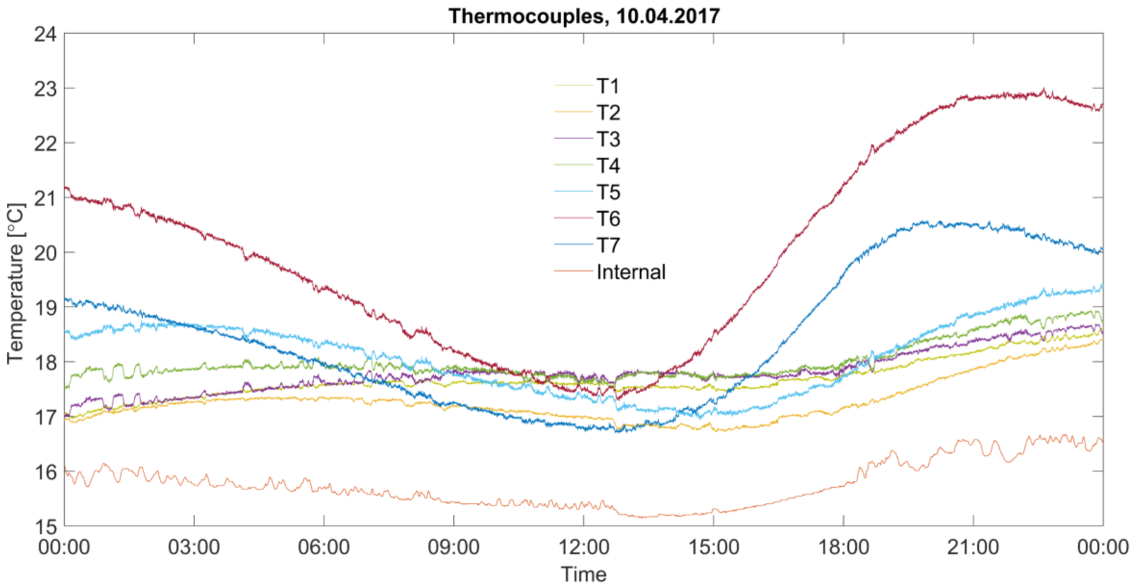

Figure 2-4. Temperature recorded during one day with all thermocouples.

The largest temperature variation is recorded by thermocouples T6 and T7, which are located respectively on the upper and lower slab of the box girder. This is explained by the difference in concrete thickness, i.e. the upper slab thickness is 22 cm and the lower slab is 16 cm, while the webs are 40 cm thick. Additionally, the voids of the cantilever slabs act as thermal insulators. Due to that, the web temperature starts to rise approximately 2 hours later than the temperature of the slabs.

Within the thermocouples on the webs, the highest temperature is recorded by thermocouples T5, then T4 and T3 respectively. This is explained by the exposition of this wall to the west, where the sun may operate approximately from 3 p.m. until sunset (8 p.m.) on the discussed day (April 10th).

The most stable temperature is the one recorded inside of the box-girder, and it is also lower than the temperature of the webs. This depends on the external air temperature during the couple of previous days and is expected[31].

Strain variation due to temperature

The thermal strain recorded during one day is presented in Figure 2-5. For the longitudinal strain gauges, the strain is approximately linearly dependent on the temperature of the deck slab. This indicates the expansion along the axis of the viaduct and no loss of stiffness. In case of the transversal gauges, the strain readings form a loop. This is caused by the previously described complex distribution of temperature on the perimeter of box girder.

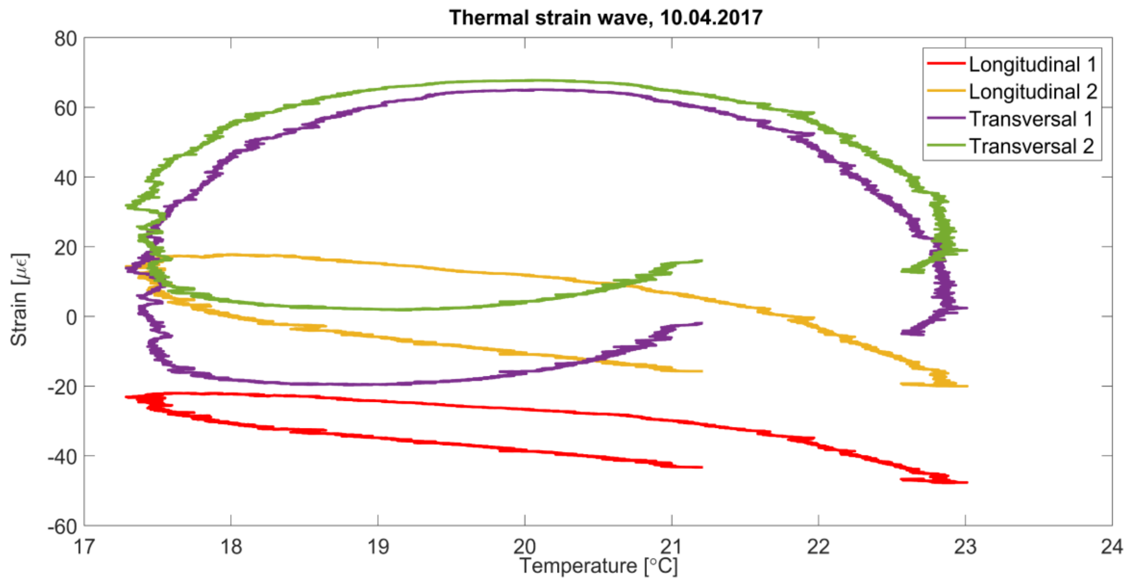

Figure 2-5. “Thermal wave” strain vs. temperature recorded on 10.04.2017.

Verification of reliability of results using thermal strains

Figure 2-6 presents the daily temperature variation and the daily “thermal wave” variation for the whole duration of monitoring. Obviously, the bigger the temperature variation, the bigger are the induced strains. This dependency can be used to verify the reliability of the sensors[40]. The longitudinal gauge of Group 1 was following the thermal amplitude only until spring 2018 when this gauge was no longer functioning properly, probably because of humidity due to improper sealing. From this incident on, the data from this gauge are not taken into account. The transversal gauge from Group 2 was following the temperature variation until it failed completely in July 2018. The two other gauges were closely following the temperature variation without inconsistencies during the whole duration of measurement.

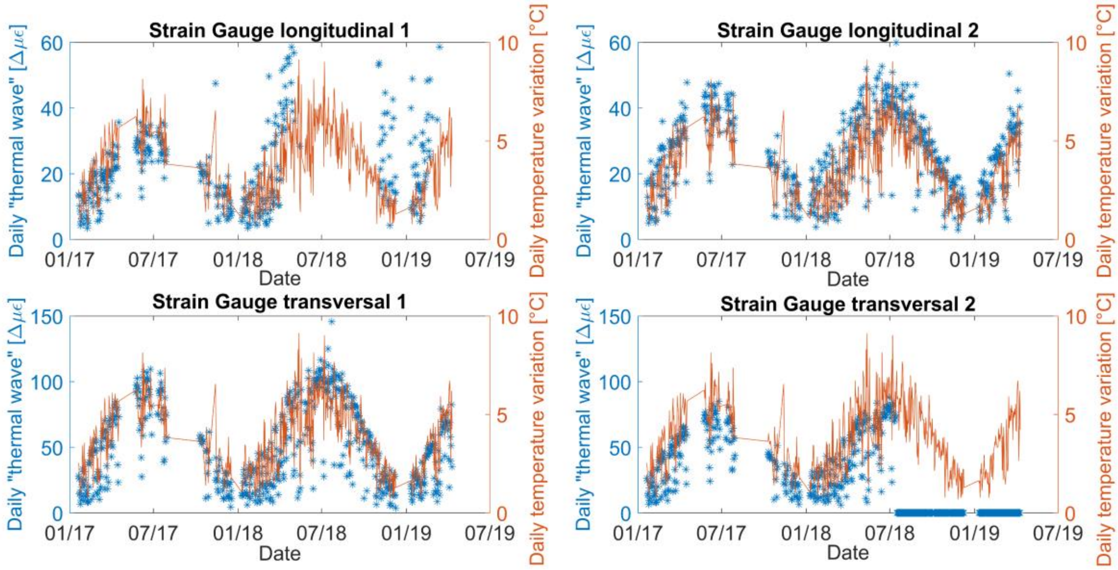

Figure 2-6. Daily temperature amplitude and thermal strain variation for the whole monitoring period.

Importance of temperature effects

As mentioned previously, the recorded raw signal is composed of the strain from two sources: thermal and traffic actions. When only the vehicle traffic loading is of interest, the thermally induced strains need to be removed. However, with proper instrumentation, the thermal strain readings can carry relevant information as well. In this monitoring campaign, the Poisson half-bridge system was installed, which is a type of the Wheatstone Bridge circuit[41]. It is composed of two active gauges, measuring the strain perpendicularly in relation one to another (Figure 2-7).

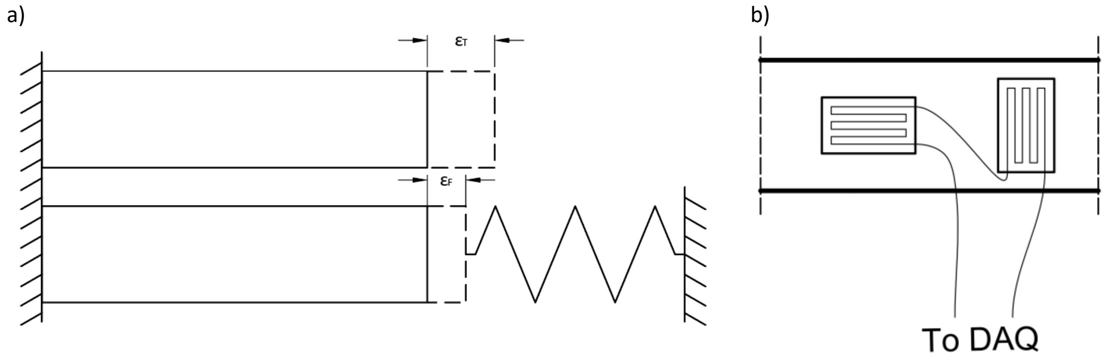

Figure 2-7. a) Free and partially restrained thermal expansion; b) Scheme of strain gauges glued on rebar in half-bridge.

The gauge oriented along the rebar axis measures both the thermal expansion of the slab and the deformations due to the traffic action. Since the concrete cover of the rebar is locally removed, the section of interest is free to expand in the direction perpendicular to bar axis. Thus, the perpendicular gauge is recording only the free thermal expansion of steel and the strain variation due to Poisson's effect. Thanks to the half-bridge connection, the signal recorded by the perpendicular gauge is subtracted from the signal recorded by the longitudinal gauge, taking into account the Poisson's effect.

The DAQ automatically cancels out the variation of electrical conductivity of cables and measurement unit due to the changes of temperature. Thus, the only source of this difference originates from the strain gauges.

The upper portion of Figure 2-7a) represents the situation of the gauge that is perpendicular to the rebar axis. If the Poisson's effect is disregarded, it measures only the free body expansion according to the formula:

Equation 2-1

$$\varepsilon_T = \alpha_T \cdot \Delta T$$

where ε_T is a free thermal expansion, α_T is the coefficient of thermal expansion and ΔT is the temperature variation.

The measurements taken by the gauge parallel to the rebar's axis are affected due to the partial restraint of the slab that still allows for some free expansion, noted with ε_F. The effect of Wheatstone half-bridge can be described by the relation:

Equation 2-2

$$\varepsilon_F - \varepsilon_T = -\frac{\sigma_T}{E}$$

where σ_T is the stress due to partially restrained thermal expansion and E is the modulus of elasticity of steel. The right part of Equation 2-2 is recorded by the DAQ as a "thermal wave" as shown by the dotted curve in Figure 2-2. Thus, the monitoring system allows for an indirect measurement of the residual thermal stress variation in the structure.

The variation of the residual thermal stresses in the longitudinal and transversal rebars is presented in Figure 2-8. In the longitudinal rebar, the structural response is delayed by 1.5 hours with respect to the deck slab temperature. The transversal rebar stresses are further delayed, in total by 4 hours. The stress variation in longitudinal rebar is mostly dependent on the temperature of the deck slab, while the transversal rebar responses depend on the temperature distribution along the whole box-girder perimeter. These effects are common and expected in reinforced concrete structures[30,31]. Importantly, the stress ranges in the transversal rebar are much larger than that in the longitudinal rebar.

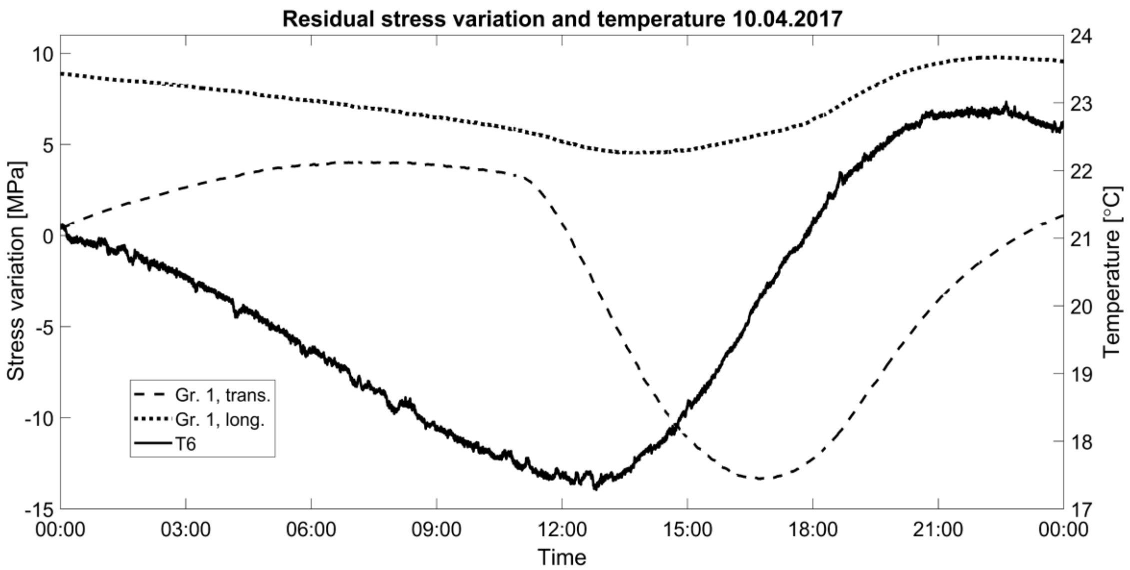

Figure 2-8. Residual thermal stress variation and temperature recorded during one day.

Measured stress ranges due to traffic and thermal actions

Histograms of stress ranges due to traffic and thermal actions

Figure 2-9a) shows the histograms of stress ranges originating from temperature variation and Figure 2-9b) from traffic loading. The histograms were prepared for measurements between January 20th 2017 and April 10th 2019, thus 602 full days of data. Stress is determined by multiplying the strain readings with the modulus of elasticity of 205 GPa for steel rebars. Only the results from gauges of the transversal rebar from Group 1 and longitudinal rebar from Group 2 are shown. The other two gauges failed prematurely, however their responses were similar to the presented ones.

The thermal stress range histograms were prepared by taking the thermal stress of each day and composing them together. Then, the rainflow counting algorithm was applied to this data. In this way, the day-to-day offsets are not considered since the effect of windowing is avoided. The stress values due to traffic loading were treated separately, day after day.

Figure 2-9 reveals that, firstly, the maximum stress ranges due to both traffic and partially restrained thermal expansion are similar for the transversal rebar. The temperature induced stress ranges are even higher than traffic induced stress ranges for the longitudinal rebar. Obviously, the number of cycles due to the traffic is much higher than due to the temperature.

Secondly, the stress ranges in the steel rebars are far below the Constant Amplitude Fatigue Limit (CAFL) of 120 MPa according to the Swiss standard for existing structures SIA 269[38]. Thus, and since the readings were taken in the determinant zone of the most likely highest stresses, the deck slab is not prone to fatigue damage.

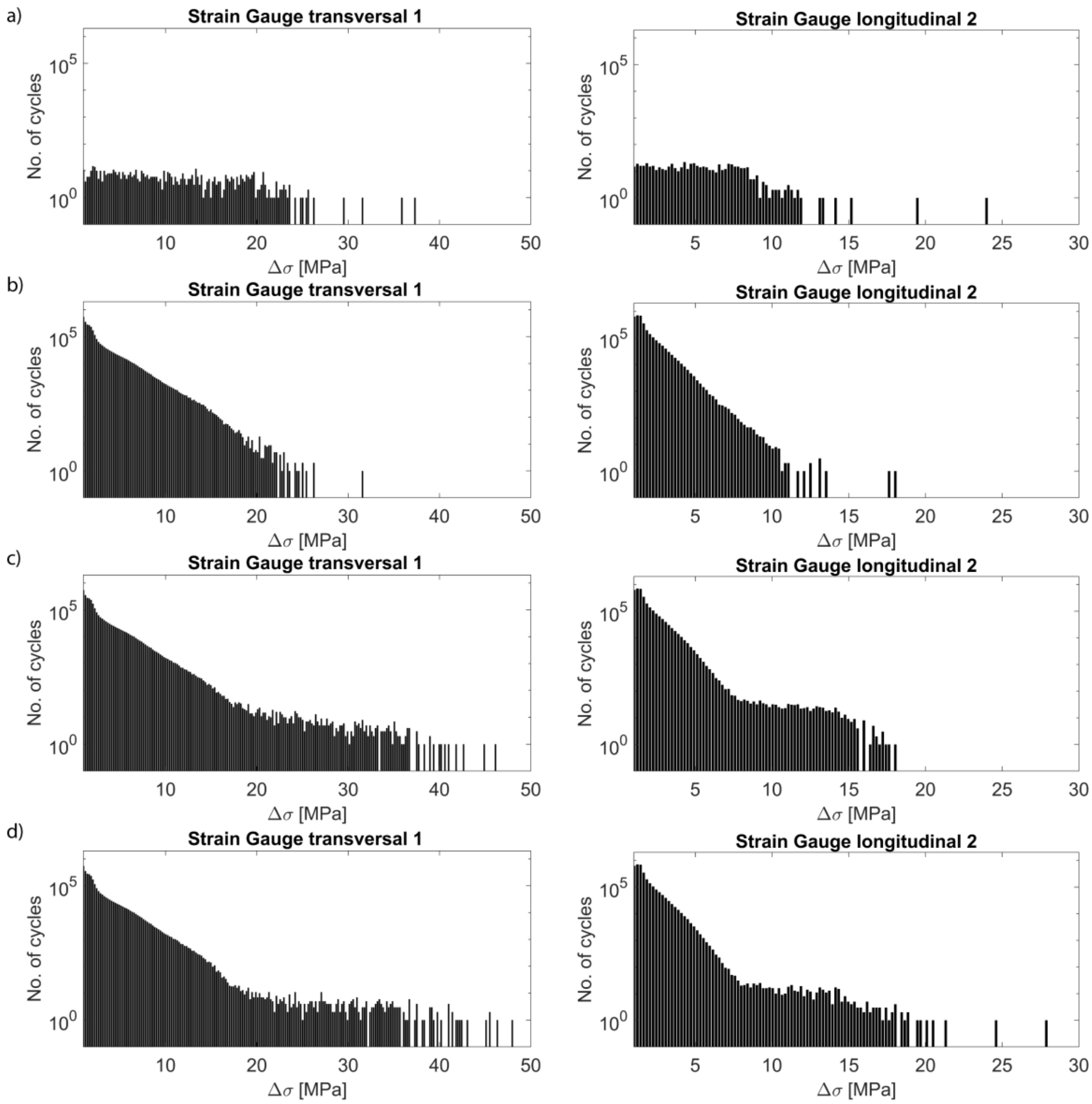

Figure 2-9. Histograms of stress ranges induced by: a) temperature (treated separately), b) traffic (treated separately), c) combined temperature and traffic with 24h windowing and d) combined temperature and traffic with 75 days windowing. These histograms are given for the whole monitoring period (602 days) and correspond to gauges: transversal from group 1 and longitudinal from group 2.

Effect of windowing of the rainflow algorithm on stress range determination

As presented above, both thermal and traffic-induced stress cycles are fatigue relevant. However, the rainflow counting algorithm is sensitive to windowing, and the temperature and traffic induced effects are therefore treated separately. For the sake of a sensitivity study, another procedure was followed as well.

First, the original signal was divided into as few windows as possible due to computational program limits, i.e., 8 windows of a size of 75 days. Then, since it is the negative of thermal stresses that is observed (Equation 2-2), the "thermal wave" was separated from the raw data as described previously, inverted and summed again with the traffic induced strain readings. In this way, after multiplication with the modulus of elasticity, the complete stress range spectrum in rebar was obtained (Figure 2-9d)). To visualise the influence of windowing, the signal prepared in the same way but with the daily window, is presented in Figure 2-9c).

The effect of windowing is visible only in the highest values of stress range. This is due to the season-to-season thermal variations that are larger than the daily temperature variations. However, these cycles are rare and can be considered as irrelevant with respect to fatigue. Thus, window length of 24 h for the rainflow counting should actually be used, as it is computationally much less expensive and sufficiently precise.

The “tail” of histograms in Figure 2-9c) is longer than in Figure 2-9b) representing the largest stress range values due to the temperature and heavy trucks combined. They occur when one truck is passing while the thermally induced stress cycle is close to minimum, and another truck is passing at the peak of the diurnal stress cycle. The difference between peaks of these events, thus the maximum stress cycle, cannot be captured by the traditional approach when temperature and traffic strains are separated. However, when the recorded stress range is far below the CAFL like in the present case, this difference is not relevant. On the contrary, when the stress range due to traffic is close or higher than the CAFL, the temperature effects should be taken into account as they might be significant even for relatively simple structural elements. This is confirmed in Eurocode 2[42] clause 2.3.1.2 stating that thermal effects should be taken into account in the analysis of fatigue limit state only if they are significant.

It should be noted that the variation of structural response due to change of temperature is inherently present in the traffic part of recorded stresses as described in the next section.

Apparent fatigue damage

The Palgrem-Miner rule and fatigue resistance curve given in SIA 269/2[38] were used for the calculation of traffic induced apparent theoretical damage due to fatigue. The fatigue resistance of the present straight rebars is defined by a detail category of 150 MPa at 2 million cycles; the slope in the S-N-diagram is 4 with a break point at 5 million cycles and 120 MPa[43]. The damage should be called “apparent”, as all the stress cycles are below the CAFL, thus no real damage takes place. Damage accumulation was conducted here for the sake of comparison only, with a slope of 7 below the CAFL.

Figure 2-10 presents the daily apparent damage and mean temperature of the deck slab (thermocouple T6). The peaks of damage due to the isolated events are clearly visible.

The fluctuation of daily damage comes not only from traffic’s stochastic nature but also from the change of material and structural properties due to the temperature variation. At higher temperature, the contribution of the asphalt pavement is lower due to the lower stiffness[17,31,44]. Thus, the contribution of steel rebars is higher in response. This effect is visible in the Figure 2-10 as well. This proves also that the strain measurements were reliable.

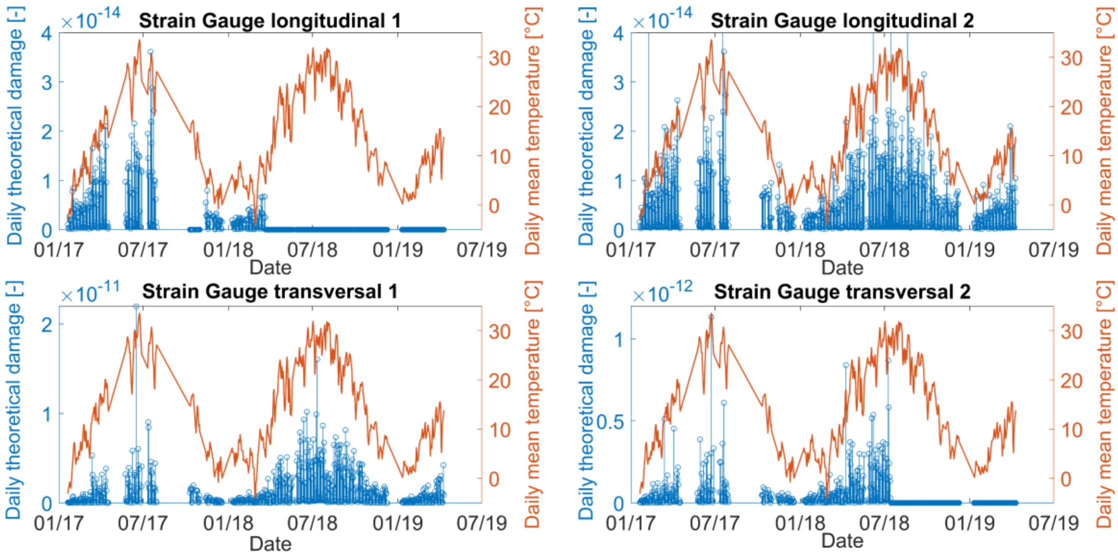

Figure 2-10. Daily apparent damage and daily mean temperature of slab.

Comparison of results from monitoring with calculations using a standardized load model

Since the deck slab of the box-girder was originally relatively thin (18 cm), its fatigue performance was of concern before the strengthening with a UHPFRC layer. Below, a simplified fatigue analysis of the UHPFRC strengthened, 22 cm thick deck slab in transversal direction is presented.

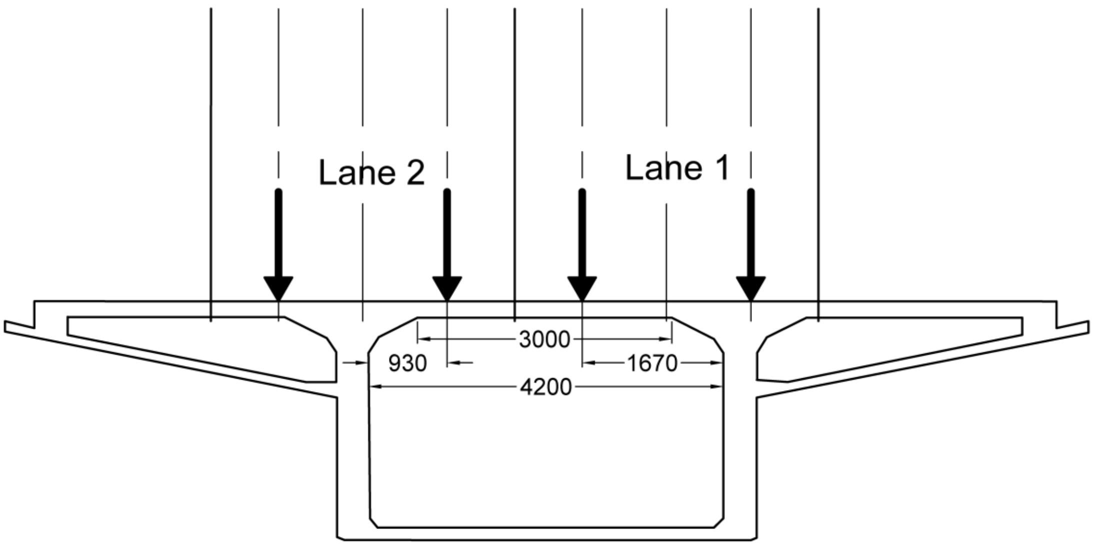

Figure 2-11. Cross-section of the superstructure with layout of the fatigue load model (dimensions in mm).

The deck slab (Figure 2-11) can be represented simply by an elongated plate fixed along its longer sides. As the haunched parts are much stiffer than the slab itself, a span of 3 m is adopted for this calculation. A Finite Element model using shell elements was prepared to calculate the bending moments in the deck slab. The tandem axle loads of Load Model 1 according to European Standard[45] was applied to determine fatigue relevant stress values in the rebars. The tandem consists of two axles spaced by 1.2 m with characteristic axle load Q_{k1}=300 kN.

According to the Swiss standard for existing structures[46] this axle load is updated to account for more realistic traffic loading:

Equation 2-3

$$Q_{fat} = Q_{k1} \cdot \alpha_{Q1,act} \cdot \gamma_{Ff} = 300kN \cdot 0.7 \cdot 1.0 = 210kN$$

where Q_{k1} is the characteristic axle load on Lane 1; $\alpha_{Q1,act}$ is the updating factor for road traffic; γ_{Ff} is the partial load factor for fatigue. The fatigue load model is positioned on the real, rightmost lane of traffic (Figure 2-11) and the wheel force is distributed on the square area with an edge length of 0.4 m.

The calculated maximum positive bending moment is equal to 24 kNm, and the computed strain and stress distributions due to this moment are given in Table 2-1. The maximum stress range in the rebars is just below the CAFL. This is because the strengthening of the structure was designed using the method presented here.

Table 2-1. Calculated stress distribution in the deck slab under maximum positive bending moment 24 kNm/m.

Layer	Strain [‰]	Stress [MPa]
UHPFRC	-0.13	-7
Reinforcement in UHPFRC	-0.04	-9
Concrete	N/A	N/A
Upper reinforcement in concrete	0.09	18.2
Lower reinforcement in concrete	0.53	108

N/A – not applicable

Table 2-1 reveals that the calculated stress range using the code-based load model is about four times higher than the measured maximum stress range. This large difference comes, among others, from the consideration of a high dynamic amplification factor implicitly present in the code-based load model[47] leading to overestimating the load by a factor of almost two. Eventual dynamic effects on the stress in the rebar are actually implicitly included in the monitoring data, which also show no notable dynamic response in the case of the present massive concrete structure. In fact, Figure 2-3 shows that the passage of a vehicle axle does not produce any vibration of the deck slab since the strain state returns immediately to the one before the passage. In addition, the static axle load considered in the code-based fatigue load model is higher than the measured mean static axle load using Weigh-In-Motion data from current vehicles in operation in Switzerland[48] and Europe.

Obviously, current methods of calculation of stresses in bridge elements lead to very conservative and thus uneconomical results in the safety verification of existing bridges. Consequently, the method of direct measurement and monitoring of fatigue action effects on bridge elements should be deployed in case of fatigue concerns before any bridge intervention is undertaken.

Conclusions

This chapter presents results from the 28-month-long monitoring of the reinforced concrete deck slab of a highway viaduct, which was strengthened with R-UHPFRC (Reinforced Ultra High Performance Fibre Reinforced Cementitious composite). This campaign was realised with thermocouples and strain gauges, glued directly to steel rebars. The structural response of the deck slab under both thermal and traffic induced strains is discussed. The following conclusions can be drawn:

- In massive concrete bridge structures, stress ranges due to traffic loading and temperature action can be of similar magnitude.
- Stress variation due to the partially restrained thermal expansion is fatigue relevant when combined with high traffic-induced stress cycles. The two action effects should be treated together to identify relevant combinations.
- Windowing of 24h using the rainflow counting algorithm is effective to gather thermally induced stress ranges with sufficient precision.
- The yearly and seasonal cycles of residual stresses due to restrained thermal expansion are not fatigue relevant, and thus, they do not need to be considered for fatigue safety verification.
- Fatigue relevant stress ranges as obtained from monitoring in the investigated deck slab portion of the viaduct are significantly smaller than the CAFL of the determinant rebar.
- Measured stress values are significantly smaller than the corresponding stress values obtained from calculation using load models as defined in standards.

Chapter 3 Influence of monitoring duration on measured traffic action effects on road bridges

On influence of duration of monitoring on results and on translation of monitoring results to long-term behaviour

The content of this chapter was accepted for publication as:

Sawicki, B., Brühwiler, E. Influence of monitoring duration on measured traffic action effects on road bridges. *Bridge Maintenance, Safety, Management, Life-Cycle Sustainability and Innovations: Proceedings of the Tenth International Conference on Bridge Maintenance, Safety and Management (IABMAS 2020) (Yokota H., Frangopol D.M., eds.), June 28-July 2, 2020, Sapporo, postponed to 2021* (2020).

Bartłomiej Sawicki was responsible for maintenance of monitoring and data collection of Chillon viaduct; data processing, analysis and interpretation from Chillon and Crêt de l'Anneau viaducts; development of methods, conceptualization and preparation of the first draft; edition of the paper.

Maintenance, use and management of existing infrastructure is an engineering task of first importance[2,49,50]. Structural engineering codes are established and calibrated to be used for the design and construction of new structures, where the uncertainty about the material properties and actions (loads) is higher than in the case of existing structures, where these parameters are updated reducing thus uncertainties[7]. The Swiss standards for existing structures[51] are a comprehensive set of codes addressing engineering of existing structures, which is still unique worldwide.

Verification of structural safety of existing structures is done by a procedure in stages[51]. The general verification is the simplest but least precise and conservative. The detailed verification is more refined and complex but precise and more realistic. It can be stated that any existing structure designed using former codes would obviously fail in the general verification stage if current design codes are applied for structural safety verification. Thus, before any (costly) structural intervention is undertaken, detailed verification must be performed as this is always more economic and sustainable.

Monitoring of traffic action effects on bridge elements is one of such methods leading to reduction of uncertainty of demand. Using basic electronic devices, strains and thus stresses due to regular traffic can be directly measured. The researchers[40,52] recommend the duration of monitoring campaign to be one full year for the massive concrete bridges, which allows to grasp the yearly variation of traffic and temperature.

Sometimes, due to time or financial constraints as well as engineering efficiency, there is a need to know the shortest monitoring period necessary to comply with the required reliability of obtained data from monitoring. This chapter addresses the question how long the monitoring campaign should last to obtain reliable results and how to take into account the duration of monitoring.

Tools and methods

The signal registered by strain gauges carries two kinds of information: 1) traffic induced stresses and 2) partially restrained temperature expansion induced stresses[53]. In this chapter, only the traffic induced part of the signal will be discussed, which is extracted using running average function[31].

Apparent daily damage

The standard approach for fatigue analysis of bridges is the Palgrem-Miner method with damage accumulation calculation on the basis of stress cycles and S-N curve. In the two case studies presented in this chapter, the registered stress cycles are below the CAFL (Constant Amplitude Fatigue Limit), and thus, no real damage is induced. The CAFL, according to Swiss standard for existing structures [38] is equal to 120 MPa for straight reinforcement bars of diameter below 30 mm.

For the sake of comparison, the apparent fatigue damage is computed on the basis of the bi-linear S-N curve with slope m=4 for cycles higher than 120 MPa and m=7 for cycles lower than 120 MPa. The point of slope change is located at 5 million cycles.

The apparent daily damage is computed using daily histograms, prepared using traffic induced stresses registered by strain gauges and with application of the rainflow algorithm as recommended in European standard[45]

Narrowing Confidence Interval

Road traffic actions are stochastic. While treated from probabilistic point of view, the measured values are extrapolated for a given return period using Extreme Value Theorem (EVT) based on fitting of Generalized Extreme Value (GEV) distribution. Depending on the quality and amount of input data, different confidence intervals of extrapolation are obtained. Contrary to the classical use of EVT for static loads, here the return levels are treated from qualitative point of view. The width of the confidence interval (CI) can be used to verify whether the duration of monitoring is sufficient and representative[52]. The Narrowing Confidence Interval (NCI) using block maxima is used in this chapter. The daily block maximum, which is a maximum traffic induced stress level registered for a given day, was chosen as representative. Due to diurnal variation of the traffic (peak hours and small traffic at night) choice of smaller blocks is not recommended[10].

In this chapter, return period of 75 years (Z75) is used, which is a reasonable for an existing bridge and was used recently by other researchers[52,54].

The NCI method is applied to the daily monitoring data taking into account all days recorded previously. Two indicators to quantify the quality of collected data by NCI method are used. The first one is the time step comparison (TSC) describing width of CI after each date, according to formula:

Equation 3-1

$$I_{TSC,i} = [z_{95} - z_5]_i - [z_{95} - z_5]_{i-1}$$

where z_5 and z_{95} are respectively 5th and 95th percentile of estimated return levels for return period of 75 years, thus width of CI, after ith day of monitoring. The second method is the Normalized Confidence Interval width (NCIW):

Equation 3-2

$$I_{NCIW,i} = \frac{[z_{95} - z_5]_i}{Z75_i}$$

where Z75 is the estimated return level for return period of 75 years after ith day of monitoring.

The smaller both indicators, the better and more stable is the recorded data.

Sampling of monitoring data

The probability of an event can be defined as its relative frequency in many trials. In this frequentist probabilistic approach, a sufficiently big number of tests will lead to a set of solutions following the distribution of a sample space. This principle is used to explore the influence of stochastic traffic data on the results of the NCI and apparent daily damage. Similar approach, akin bootstrapping, was used by other authors for weight-in-motion data[52] and for bridge monitoring data[55].

The daily histograms (for apparent damage approach) and daily block maxima (NCI approach) were prepared on the basis of monitoring data. The information about a) season – to indirectly take into account possible influence of temperature on the structural response; and b) day of the week – to take into account variation of traffic between week days and weekends; were prepared.

Then, by means of a large number (100) of permutations, keeping the season and day of the week, a set of observations of one-year duration were prepared. In this way, the influence of stochastic nature of traffic on convergence of two methods (NCI and apparent damage) and the variation of possible results can be analysed. This method is valid under the assumption of stationarity of traffic volume and weight in the following years.

Variation of cumulative damage

The cumulative damage based on the summary of daily damage recorded by monitoring is a basis of the fatigue assessment using Eurocode Load Model 5[45]. However, due to the stochastic nature of traffic the cumulative damage recorded during a short period may not be representative for the whole service duration of the bridge. To cope with that, Eurocode 1-2 Annex B[45] recommends multiplication of the number of lorries (stress cycles) by 2 and load levels (stress amplitudes) by 1.4. In the case of monitoring of the Chillon viaduct, this leads to augmentation of cumulative damage by factor of 20. Thus, more economical guidance is needed.

Cumulative Damage correction Factor (CDF) depending on the monitoring duration is proposed in this chapter. Using the abovementioned sampling method, 100 one-year-long monitoring campaigns were simulated and cumulative damage was computed after each day of monitoring. Then, 5th (CD_5) and 95th (CD_{95}) fractiles are found. The Cumulative Damage correction Factor is defined as follows:

Equation 3-3

$$\gamma_{CDF,i} = \frac{CD_{95,i}}{CD_{5,i}}$$

Multiplication of the cumulative damage obtained in short-term monitoring campaign with this factor should bring a correction taking into account the stochastic nature of traffic.

Case studies

In this chapter, the methods presented above are applied to two bridges for which long-term monitoring data is available. Since the two bridges carry different classes of road (two-lane highway and bi-directional road) and their structure is different (posttensioned concrete and concrete-steel composite structure) the obtained results can be generalized.

To grasp correctly the seasonal variation of structural response to traffic actions, each one-year-long simulation was started on four different dates during the year: January 1st, April 1st, July 1st and October 1st.

Below, the detailed procedure is presented for Chillon viaduct and starting date on January 1st only. Relevant mean curves are presented for Crêt de l'Anneau viaduct case and other starting dates for the sake of clarity.

Chillon viaduct

The Chillon viaducts are two structures with length of 2.1 km each, located in Western Switzerland. Each structure carries one direction of highway with two lanes and an emergency lane. The prefabricated post-tensioned reinforced concrete box-girder structure is in service since 1969. In 2014/2015 it was strengthened with cast-in-place layer of reinforced UHPFRC[16]. In 2016, strain gauges were glued directly on the locally exposed reinforcement bars on the bottom side of the slab. Representative location, at the viaduct centreline and middle of a typical span, was chosen. The transversal rebar response depends on the axle load, while the longitudinal rebar response is a mixture of local response due to axle loads and global response due to truck weight[53], as discussed in Chapter 2, thus the two are discussed here. 602 days of data registered between

January 2017 and April 2019 are available. The stationarity of data was confirmed using Kwiatkowski-Philips-Schmidt-Shin (KPSS) stationarity test[56]

Results of NCI

The first step in NCI method is the extrapolation of daily block maxima. One hundred one-year-long monitoring campaigns were simulated by sampling daily block maxima over the full monitoring period. Then, the return levels for return period of 75 years was extrapolated after each day of monitoring. The extrapolated values starting on January 1st are presented in Figure 3-1. It can be noticed that when the amount of data is sufficient, the values are less scattered. The mean of extrapolated values after one year of monitoring is 33 με and 132 με for longitudinal and transversal rebars respectively. For comparison, maximum values of strains registered during monitoring campaign were equal to 32 με and 122 με respectively. Since these highest registered values are not necessarily present in every sampled dataset it can be concluded that the number of 100 samples gives a representative mix of data. Similar behaviour in terms of stabilization of value with increase of observation time was noticed for the width of confidence interval, which is not presented here.

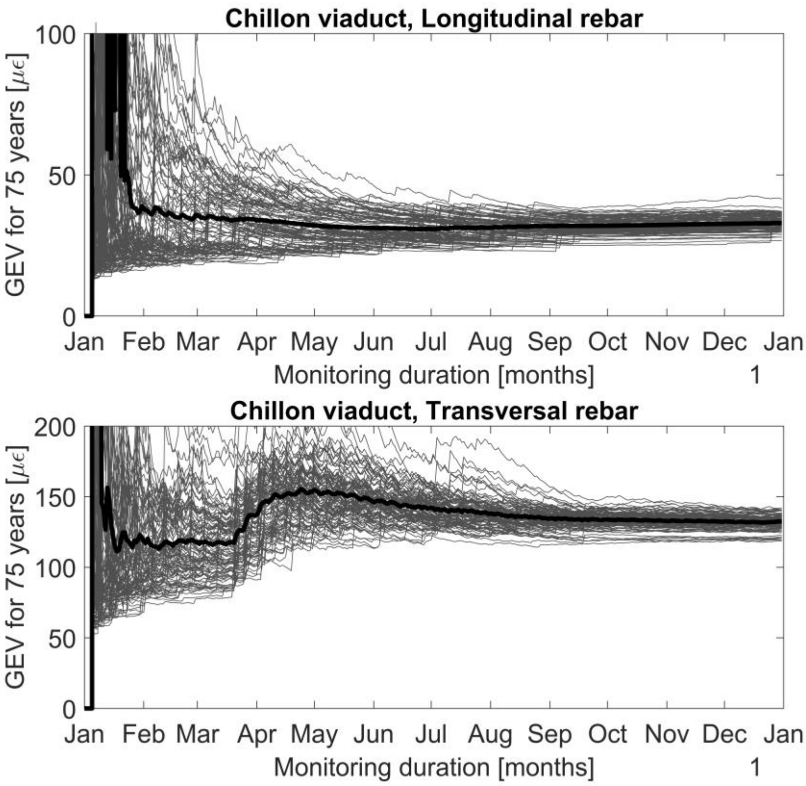

Figure 3-1. Extrapolated return levels for return period of 75 years for two strain gauges of Chillon viaduct and the average value.

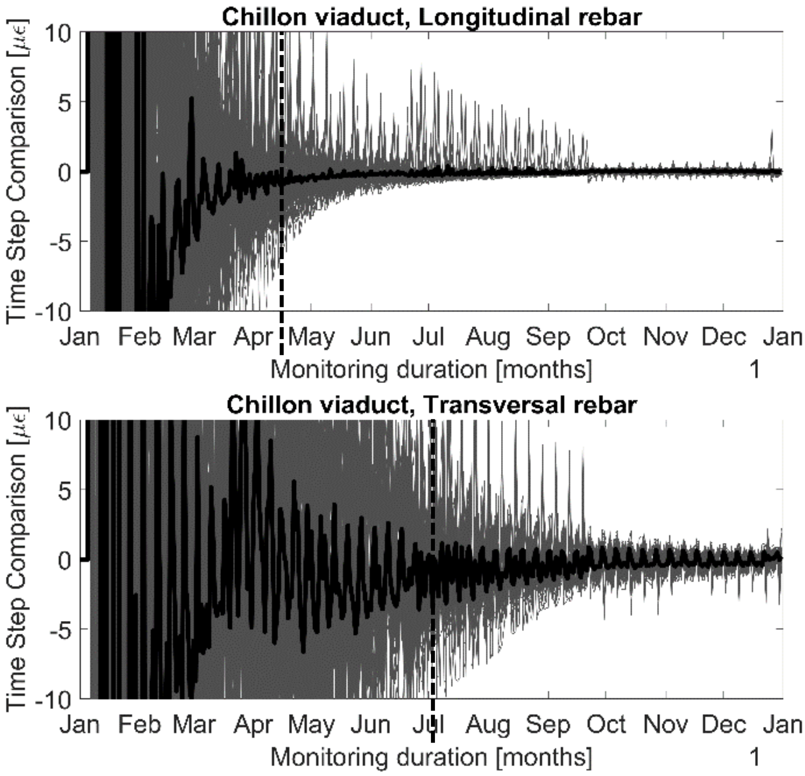

Figure 3-2. Time Step Comparison for two strain gauges of Chillon viaduct and the average value with 100 and 180 days period (marked).

The next step is to use the Equation 3-1 and Equation 3-2 to calculate the TSC and NCIW indicators respectively. They are presented in Figure 3-2 and Figure 3-3.

The TSC for longitudinal rebar stabilizes approximately after 100 days. The transverse rebar needs around 180 days to achieve stable indicator. Since the transversal rebar receives higher strains and responses to axle load only[53] it is more sensitive to the traffic variability. Interestingly, the individual sampled curves reveal peaks, which are spaced by 7 days. This indicates large weekly variation of traffic and comes from heavily loaded trucks observed during weekdays.

In turn, the mean NCIW is stabilizing at similar pace for both rebars. After 100 days it reaches values that are close to final, and after 180 days the final values are achieved.

However, for individual curves this pace varies a lot for both indicators. This variability comes from the stochastic nature of traffic data. The heaviest trucks can occur in the very beginning of the monitoring campaign, leading to fast stabilization of indicators, or, they might arrive later de-stabilizing the extrapolated values. This phenomenon is discussed below.

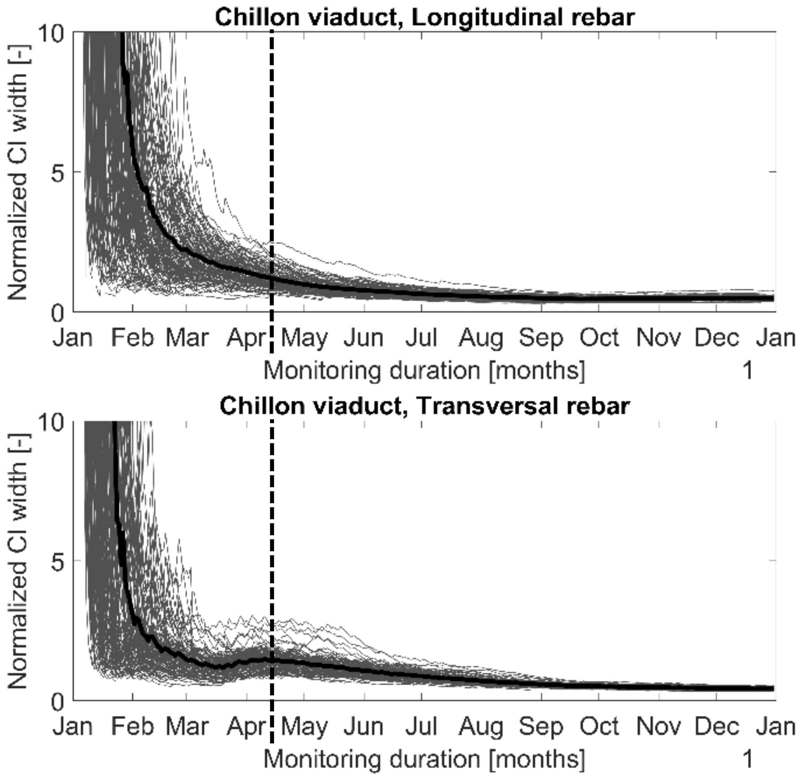

Figure 3-3. Normalized Confidence Interval width for two strain gauges of Chillon viaduct and the average value with 100 days period (marked).

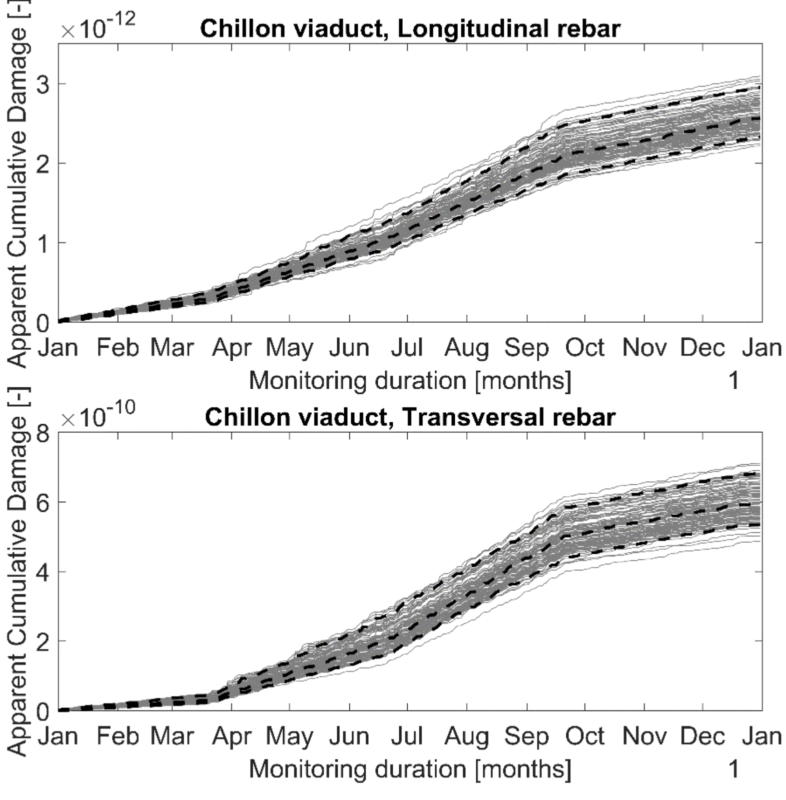

Figure 3-4. Apparent cumulative damage for two strain gauges of Chillon viaducts. Dashed curves represent 5th, 50th and 95th fractiles.

Results of cumulative apparent damage

The apparent daily damage was resampled as discussed previously. The simulated curves, together with mean value, 5th and 95th fractile curves are presented in Figure 3-4. The accumulation of damage depends on the mix of traffic present on the bridge in the given day.

There is a clear seasonal variation of accumulated apparent damage, with faster growth during summer and slower during winter. This is explained by the temperature variation. During hot summer months, the stiffness of the asphalt pavement is reduced so the response of steel rebar is more pronounced compared with cold winter. It was for this phenomenon that the seasons of daily damage and block maximum were kept.

As mentioned previously, the 5th and 95th fractiles (Figure 3-4) are used to calculate the γ_{CDF} factor. This factor is monitoring time dependent, i.e., the shorter the monitoring duration, the higher the chance that important action effects and their combinations were omitted. Importantly, it is intended to take into account the stochastic nature of traffic only. It does not consider the seasonal variation in damage accumulation, nor it was calibrated with respect to the necessary reliability level of the structure.

The values of γ_{CDF} factor are discussed later, taking into account data from Crêt de l'Anneau viaduct.

Crêt de l'Anneau

Crêt de l'Anneau viaduct was built in 1959 and is composed of eight spans, with total length 195 m. This composite steel-reinforced concrete structure is located in western Switzerland and carries bidirectional road traffic. The slab of variable thickness (17 cm to 24 cm) is fixed to two 1.3 m high steel box-girders. The monitoring was deployed in June 2016[57]. In this chapter six strain gauges are considered. Two strain gauges were installed at span 2, one on transversal and one on longitudinal rebar of slab, located at midspan and centreline of bridge. Another two gauges were installed in same arrangement at span 4. Furthermore, at span 4, one more gauge was installed on the transverse rebar 40 cm from centreline and 60 cm from midspan. The sixth gauge was installed at the bottom of box-girder at midspan. In total, 638 full days of data, registered during 30 months, are taken into account.

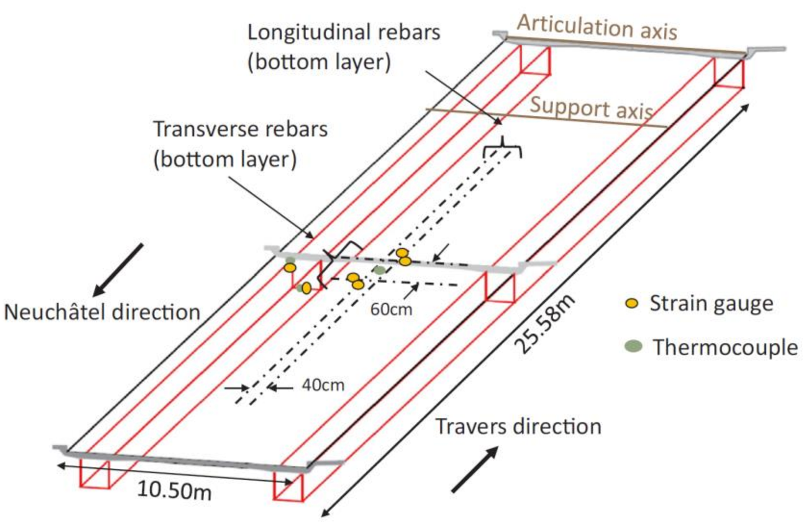

Figure 3-5. Scheme of monitoring of Crêt de l'Anneau viaduct[57].

Discussion

The data from the two viaducts was resampled and processed as discussed previously. The results for all the sensors and starting dates are discussed in this chapter.

Minimum monitoring time

The Time Step Comparison and Normalized Confidence Interval width for all sensors are presented in Figure 3-6 and Figure 3-7. For most of the sensors, the stabilization occurs before 100 days of monitoring.

However, in certain cases the indicator is rising after some monitoring time. These are the transverse strain gauges of Crêt de l'Anneau viaduct. Since the reinforced slab is very thin, the contribution of asphalt pavement to the structural stiffness is important, leading to large variation of structural response depending on the temperature[57]. Thus, the strains registered in summer are higher than those registered in winter. Effect of this phenomenon is most visible for simulations starting in winter (January 1st). After the period of measurements during winter and spring, TSC and NCIW indicators stabilize. Then, daily block maxima registered during hot summer, when registered strains are higher, are added. This leads to increasing indicators presented in Figure 3-6 and Figure 3-7.

This confirms that the presented methods provide reliable results only for stationary data. However, it can be concluded that if the effect of temperature is taken into account otherwise or it is not important, the minimum monitoring time to capture the traffic data reliably is around 100 days. This confirms findings by Treacy et al.[52] as obtained from a monitoring campaign of a reinforced concrete highway viaduct.

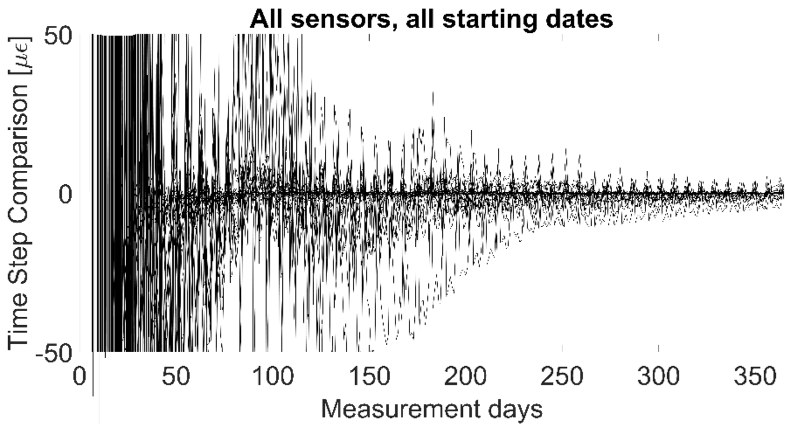

Figure 3-6. Time Step Comparison for eight gauges and four starting dates.

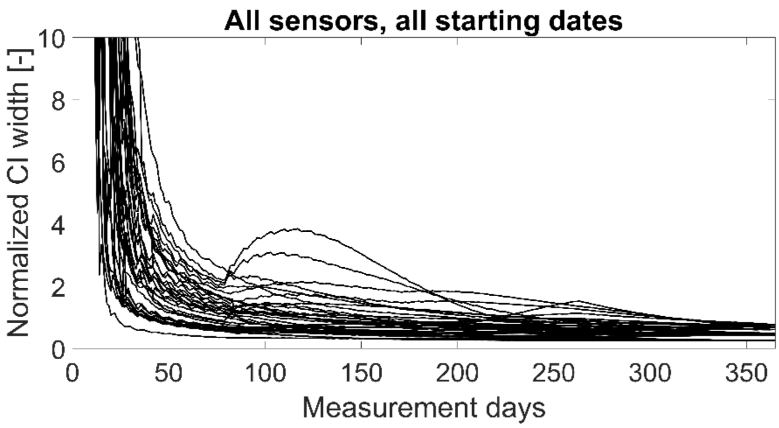

Figure 3-7. Normalized Confidence Interval width for eight gauges and four starting dates.

Optimal monitoring time – correction factor

The daily apparent damage was resampled and treated as described previously. Since the response of the transversal reinforcement bars of Crêt de l'Anneau viaduct is very sensitive to temperature variation, they are discussed separately.

Figure 3-8 presents the Cumulative Damage correction Factor γ_{CDF} prepared on the basis of resampling of accumulated damage of five strain gauges (transversal and longitudinal rebars of Chillon viaduct; longitudinal rebars and box-girder of Crêt de l'Anneau). For most of the sensors, the value of this factor stabilizes around the 50th measurement day. There are two curves with visible peaks around day 70. These are gauges on longitudinal rebars of Crêt de l'Anneau, which registered an extremely heavy truck passage. Nevertheless, the factor reached the value of 4.0 only. Overall, the value of γ_{CDF} factor after full year of monitoring is 1.3.

In the case of transversal rebars of Crêt de l'Anneau, which are highly sensitive to temperature, the convergence rate of the γ_{CDF} factor depends on the starting date of simulation. The results are destabilized, which was discussed previously. Still, the value of factor after full year of monitoring is below 2.5 in all cases, which is considerably lower than the factor of 20 proposed in Eurocode[45].

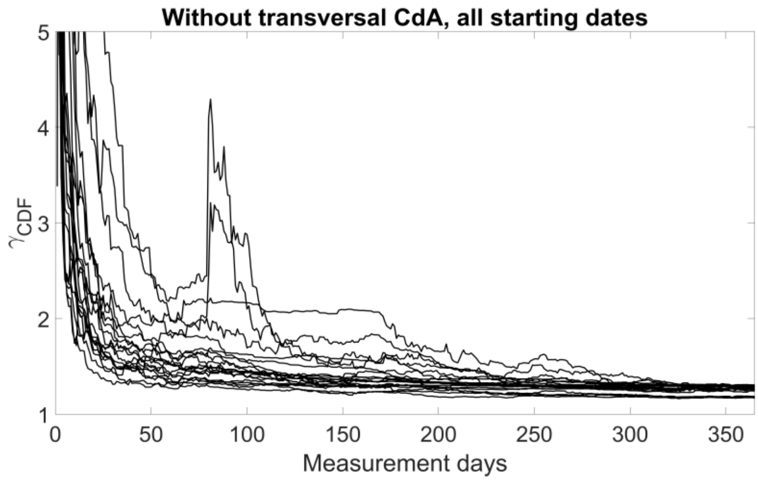

Figure 3-8. Cumulative Damage correction Factor γ_{CDF} based on five gauges (not taking into account transversal rebars of Crêt de l'Anneau) and four starting dates.

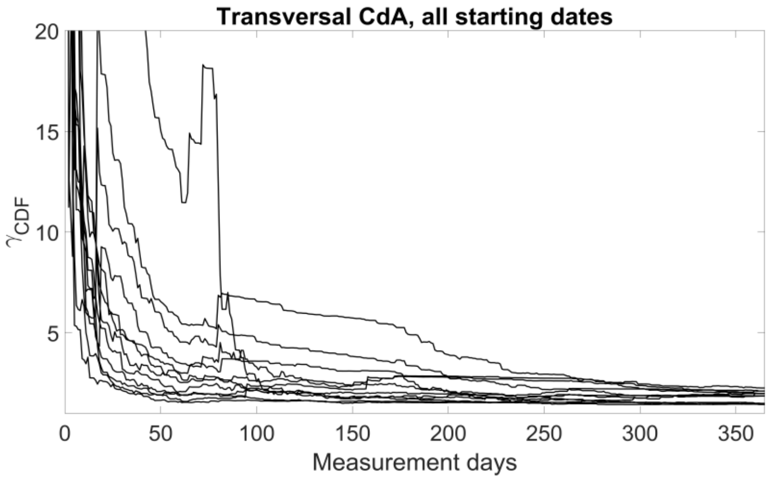

Figure 3-9. Cumulative Damage correction Factor γ_{CDF} based on three gauges (transversal rebars of Crêt de l'Anneau) and four starting dates.

Conclusions

Long term monitoring data from two viaducts was analysed and resampled to investigate the minimum monitoring time required to capture with sufficient reliability the nature of road traffic loading. The method to take into account uncertainty due to short duration of observation in cumulative damage approach is proposed as well. This Cumulative Damage correction Factor does not take into account possible future increase in traffic.

The following conclusions can be drawn:

- The minimum monitoring duration for road bridges is 100 days; if the monitoring is shorter, the collected data cannot be considered as reliable.
- Since the structural response can be highly dependent on ambient temperature, the recommended season to conduct short-term monitoring is during summer months with high temperatures.
- Possible seasonal variation of traffic must be taken into account in the planning of short-term monitoring; however, the two case studies did not reveal such variation as verified with KPSS stationarity test[56] and year-to-year comparison of cumulative fatigue damage.
- For most cases, the Cumulative Damage correction Factor of γ_{CDF}=4 is suggested for cumulative damage extrapolation after 100 days of monitoring, and γ_{CDF}=1.3 after 1 year.
- For highly temperature sensitive structures, factor of γ_{CDF}=20 (or, Eurocode method) should be used for accumulated damage after 100 days of monitoring and γ_{CDF}=2.5 for 1 year-long monitoring; to reduce these values, longer monitoring can be considered.

Chapter 4 Inverse analysis of R-UHPFRC members to determine the flexural response under service loading and at ultimate resistance

On material properties variation in a full-scale element, methods of calculation of stress distribution and tensile-compressive response of UHPFRC under bending action

The content of this chapter was submitted for publication as:

Sawicki, B., Brühwiler, E., Denarié E. Inverse analysis of R-UHPFRC members to determine the flexural response under service loading and at ultimate resistance. *Journal of Structural Engineering*, submitted on 24.11.2020.

Bartłomiej Sawicki was responsible for conceptualization, preparation and execution of experiments including casting of specimens; conceptualization and supervision of semester projects on magnetic NDT calibration; modification of inverse analysis methods for application to full-scale R-UHPFRC beams; modelling; data collection, curation and analysis; conceptualization and preparation of the first draft; edition of the paper.

Ultra High Performance Fiber Reinforced Cementitious composites (UHPFRC) are a relatively new class of building materials. They are composed of a cementitious matrix with fine grains (<1mm) and a high dosage of discontinuous short fibers, usually made of steel (>3% vol.). This material is often combined with steel reinforcement bars to form R-UHPFRC (Reinforced UHPFRC)[58]. Its implementation in structural engineering to rehabilitate and strengthen existing structures and to design and build new structures is rapidly rising in Switzerland[59] and around the world[60–63].

Most of the research on stress distribution in R-UHPFRC members was focused on the ultimate resistance[64–67] or monotonic loading[68,69], without taking into account unloading of the member. An outlook to structural response under service loading with an analytical method of taking into account change of element stiffness due to loading-unloading was discussed previously[70], but without detailed analysis of stress distribution in cross section or composite behavior between steel reinforcement bar and UHPFRC[71].

As far as the ultimate resistance of members determine structural safety, the serviceability state prevails during service duration of a structure. Understanding the behavior of a structure under loading-unloading conditions, for example due to live-loads, and taking into account intrinsic scatter of material properties in the structural member[72] is necessary to eliminate discrepancies between modelled and measured responses[73].

The principle of the inverse analysis is based on modelling of an experiment from which the material properties are indirectly retrieved. Using this method, the direct tensile test, which is difficult to be conducted unequivocally, can be replaced by relatively simple bending tests, and the inherent variation of UHPFRC properties in different elements[72] is quantified. Several inverse analysis methods are available, using simplified closed-form solutions[74–77] as well as numerical[78–80], analytical[81] and finite element methods[82,83], taking into account scatter of material properties in members[74,84]. Inverse analysis can also be done for larger members[85,86]. In this work analytical and numerical FEM methods are used.

This chapter has two objectives: 1) to deduce the stress distribution in R-UHPFRC bended member under loading-unloading action, and 2) to observe the scatter of material performance in small and large UHPFRC elements. Analytical and numerical Finite Element Modelling (FEM) inverse analyses methods are applied to retrieve material properties from bending tests of full-scale members and companion plate specimens. They are compared against results of magnetic Non-Destructive Testing (NDT). The stress distribution in cross sections of R-UHPFRC beams under loading-unloading can be precisely modelled using the identified material properties. The results of modelling are validated with strain values of reinforcement bars measured during experiments.

Methods

Testing of flexural members

UHPFRC plates

The Swiss guidelines for UHPFRC[20] specify four-point bending tests on rectangular plates to obtain the tensile properties of UHPFRC by inverse analysis of experimental results. Plates of width b_m and thickness h_m are tested under four-point bending over a span l_m and force application points spaced at $l_m/3$, as shown in Figure 4-1. Force and mid-span deflection are recorded during testing. The material properties are obtained by inverse analysis methods.

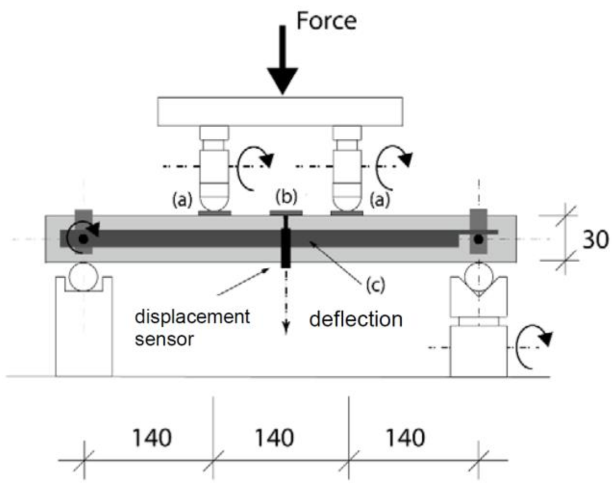

Figure 4-1. Four-point bending test of plate specimens to determine the tensile properties of UHPFRC according to SIA 2052; dimensions in mm, width 100 mm.

R-UHPFRC flexural beams

In this chapter, 10 beams of three different types (Figure 4-2) are discussed, and each of the members has been casted separately. Three beams of Type I, three beams of Type II and two beams of Type III have been tested under quasi-static loading until failure. Additionally, one beam of Type II and one beam of Type III have been tested under loading-unloading cycles to investigate the structural behaviour under service conditions.

Beams of Type I contain one rebar of diameter Ø20 mm, and the cover thickness is c_{nom} = 10 mm, thus Ø/2. Beams of Type II are reinforced with one rebar Ø34 mm and c_{nom} = 17 mm, thus Ø/2. Type III members contain one longitudinal rebar Ø20 mm with c_{nom} = 10 mm and Ω-shaped ⌀6 mm stirrups (Figure 4-2). Although Types I and III have the same longitudinal reinforcement (Ø20 mm), the rebars were fabricated and delivered separately, and thus they are treated disjointly.

All the beams were casted in horizontal position (as tested), pouring fresh UHPFRC from the top at one end. Six external vibrators attached to walls of the formwork assured good flow of the mix. After casting, the formworks were covered with foil for 7 days. Then the beams were unmolded, wrapped in the foil and transported to storage area.

The beams were subjected to quasi-static displacement-controlled four-point bending tests. The constant bending moment zone varied between 0.2 m and 0.7 m as indicated in Figure 4-2, to prevail the bending failure mode over shear failure. The displacement was applied using a servo-hydraulic actuator and transmitted with use of a hinge and a steel beam. The resultant force was measured using the load cell of the actuator. For groups II and III, foil strain gauges were glued on rebars at midspan and ±200 mm from midspan before casting.

Commercially available UHPFRC mix Holcim710® was used, with 3.8% vol. 13 mm straight steel fibers with aspect ratio 65. The minimum age at the moment of testing was three months. The cement hydration in UHPFRC is advanced after 28 days and stops almost completely after 90 days[87], thus it was assumed that the age has no influence on the material properties. To verify this, the companion plates were tested under four-point bending at 28 and 90 days after casting, which is discussed later.

The mean compressive strength obtained by testing of cylinders 70 mm x 140 mm in direct compression at 28 days according to Swiss standard is f_{Uc} = 140.7 MPa

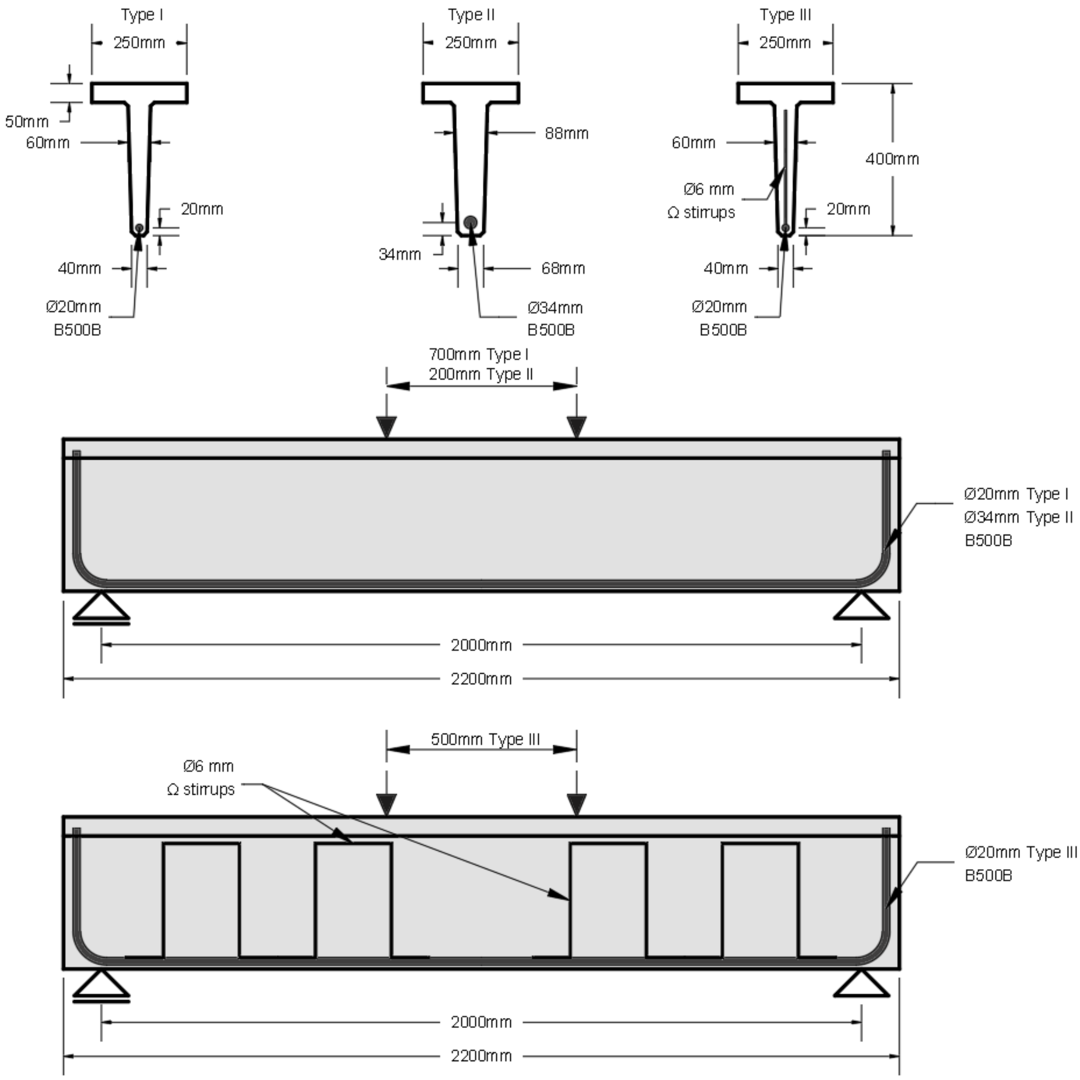

Figure 4-2. Three types of beams tested under four-point bending.

Table 4-1. Mean tensile material properties of reinforcement bars based on axial tensile tests.

Beam type	f_s [MPa]	f_t [MPa]	ε_u [‰]	E_s [GPa]
Type I (Ø20 mm)	600	687	9.2	224
Type II (Ø34 mm)	525	624	9.4	245
Type III (Ø20 mm)	512	617	9.2	234

Both longitudinal reinforcement and stirrups are of type B500B according to Swiss standard[43] and Eurocode[42], with theoretical characteristic yielding strength f_{sk}=500MPa. The properties of longitudinal reinforcement obtained using direct tension test according to Swiss standard are presented in Table 4-1. The rebars used in Type I beams have higher strength, however they still meet the requirements of B500B reinforcement class.

Inverse analysis

Analytical methods

Inverse analysis methods for an element under four-point bending are based on sectional stress distribution. Stress and strain values are sought for the three points A, B and C according to Figure 4-3a) on the force – deflection curve.

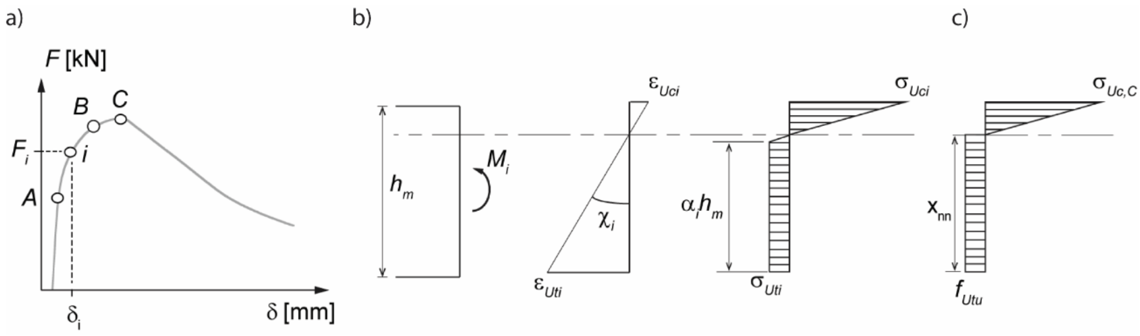

Figure 4-3. Principle of inverse analysis of four-point bending test [21].

The point A indicates the end of linearity of force (F)-deflection (δ) curve, implying loss of elasticity of the material. Sectional stress distribution and deflection at this point can be calculated using the elasticity theory, obtaining Young's modulus E_U and elastic limit stress f_{Ute}. Alternatively, E_U can be calculated for each F-δ pair. The point A is detected where irreversible drop of E_U occurs.

The ultimate resistance of the element is reached at point C. Using a stress block in tension and elastic response in compression for UHPFRC, knowing both the position of the neutral axis and the acting bending moment as well as employing the sectional force equilibrium, the tensile resistance of UHPFRC f_{Utu} is found (Figure 4-3 c)). In case of R-UHPFRC members the contribution of the reinforcement bar is taken into account as well under assumption of perfect bond.

The point B marks the moment when softening behavior of UHPFRC comes into play. It is detected with iterative methods to identify the loss of agreement between experimental deflection-force curve and the one obtained analytically using a simplified material model with stress cut-off at f_{Utu}. The lack of agreement indicates loss of validity of the model without post-peak resistance and thus beginning of the softening behavior contribution of UHPFRC in bending resistance.

Plates, method I

The analytical inverse analysis method described in Swiss UHPFRC recommendations[20] was proposed by[80]. This method is based on finding three points: A, B and C, separately.

To determine point A, apparent secant moduli E_i are found for each δ_i-F_i pair according to

Equation 4-1

$$E_i = 0.0177 \cdot \frac{F_i}{\delta_i} \cdot \frac{12 \cdot l_m^3}{b_m \cdot h_m^3}$$

The moving average E_{mi} over 20 values of E_i is computed and the curve δ_i – E_{mi} plotted. The point A corresponds to the deflection δ_A for which an irreversible decrease of more than 1% of the value E_{mi} occurs. The modulus of elasticity E_U is equal to E_{mi} at point A and the elastic limit stress f_{Ute} is calculated by taking F_A at this point and assuming linear elastic stress distribution over the section:

Equation 4-2

$$f_{Ute} = \frac{F_A \cdot l_m}{b_m \cdot h_m^{\ 2}}$$

A simplified formula to obtain f_{Utu} is used at point C. It is based on the following assumptions: sectional force equilibrium, linear elasticity of material in compression and position of neutral axis at $0.82h_m$ for this specimen geometry. These assumptions were confirmed by direct tensile tests and numerical modeling[80].

Equation 4-3

$$f_{Utu} = 0.383 \cdot \frac{F_C \cdot l_m}{b_m \cdot h_m^{\ 2}}$$

To detect point B the curvature in the constant moment zone is assumed to remain proportional up to the peak force according to equation[74]:

Equation 4-4

$$\chi_i = \frac{216}{23} \cdot \frac{\delta_i}{l_m^{\ 2}}$$

For each pair δ_i-F_i the bending moment M_i and further the tensile stress σ_{Uti} and strain ε_{Uti} on the bottom face of the specimen in the constant bending moment zone are computed, according to Equation 4-5 to Equation 4-7:

Equation 4-5

$$M_i = \frac{F_i \cdot l_m}{6}$$

Equation 4-6

$$\sigma_{Uti} = 0.5(1 - \alpha_i)^2 h_m \chi_i E_U$$

Equation 4-7

$$\varepsilon_{Uti} = \frac{\sigma_{Uti}}{E_U} + \chi_i \alpha_i h_m$$

For simplification, the parameter λ_i is defined by the following equation:

Equation 4-8

$$\lambda_i = \frac{12M_i}{\chi_i E_U b_m h_m^{\ 3}}$$

Equilibrium in the cross-section yields:

Equation 4-9

$$2\alpha_i^3 - 3\alpha_i^2 + 1 - \lambda_i = 0$$

These values are computed for a series of points evenly distributed between points A and C. At least 10 points are recommended and the first point should be taken such that $\lambda_i = 0.5$ ($\alpha = 0.5$) to obtain a representative result for the whole cross-section. The first point $_j$ for which the calculated $\sigma_{Utj} > f_{Utu}$ is taken as point C, and thus the value of strain-hardening deformation of UHPFRC is $\varepsilon_{Utu} = \varepsilon_{Utj}$.

Plates, method II

The second method of inverse analysis for plates uses the same principles, but the points A and B are found together and the whole force-deflection curve is fitted between them[88]. First, the tensile strength f_{Utu} is calculated using Equation 4-3.

Then, the F-δ curve is computed on the basis of the assumed material properties. A set of α values (see Figure 4-3) is prepared. The minimum recommended number of points is 10. The points should range from α=0 (elastic state) to an α–value such that the stress on the bottom face in the constant bending moment zone becomes $\sigma_{Uti} > f_{Utu}$.

For each point, the neutral axis position in relation to the specimen height is calculated based on force equilibrium, and:

Equation 4-10

$$x_{n-n,i} = 0.5 + \frac{{\lambda_i}^2}{2}\left(1 - \frac{E_{Uh}}{E_U}\right)$$

where the hardening secant is computed as

Equation 4-11

$$E_{Uh} = \frac{f_{Utu} - f_{Ute}}{\varepsilon_{Utu} - \frac{f_{Utu}}{E_U}}$$

The curvature in the constant bending zone is

Equation 4-12

$$\chi_i = \frac{\frac{f_{Ute}}{E_U}}{h_m \cdot \left(x_{n-n,i} - \alpha_i\right)}$$

The strain at the bottom face is computed assuming plane sections with the cutoff limit at ε_{Utu} since the softening material behavior is not taken into account:

Equation 4-13

$$\varepsilon_{Uti} = \frac{f_{Ute}}{E_U} \cdot \left(1 + \frac{\alpha_i}{x_{n-n,i} - \alpha_i}\right)$$

Using the obtained strain distribution and assumed material properties, the stresses on the bottom and upper faces of the plate are computed, denoted as σ_{Uti} and σ_{Uci} respectively. The deflection δ_i is calculated transforming Equation 4-4. The bending moment M_i is found transforming Equation 4-8 with respecting the sectional equilibrium determined by Equation 4-9 and the resultant force F_i is computed using Equation 4-5.

In this way, a series of pairs F_i - δ_i is plotted against the load-deflection curve obtained from testing. The first point (α_i = 0) is point A, thanks to which the elastic limit stress f_{Ute} and modulus of elasticity E_u are found. The point where the two curves are diverging is point B. By varying ε_{Utu} such that the measured and computed curves are similar and that point B is shifted as far as possible towards the peak force, the inverse analysis is completed.

R-UHPFRC members

Principles of method I for plates are adopted for R-UHPFRC flexural members. After recording the force F - deflection δ curve during the test, the secant modulus E_i at each measurement point is calculated. The material remains elastic thus α = 0, and Equation 4-9 yields λ = 1. Taking the Equation 4-4, and in analogy with Equation 4-8 the following equation is obtained:

Equation 4-14

$$E_i = \frac{23 \cdot {l_m}^2 \cdot F_i \cdot (l_m - b_m)}{864 \cdot \delta_i \cdot I}$$

Where b_m is the distance between the load application points and I is inertia of the beam at elastic state. Similarly as for plate specimens, the point A is found, and the stress on the bottom face being the elastic limit stress f_{Ute} is obtained using Euler-Bernoulli elastic beam theory.

At point C the position of the neutral axis $x_{n\text{-}n}$ needs to be located to get the tensile strength f_{Utu}. For each type of the beam, $x_{n\text{-}n}$ is found separately, using extensometers installed over the height of beam. Once the position is known, and under the assumption of elastic material response in compression and elastic-plastic in tension (Figure 4-3 b)), the f_{Utu}–value is found respecting the cross-sectional force balance and the acting bending moment at point C.

Instead of finding point B, another method is used for the determination of ε_{Utu}. In R-UHPFRC members, thanks to the composite action of both materials and favorable orientation of fibers in vicinity of the rebar, the tensile properties of UHPFRC are significantly better than in case of non-reinforced element. The tensile strain-hardening domain and thus the ε_{Utu} value increases up to 5 times when rebar B500B is used[89,90]. In analogy with the simplified elastic-plastic material model from the Swiss standard[20], it is assumed that the tensile strain hardening value of the UHPFRC is equal to $2\varepsilon_{Utu}$. This was validated by finite element modelling of the discussed R-UHPFRC beams. Under strain of $2\varepsilon_{Utu}$ in critical cross-section 97% of the ultimate resistance was achieved in average for three types of beams.

Finite Element Modelling

The inverse analysis using FEM is based on finding the material model such that the computed and experimental structural response are in good agreement. The commercial DIANA® FEA [91] software was used similarly as by Sadouki et al.[92].

A 2D model of the plate specimen subjected to four-point bending was built using plane stress rectangular 5 mm x 5 mm finite elements. The elastic, strain-hardening and softening material response is simulated using an elastic – multi directional fixed crack model. The localization of the fictitious crack along the element is determined by dividing the constant bending moment area into vertical zones. One of them, corresponding to the location of the critical section in the tested specimen, is modelled using the nominal material properties while the rest of the plate is modeled using the material model with the same modulus of elasticity E_U, elastic limit stress f_{Ute} and hardening modulus E_{UH} but higher tensile strength f_{Utu}. The constitutive law of UHPFRC including the beginning of softening branch is varied until obtaining a similar force – deflection response as in the experiment. The experiment is modelled until the ultimate member resistance is reached using a nonlinear solver with variable loading steps. The load introduction as displacement by means of nonlinear springs that are acting in compression, only reflects the possibility of loss of contact between the testing machine and the plate.

Similar method is used for modeling of the R-UHPFRC beams. The T-shaped cross-section is modelled by division of the 2D model into six horizontal parts. The uppermost part is representing the flange, and the remaining five parts are composing the web. The variable web thickness is modelled through stepwise variation of the thickness such that the error of the moment of inertia of the beam is below 1%. The longitudinal rebars are modelled as straight, horizontal, perfectly anchored bars. Additionally, to avoid crushing of singular elements, 200mm long and 20mm thick steel plates are added, respecting the theoretical static scheme of the beam. The size of elements is same like for the plates, i.e. 5 mm x 5 mm.

Only the material model of UHPFRC is fitted. The material properties of rebars are adopted as elastic-perfectly plastic using the average material properties as obtained from testing, relevant for each type of beam.

Material model of UHPFRC

The UHPFRC is a composite material made of a cementitious matrix and fibers. Due to this bi-component structure, the UHPFRC shows quasi bi-linear behavior under direct tension before reaching its tensile strength (Figure 4-4).

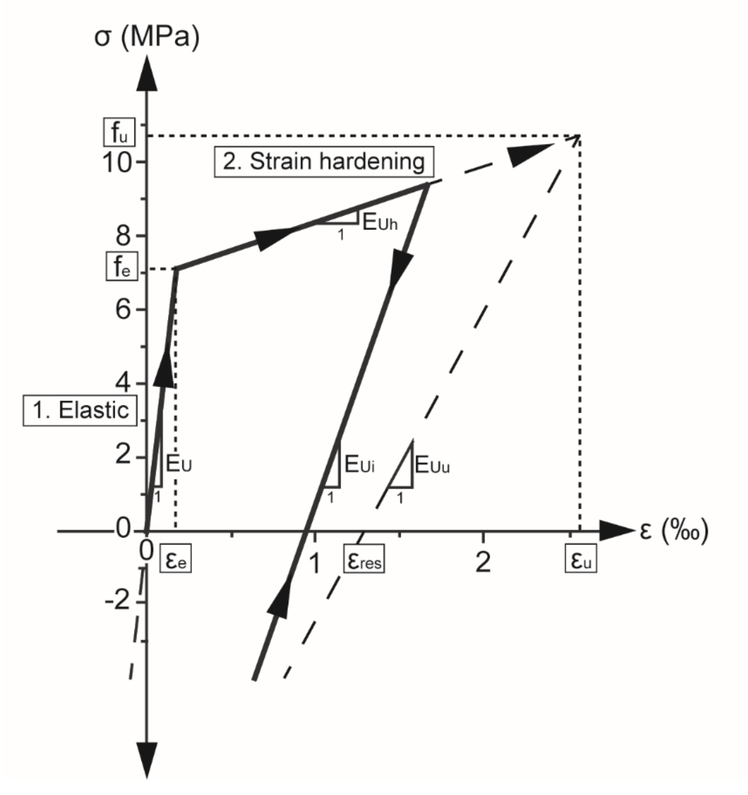

Figure 4-4. Simplified UHPFRC constitutive law under loading-unloading in tension.

The first stage is elastic. The behavior of UHPFRC is linear with Young's modulus E_U and after unloading the strain comes back to zero.

After the elasticity limit (f_e, ε_e, Figure 4-4) is reached, uniformly distributed discontinuities in the matrix start to occur and the material develops in the strain-hardening domain with strain-hardening secant E_{Uh} defined by Equation 4-11. From the macroscopic point of view, the material can be considered as a continuum, however increasingly anisotropic as hardening develops.

When UHPFRC is in the strain-hardening domain, after unloading the residual strain ε_{res} remains. When the tensile strength is reached, the unloading secant is calculated according to:

Equation 4-15

$$E_{Uu} = \frac{f_u}{k_u \cdot \varepsilon_u}$$

where $k_u=0.5$ for UHPFRC with straight steel fibers[93]. Under renewed tensile action, the response follows E_{Uu} until the previously imposed stress is reached. If the tensile stress if further increased, the material follows the envelope strain-hardening curve shown in Figure 4-4.

In the current work it is assumed that the unloading secant E_{Ui} varies linearly from E_U to E_{Uu} between ε_e and ε_u respectively, which lies in agreement with behavior of fiber reinforced mortar at the onset of matrix cracking[94]. To the authors best knowledge, there was no study on the behavior of UHPFRC in compression after previously reaching the strain-hardening domain in tension. Tensile strain-hardening cement-based composites with steel fibers seem to follow unloading secant E_{Ui} at the first stage of compressive response[95], and this was adopted in the current work.

The UHPFRC in compression, without pre-loading in tension, behaves linear elastically with E_U up to the compressive strength f_{Uc}.

Calculation of stress distribution in the cross-section

The stress distribution in the R-UHPFRC beam is computed using Euler-Bernoulli elastic beam theory and numerical methods. Perfect bond between reinforcement bar and UHPFRC is assumed[89].

The UHPFRC cross-section of the beam is discretized into 100 horizontal layers of equal thickness taking strain at each layer being uniform. The elastic – strain-hardening material model in tension and perfectly elastic model in compression is adopted for UHPFRC during the first loading. The elastic – perfectly plastic model is adopted for the steel reinforcement bar.

The linear strain distribution is governed by the strain ε in the bottom of member and by the position of the neutral axis $x_{n\text{-}n}$. For given $x_{n\text{-}n}$, strain distribution in the UHPFRC and rebar is calculated. Based on the material model, stress in each layer and in the rebar is obtained. Resultant forces are computed by respecting the beam geometry. The neutral axis $x_{n\text{-}n}$ is finally found when the sum of sectional forces is $\sum F=0$. Then, the resulting bending moment for the corresponding ε is calculated. The procedure is automated in such a way that for a given bending moment, the unique pair of ε and $x_{n\text{-}n}$ is found, and thus the distribution of stress is determined.

Once the stress distribution for the maximum pre-loaded bending moment M_{max} is calculated, the loading-unloading cycle is obtained, and the unloading secants E_{Ui} and residual strains $\varepsilon_{res,i}$ depending on the reached stress, are computed and stored for each UHPFRC layer. To find the strain distribution at the minimum un-loaded bending moment M_{min}, a new pair of ε and x_{n-n} is found. The UHPFRC layers that entered into the strain-hardening phase at M_{max} follow the unloading secant E_{Ui} stored previously. Importantly, if in any layer the obtained strain is such that $0<\varepsilon<\varepsilon_{res,i}$, the stress in the UHPFRC is negative (i.e. compressive stress) despite a positive strain value (see Figure 4-4).

Magnietic NDT

The distribution of tensile strength f_{Utu} in an UHPFRC element depends on local orientation and content of fibers[72,96] and can be approximated for straight fibers as follows[97,98]:

Equation 4-16

$$f_{Utu} = \mu_0 \cdot \mu_1 \cdot \tau_f \cdot V_f \cdot \frac{l_f}{d_f}$$

where τ_f is an average fiber pull-out stress; V_f, l_f and d_f are the fiber volumetric content, length and diameter, respectively.

The fiber orientation factor μ_0 reflects the probability that a fiber crosses a given section. Under the assumption of homogenous fiber distribution, factor μ_0 is determined as ratio between total area of fibers in the section to fiber volume fraction[99,100]:

Equation 4-17

$$\mu_0 = \frac{n_f \cdot A_f}{V_f}$$

The fiber efficiency factor μ_1 considers the angle between the cross-section and the fiber crossing[89,101]. In a structural element, it is dependent from μ_0[102]. The two factors can be precisely obtained using image analysis of specimen surfaces extracted from elements[72,103] and destructive testing[102], but for sake of applicability to the real structures non-destructive techniques (NDT) should be used.

Using the fact that in most UHPFRCs steel fibres are used, their magnetic inductance L can be exploited to establish μ_0 and μ_1[104,105]. After measuring the magnetic inductance on the element surface in two directions as well as inductance of the air (L_x, L_y and L_{air} respectively) the magnetic permeability is found:

Equation 4-18

$$\mu_{r,i} = \frac{L_i}{L_{air}}$$

Using the linear dependence of mean magnetic permeability ($\mu_{r,mean} = (\mu_{r,x} + \mu_{r,y})/2$) on fiber content and that for $V_f = 0\%$ the permeability $\mu_{r,mean} = 0$, the slope of linear regression is determined. This slope is dependent on the type of fiber used[106] and is later used to calculate the local V_f at the measurement point. Slope values ranging from 3.8 to 4.55 can be found in the literature[105,107].

Using the fiber orientation $(\rho_x - \rho_y)$, the factors μ_0 and μ_1 are obtained [104]:

Equation 4-19

$$(\rho_x - \rho_y) = 0.5\frac{\mu_{r,x} - \mu_{r,y}}{\mu_{r,mean} - 1}$$

Equation 4-20

$$\mu_0 = 0.57 + 1.85(\rho_x - \rho_y)$$

Equation 4-21

$$\mu_1 = \begin{cases} 1.686 \cdot \sqrt{\mu_0} - 0.406, & \mu_0 < 0.7 \\ 1.0, & \mu_0 \geq 0.7 \end{cases}$$

Magnetic NDT calibration

Since the magnetic permeability of UHPFRC depends on the fiber type[105], the calibration for the UHPFRC mix used in this research was performed. Due to the circular magnetic flux produced in the U-shaped sensor (Figure 4-5), a certain effective depth is penetrated depending on the power of the magnetic field. For the sensor similar to the one used in the present study, but with smaller operating voltage (0.1 V), the effective depth was found to be equal to 25 mm[108]. As according to Lenz's law the inductance is proportional to electromotive force, it can be expected that the effective depth increases with higher voltage in the coil. If the effective depth of sensor is higher than the thickness of element used for calibration, the method cannot be used for elements of a different thickness. In the current study 2 V current was chosen as in Nunes et al.[105], thus it was decided to perform the calibration on specimens specially prepared for this purpose instead of plates serving for material testing (30 mm thick).

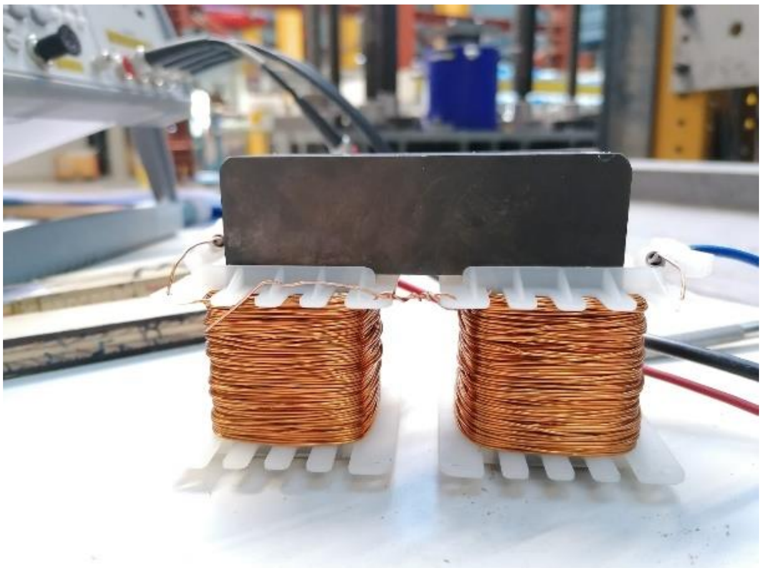

Figure 4-5. Magnetic sensor used for NDT of UHPFRC tensile resistance.

Four plates 40 mm x 200 mm x 1500 mm were casted vertically to mock-up the web of the T-shaped beam (Figure 4-6). To assure non-uniformity of fiber alignment and distribution as well as to obtain more calibration points for the method, four different methods of casting were applied: a) casting from the top at one end, no vibrating, b) from the top at one end with vibrating after casting, c) from the top at one end with vibrating during and after material placing, and d) from the top at two ends with vibrating during and after material placing.

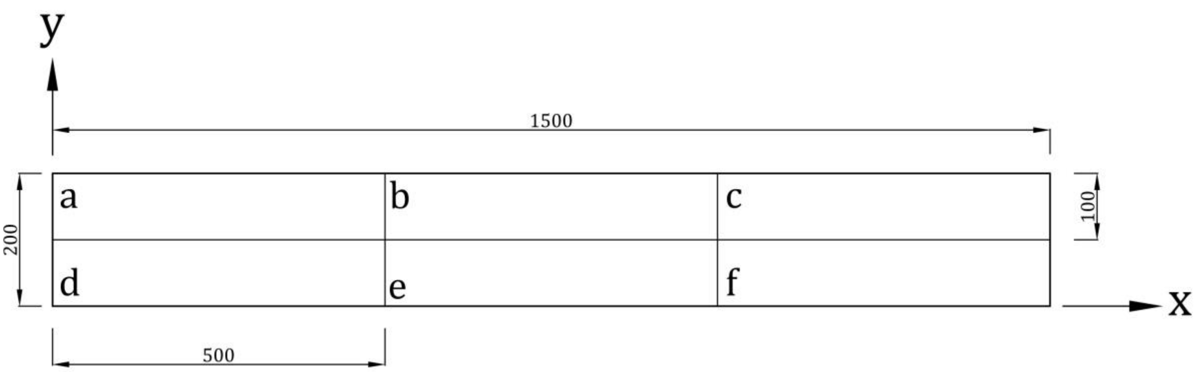

Figure 4-6. Plates used for calibration of magnetic NDT method, thickness 40 mm.

After 28 days, the magnetic inductance was measured along the plates, in two directions. The plates were cut to obtain 6 specimens from each plate (a to f, Figure 4-6) of dimensions similar to the bending tensile test specimen according to Swiss standard[20] and tested under four-point bending to obtain f_{Utu} as described previously. Despite the bigger thickness compared to the standard specimens, the same stress distribution at ultimate resistance was assumed[85].

Assuming uniform V_f = 3.8% in all specimens, the slope of regression curve is found[105] to be equal to 4.59. Since the magnetic measurements on webs of T-shaped beams under same assumption yielded the average of slopes 4.64, it is accepted that:

Equation 4-22

$$\mu_{r,mean} = 1 + 4.6V_f$$

Importantly, no correlation between the web thickness of T-beams and fitted slopes could be found. This confirms that the effective depth of the sensor is smaller than the thickness of plate used for calibration.

After finding the local V_f as well as the factors μ_0 and μ_1 for measurement points at the critical section of tested plates, fiber pull-out shear stress for this kind of mix can be estimated. Using Equation 4-16, τ_f = 7.5MPa which corresponds well with values obtained in pull-out test of fibers with the same diameter (6.9MPa to 10MPa)[103,109]. Hereby the method is calibrated for the current UHPFRC mix and can now be used for f_{Utu} calculation. The results obtained with destructive and non-destructive values during calibration are presented in Figure 4-7. Noteworthy the rather large scatter of f_{Utu} is due to the different casting methods and should not be associated with the material variation in the T-shaped beams.

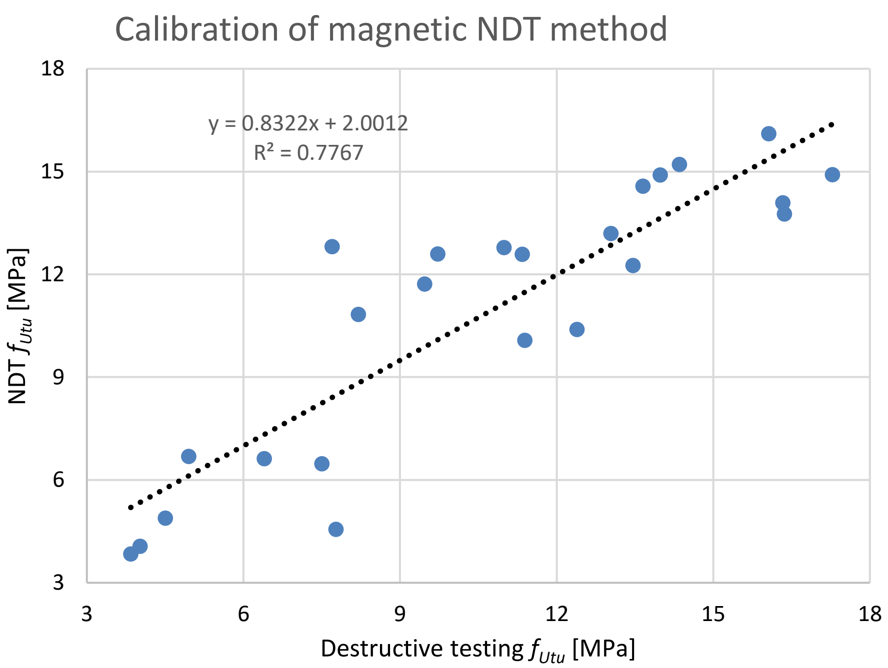

Figure 4-7. Calculation of tensile resistance f_{Utu} using calibrated magnetic NDT.

UHPFRC properties

Comparison of FEM and analytical methods for inverse analysis of plates

For some of the plates tested in four-point bending, the finite element modelling was used to verify agreement between both analytical inverse analysis methods. Representative specimens for each group were chosen. Specimens with critical cross-section close to the mid-span were favored since the two analytical methods should be more precise at this location and thus the comparison more reliable. The comparison of material properties obtained for 9 plates of 48 in total, from different castings, at 28 and 90 days, using three methods is presented in Table 4-2.

Table 4-2. Tensile properties of UHPFRC obtained for 9 plate specimens using both analytical methods and finite element modelling.

Plate	Method I				Method II				FEM			
	f_{Ute} [MPa]	f_{Utu} [MPa]	ε_{Utu} [‰]	E_U [GPa]	f_{Ute} [MPa]	f_{Utu} [MPa]	ε_{Utu} [‰]	E_U [GPa]	f_{Ute} [MPa]	f_{Utu} [MPa]	ε_{Utu} [‰]	E_U [GPa]
1	5.5	13.2	3.6	43.7	10.0	13.2	2.0	42.0	9.0	13.5	2.2	43.7
2	9.5	12.5	2.3	43.3	8.5	12.5	1.3	46.0	9.5	13.0	1.9	43.3
3	6.1	12.1	5.6	43.1	9.0	12.1	3.5	43.5	6.5	12.1	2.6	43.1
4	6.0	9.0	1.5	42.0	8.0	9.0	1.2	42.0	6.0	7.5	1.5	42.0
5	4.3	10.2	3.3	40.2	7.9	10.2	2.2	40.0	6.5	10.2	2.8	40.2
6	3.5	10.7	3.7	45.2	4.0	10.7	1.2	43.0	5.0	10.5	1.4	43.0
7	4.1	8.6	1.1	33.8	4.0	8.6	0.8	35.0	4.1	9.0	0.5	33.8
8	3.8	12.2	4.1	40.2	8.2	12.2	2.4	34.0	6.0	14.0	3.2	40.2
9	5.9	13.5	4.2	40.0	7.0	13.5	2.5	38.0	7.0	15.0	3.0	40.0

It can be noticed that the elastic limit stress f_{Ute} obtained with FEM is between the values obtained with the analytical methods (except for plate 6). The same is observed for strain hardening deformation ε_{Utu} (except for plates 3 and 7). Similar ultimate tensile strength f_{Utu} was obtained with all methods, while the variation was below 15%.

The discrepancy between results obtained with each method visualizes the difficulty of fitting point A in the analytical inverse analysis procedure. FEM should give the most precise results since the critical crack is modelled exactly where it appeared. Furthermore, the full sectional stress distribution is obtained instead of a simplified one. Since the results obtained with FEM are between results of analytical analysis it can be stated that both methods approach the solution from two sides. The importance of these discrepancies is discussed later in this chapter.

Limit of elasticity and modulus of elasticity

The Young's modulus E_U and elastic limit stress f_{Ute} obtained with inverse analysis of all tested plates are presented in Table 4-3. The average values for each type of beam tested to failure is given as well. The mean values (μ) and standard deviations (σ) were computed for six plates in each test series after 28 and 90 days.

Table 4-3. Modulus of elasticity and elastic limit stress obtained for beams and plates using analytical and finite element modelling methods.

Type	Age	Plates analytical method type								Beams			
		I f_{Ute} [MPa]		II f_{Ute} [MPa]		I E_U [GPa]		II E_U [GPa]		f_{Ute} [MPa]		E_U [GPa]	
		μ	σ	μ	σ	μ	σ	μ	σ	Anal.	FEM	Anal.	FEM
I	28d	6.37	0.63	8.27	1.55	41.9	1.5	43.8	3.4	8.3	10.1	36.0	36.0
	90d	6.20	1.63	7.70	1.81	41.9	2.3	42.4	3.7				
II	28d	5.51	1.01	6.82	0.57	39.5	2.9	40.2	2.8	9.8	9.0	37.7	36.5
	90d	4.22	0.61	4.63	0.57	41.3	3.1	42.0	2.7				
III	28d	3.71	0.46	7.2	3.17	37.8	2.5	35.2	1.8	4.4	3.7	30.5	31.8
	90d	5.14	0.96	7.58	0.68	39.3	2.0	37.0	3.0				

Comparison of the results shows that no change of properties occurred between 28- and 90-days age. Only for f_{Ute} obtained with method II for group II the two mean values lie outside of 2σ interval indicating a scatter that is larger than expected assuming normal distribution of properties.

The elastic limit stress f_{Ute} for plates is smaller than for beams, confirming the beneficial influence of reinforcement on material properties[89]. On the contrary, obtained E_U is higher for plates than for beams. This may be explained by shear deformation neglected in calculation of deflection in inverse analysis.

The inverse analysis method II for plates gives in average 36% higher elastic limit stress f_{Ute} than with method I, with the special case of Type III casting after 28 days where this parameter almost doubles. This may be due to lack of rapid loss of stiffness or regaining it at further stage due to the fiber orientation and content stratification in the specimen. In the same time, the moduli of elasticity E_U found with the two methods are similar and the average scatter is below 1%.

The elasticity limit of beams Type III is lower than for other types. It was probably provoked by early age shrinkage cracking due to: a) lower matrix tensile resistance because of age of premix (>1 year) and b) addition of omega stirrups that changed restraint level of setting mix. Only for this group of beams, localized microcracks were detected after spraying with alcohol before loading. Such defects are not considered in inverse analysis, lower apparent elasticity limit and thus elastic limit stress are obtained. This group of beams was casted one year after other specimens, with the same material.

Tensile strength

The tensile strength f_{Utu} and hardening strain ε_{Utu} obtained with inverse analysis of plates are presented in Table 4-4 together with values obtained for respective beams. The average value for each type of beams tested to failure is given. The mean values (μ) and standard deviations (σ) are given for each series of tests after 28 and 90 days.

The mean f_{Utu} for beams obtained with magnetic NDT is presented in Table 4-4 as well. The average value for each beam was taken because the influence of fiber non-uniformity is negligible for the overall resistance of the beam[106] in R-UHPFRC members. Still, it determines the failure crack location[110].

The estimated hardening strain ε_{Utu} is lower using the analytical inverse analysis method II by around half comparing to method I. Similar ε_{Utu} values for beams is obtained with the analytical method compared with the FEM method.

Similar f_{Utu} values for plates and beams are obtained with all methods except for beam Type III. As mentioned previously, due to the early age cracking the apparent material strength is lower in the beams from this group.

Table 4-4. Tensile strength and hardening strain obtained for beams and plates using analytical and finite element modelling methods.

Type	Age	Plates analytical method type						Beams				
				I		II						
		f_{Utu} [MPa]		ε_{Utu} [MPa]		ε_{Utu} [GPa]			f_{Utu} [MPa]		ε_{Utu} [GPa]	
		μ	σ	μ	σ	μ	σ	Anal.	Num.	NDT	Anal.	Num.
I	28d	11.8	2.1	3.6	1.5	2.1	1.0	12.7	12.8	13.0	3.8	2.7
	90d	12.3	2.0	3.4	1.0	1.6	0.5					
II	28d	10.6	0.7	3.4	1.0	1.5	0.4	11.8	11.2	11.6	2.2	2.6
	90d	11.1	0.8	4.0	1.0	1.3	0.2					
III	28d	11.6	2.8	2.6	1.4	1.6	0.8	7.3	7.3	9.1	2.9	2.4
	90d	12.0	1.5	3.4	0.9	2.1	0.5					

Ultimate resistance of members

To quantify the influence of variation of material properties obtained with different methods, the computed ultimate resistance of beams is compared with testing results. The simplified method from the Swiss UHPFRC standard[20] is used (Figure 4-8).

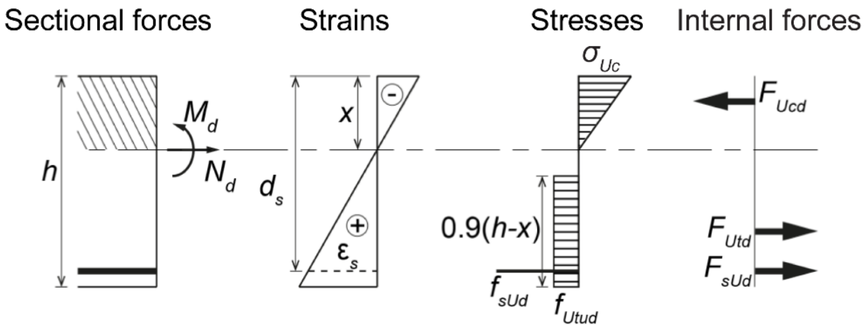

Figure 4-8. Simplified resistance model for UHPFRC members to determine the ultimate resistance, according to SIA 2052.

The method assumes that the plain sections remain plain and that both reinforcement and UHPFRC in tension are fully activated. The tensile stress block of UHPFRC is taken as 90% of height below the neutral axis to consider the fact that part of the material is in the elastic state. Then, the neutral axis can be found to comply with force balance in the cross-section. For the sake of comparison, the mean values of resistance are used here. As mentioned before, strain at the bottom of the beam is assumed to be equal to $2\varepsilon_{Utu}$ per analogy to SIA 2052[20], and supported by FEM simulations. For values based on magnetic NDT, the ε_{Utu} and Eu mean values obtained from plates using method I for respective type of beams are adopted. To quantify the composite behaviour of reinforcement and UHPFRC, the ratio Q of sectional tensile force shared between them is presented in Table 4-5 as well.

Table 4-5. Experimental and calculated bending resistance of beams.

Beam/Method	Test [kNm]	Method I [kNm]	Method II [kNm]	NDT [kNm]	Beam anal. [kNm]	*Q* [-]
Type I	109.2	107.8	105.2	110.2	108.9	0.98:1
Type II	230.4	213.6	203.4	217.1	228.8	1.54:1
Type III	82.2	97.7	95.5	89.1	86.1	0.94:1

The bending resistance based on material testing for groups I and II lays consistently below the experimental value of ultimate resistance, but within a 10% margin showing thus good agreement. For group III, the ultimate resistance is overestimated by 20% due to previously mentioned early age shrinkage cracking of the matrix. Importantly, the ultimate resistance value determined using the f_{Utu} value obtained by NDT gives closer results than based on values from material testing. This is because the fiber orientation and content variation can be correctly grasped by the NDT method. The ultimate resistance based on the inverse analysis methods of beams is shown for the sake of comparison to quantify the error of the model. Finally, it can be noted that the smaller rebars (Ø 20mm) contribute as much as UHPFRC to tensile sectional force, and the contribution of UHPFRC decreases with increase of rebar diameter to 34mm.

Stress distribution in members under service conditions

Two additional beams, one of Type II with Ø34 mm rebar and one of Type III with Ø20 mm rebar, were tested to investigate flexural stiffness and stress distribution in the cross section under service conditions. They were instrumented with strain gauges on the rebars prior to casting. Multiple loading-unloading cycles were imposed to simulate structural response under service conditions, i.e. up to 50% of ultimate resistance (*S*).

Figure 4-9 and Figure 4-11 present measured strain variation in the rebar during the test. Scatter in measured values comes probably from the variation of UHPFRC properties in the member. Similar variation was observed by other authors[72,111,112].

The results of member modelling are presented in Table 4-6 and Table 4-7. The structural response of the beam is calculated using the material properties obtained from plates with the two methods of analytical inverse analysis, and with the inverse FEM analysis of beams. Good agreement of modelled to measured reinforcement bar strains are obtained, validating the method. Since the beams used for validation are not the ones used for obtaining the material properties, it is demonstrated that the method can be applied to structural members.

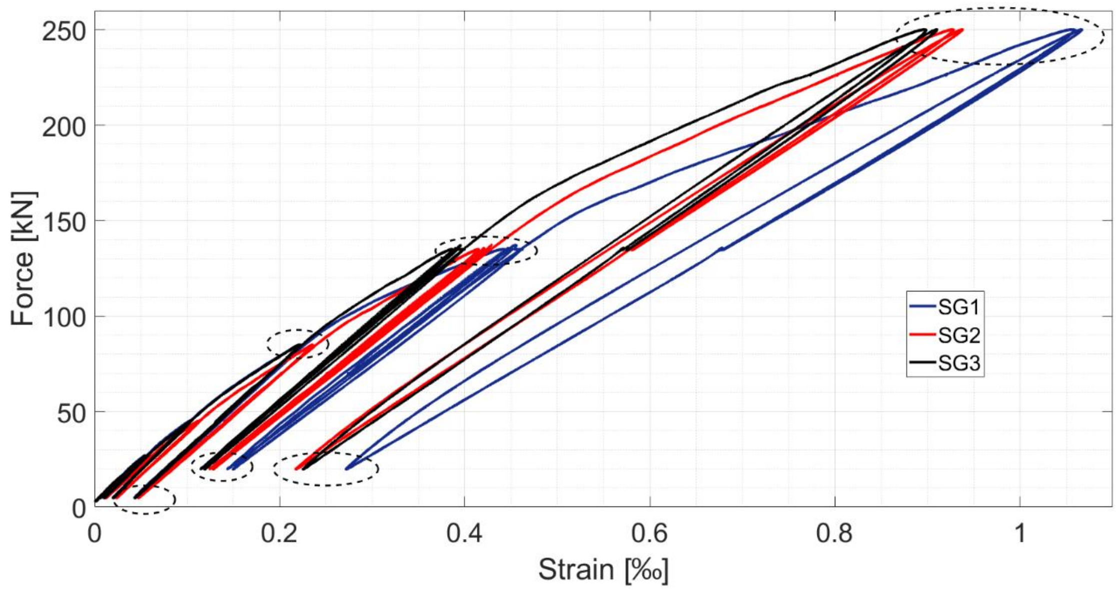

Figure 4-9. Force vs. strain in reinforcement, beam Type II (⌀34mm) for three strain gauges (SG) glued on rebar; modelled load steps marked with ellipses.

Table 4-6. Validation of stress distribution Type II (⌀34mm).

Force [kN]	*S* [-]	Strain modelled in rebar, UHPFRC properties from inverse analysis of [‰]			Strain measured in rebar [‰]	*Q* [-]	*R* [-]
		Beams	Method I	Method II			
85	0.17	0.25	0.30	0.27	0.22-0.23	0.63:1	0.91
5	0.01	0.02	0.09	0.06	0.04	0.73:1	1.00
135	0.26	0.45	0.57	0.52	0.39-0.44	0.79:1	0.0.81
20	0.04	0.12	0.26	0.19	0.12-0.14	1.25:1	0.98
250	0.49	1.03	1.24	1.12	0.89-1.05	1.28:1	0.75
20	0.04	0.32	0.56	0.37	0.22-0.27	2.10:1	0.97

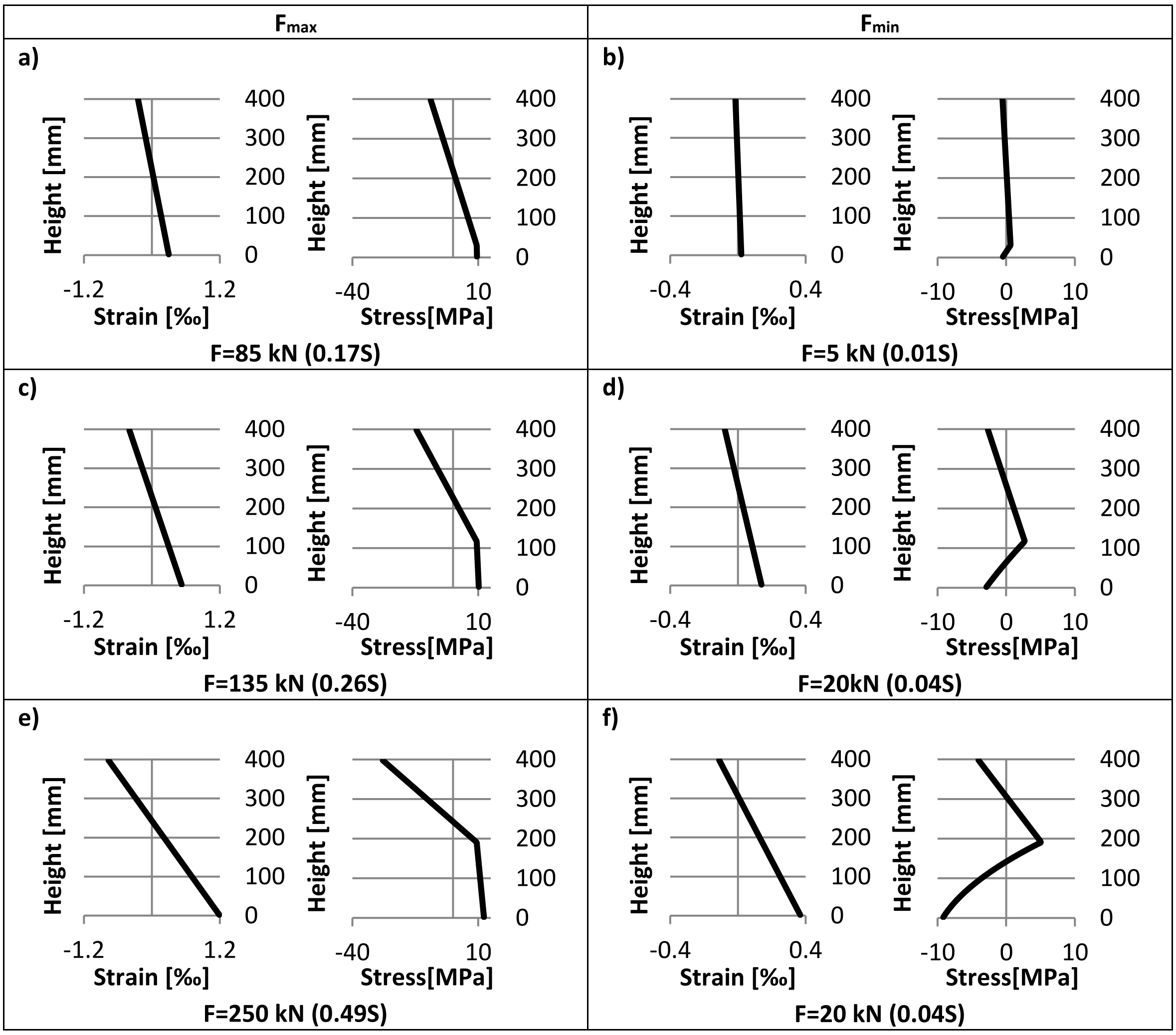

Figure 4-10. Stress and strain distribution in UHPFRC during loading (Fmax) and unloading (Fmin), beam Type II (⌀34 mm).

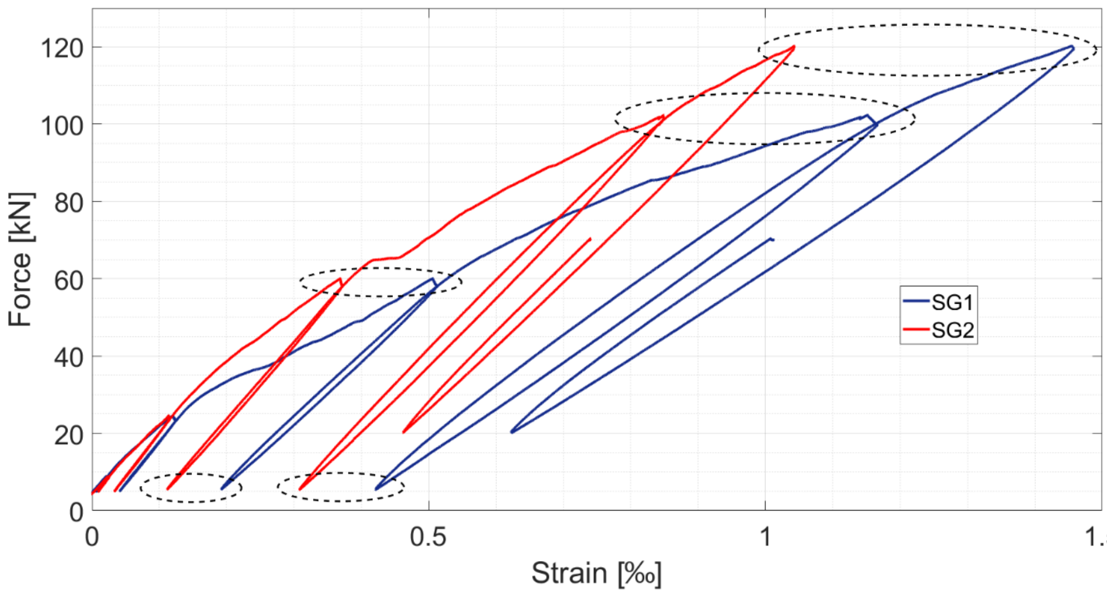

Figure 4-11. Force vs. strain in reinforcement, beam Type III (⌀20mm) for two strain gauges (SG) glued on rebar; modelled load steps marked with ellipses.

Table 4-7. Validation of stress distribution Type III (⌀20mm).

Force [kN]	*S* [-]	Strain modelled in rebar, UHPFRC properties from inverse analysis of [‰]			Strain measured in rebar [‰]	*Q* [-]	*R* [-]
		Beams	Method I	Method II			
60	0.26	0.42	0.37	0.28	0.36-0.50	0.57:1	0.59
5	0.02	0.12	0.14	0.04	0.11-0.19	0.90:1	0.84
102	0.45	0.90	0.82	0.65	0.84-1.14	0.98:1	0.53
5	0.02	0.39	0.39	0.20	0.31-0.42	1.56:1	0.84
120	0.53	1.13	1.03	0.84	1.04-1.45	1.16:1	0.53
20	0.09	0.57	0.56	0.36	0.46-0.62	2.18:1	0.82

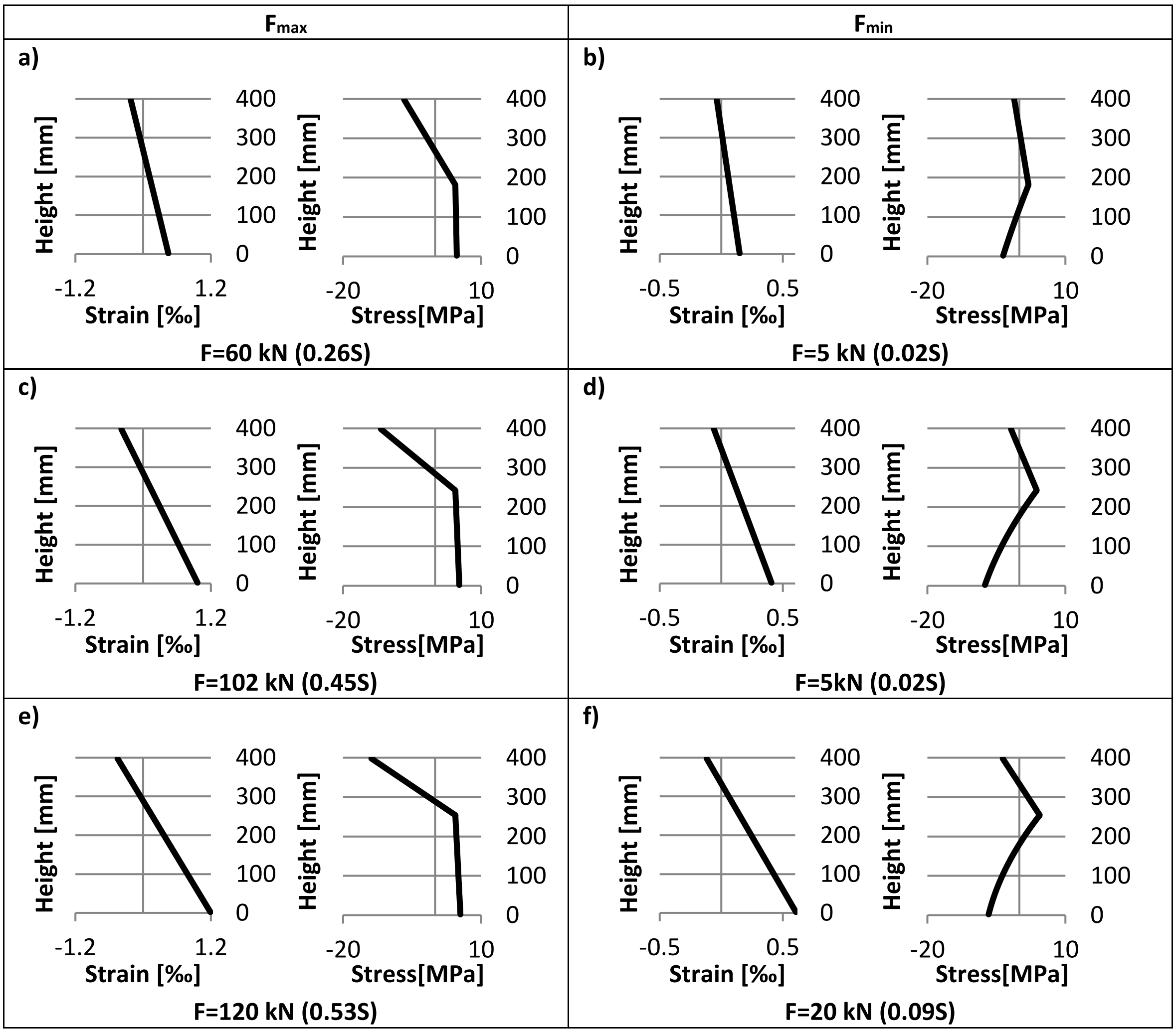

Figure 4-12. Stress and strain distribution in UHPFRC during loading (Fmax) and unloading (F¬min), beam Type III (⌀20 mm).

The ratio *Q* of tensile sectional force carried by reinforcement bar and UHPFRC respectively describes the level of cooperation between them. As stress increases and UHPFRC enters the strain-hardening domain, the load bearing contribution of the rebar is increasing. After unloading at F_{min}, the rebar contribution is more pronounced than during loading to F_{max} due to difference in loading (E_U, E_{Uh}) and unloading (E_{Ui}) secant values of the UHPFRC. The variation of the ratio *Q* comes from modification of cross-sectional properties due to the strain hardening and unloading constitutive laws of UHPFRC. This mechanism greatly reduces the stress variation in the rebar during loading-unloading cycles, which is in particular important in the case of fatigue.

Loss of member stiffness is quantified with the *R*-ratio of bending inertia of the cross-section showing UHPFRC strain-hardening to initial elastic inertia. The moment of inertia is calculated separately for F_{max} and F_{min} in each cycle. For F_{max}, a composite cross-section with three moduli of elasticity is assumed[74]: 1) UHPFRC in the elastic state with E_U, 2) UHPFRC in the strain-hardening state with E_{Uh} and 3) the reinforcement bar with E_s. The moment of inertia is calculated with respect to the neutral axis position x_{n-n} at F_{max}. For calculation of member inertia at unloading, the secant E_{Ui} is calculated for each computational layer separately. Then, the inertia of the composite cross-section about x_{n-n} at F_{max} is obtained. The inertia at F_{min} is higher than at F_{max}, which is reflected by the slopes of the curves shown in Figure 4-9 and Figure 4-11.

The distribution of strain and stress in UHPFRC for each load step is presented in Figure 4-10 and Figure 4-12. The response at F_{min} depends on the stress distribution at F_{max}. Interestingly, the UHPFRC in the bottom part of the member, which usually is in tension, may even show higher compressive stresses than the upper part when the beam is unloaded, depending on geometrical dimensions and loading history. In the case of the presented T-shaped beams it was up to 90% of total compressive sectional force (Figure 4-10 f)). Similar behavior, but with smaller compressive stress activated because of a different cementitious material used, was observed by Wang et al.[71]. With increasing load, the neutral axis position moves up due to strain-hardening and increase of *Q*. At unloading the axis goes even higher, compared to the respective F_{max}, due to the UHPFRC response and especially when compressive stress is activated.

The abovementioned mechanism determines the structural response and should be taken into account when calculating the stress state of the member under service condition. During loading, the range of elastic limit stress f_{Ute} in the cross-section should be found and modified composite section taken into account for stress calculations. When the structure is unloaded, a more complex method should be applied, with calculation of E_{Ui}. However, as stiffness during unloading is higher than at primary loading, neglecting the modified moment of inertia at unloading is acceptable for the sake of simplification leading to higher computed deflection range, thus conservative solution. Nevertheless, modified inertia at unloading should be taken into account during monitoring of deflection of R-UHPFRC structures under service loading as well as calculation of stress ranges under fatigue actions.

The method is validated for both beam types and good agreement was obtained between both measured and calculated strain using material properties obtained from inverse analysis of beams. The agreement with properties based on plate testing is lower, with average error of 20%. It is not obvious which method of inverse analysis of plates gives better results for the beam at service state.

Conclusions

This chapter presents and analyses test results of R-UHPFRC members and UHPFRC plates subjected to four-point bending. Analytical and finite element modelling inverse analysis methods are applied to retrieve UHPFRC material properties alongside with results using a magnetic non-destructive testing method. The results are compared and the importance of their variation quantified for R-UHPFRC beam behavior under loading-unloading and at ultimate resistance.

This research has shown that:

- The inverse analysis method can be used also for large elements, like full-scale beams, including elements with reinforcement bars.
- UHPFRC in tensile zone of the R-UHPFRC member enters into compression if it was previously loaded beyond the elastic limit. This phenomenon leads to significantly increased tensile strain in the rebar at the unloaded state and thus influences the global response of the structural member. This increase is largely notable in particular at high loading level.
- Magnetic NDT is a reliable method allowing to determine the UHPFRC tensile strength f_{Utu} after calibration for a given UHPFRC mix. Better estimation of ultimate bending resistance of structural members is obtained than based on material testing because fiber distribution in the element is explicitly taken into account.
- Combination of material testing on smaller specimens and magnetic NDT is recommended to retrieve the full set of material properties. This method gives results comparable to UHPFRC characterization with inverse analysis of prototype element.

Furthermore, the knowledge gap on behavior of UHPFRC in tension-compression regime was identified. It is recommended to investigate this research topic, which in turn would allow improving the quality of modeling of R-UHPFRC members under loading-unloading in the serviceability domain.

Chapter 5 Deformational behaviour and damage mechanism of a R-UHPFRC beam subjected to fatigue loading

On process of fatigue and failure mechanism of the R-UHPFRC beam instrumented with distributed fibre optics sensors

The content of this chapter was submitted for publication as:

Sawicki, B., Brühwiler, E., Bassil A. Deformational behavior and damage mechanism of R-UHPFRC beam subjected to fatigue loading. *Materials and Structures*, submitted on 12.10.2020.

Bartłomiej Sawicki was responsible for conceptualization, preparation and execution of experiments including casting of specimens; data collection (except of distributed fibre optics sensors), curation and analysis; conceptualization and preparation of the first draft; edition of the paper.

Novel building materials with high strength allow for design of more slender structures. Consequently, the ratio of external load, e.g. due to traffic, to self-weight is much higher than in the case of massive structures. Because of that, the fatigue resistance becomes of importance. One of such novel materials is the UHPFRC, comprising cementitious matrix with small constituents (<1 mm) and high amount of short fibers (>3% vol.), usually made of steel. It is often used with longitudinal reinforcement bars in the direction of highest internal forces, forming reinforced UHPFRC (R-UHPFRC).

So far, few fatigue tests on R-UHPFRC elements were reported. A test on a one-meter-long section of pedestrian bridge with GFRP rebars was executed by Parsekian et al.[113], with deflection measurement. Under load cycle ranges reaching up to 55% of static resistance, the structural stiffness degraded rapidly in the beginning and slower towards the end of the test, with stabilization at around 2/3 of the original value. After three million cycles no failure occurred. Makita and Brühwiler[114] performed direct tensile tests on R-UHPFRC plates with three longitudinal rebars. The specimens were instrumented with extensometers. Under a stress range similar to the present study, the deformation was growing only in the beginning of the test, up to 500'000 cycles, remaining later almost constant until rebar failure. This finding was explained by stress transfer from UHPFRC to the reinforcement bar as the former loses stiffness due to the fatigue process. The decrease of local deformation range was observed for critical cross-section until failure of the rebar; however, it was not discussed in detail. The variation of deformation range along the specimen was attributed to scatter of bulk properties of UHPFRC in the specimen. Moreover, they reported about spalling of the cementitious matrix during the fatigue process. The same authors[115] tested also reinforced concrete slab-like elements strengthened with R-UHPFRC layer. Similarly, variation of deformation was observed, with highest deformation range in the section where the critical crack occurred. They inferred that strain and stress in rebars grew gradually leading to failure and determining the fatigue resistance of the structural element. However, the strain range in reinforcement bars was not directly measured.

For the sake of simplicity in design and modelling, the UHPFRC material is assumed to behave like a continuum up to the tensile strength f_{Utu} - when the localized fictitious crack is formed. However, after reaching the elastic limit stress f_{Ute}, distributed matrix discontinuities, i.e. microcracks, appear. Observation of their opening may give important information on the fatigue process. Parsekian et al.[113] observed the largest microcrack opening amplitude. No change occurred under fatigue load range of 36% of static resistance, while rapid increase was observed under range equal to 55% of resistance. For the sake of comparison with the current research, a test on reinforced ECC (Engineering Cementitious Composite) with PVA fibers is analyzed[116]. The structure of the matrix and microcracking behavior of this class of materials is similar to UHPFRC[117]. The distributed microcracks formed at early stage and their depth across the beam stabilized after few thousand cycles. Slow and constant growth of their opening continued throughout the test. The tensile strain in reinforcement bars and global deflection were almost constant, and the rupture of rebars marked the failure of the beam.

Although Distributed Fiber Optic sensors (DFOs) were used for in-situ monitoring[118], measurement of strain in reinforcement[119] and discontinuities detection[112,119] in R-UHPFRC elements, they were never applied in fatigue experimental testing of UHPFRC. However, DFOs proved their usefulness for fatigue monitoring of strain[120] and crack opening[121] in reinforced concrete. They allow for detection and measurement of microcrack opening in UHPFRC as well[122].

This chapter discusses a fatigue test on a single R-UHPFRC beam, with strain measurement using extensometers (EXT), strain gauges (SG) and DFOs installed on reinforcement bars and UHPFRC. Special consideration is given to the cooperation of reinforcement and UHPFRC under tensile stress due to bending. Microcrack propagation and critical crack location are discussed. Finally, possible fatigue mechanism of UHPFRC in the structural member is presented.

As only one test is discussed, no conclusion on constant amplitude fatigue strength can be drawn. The chapter does not discuss fatigue damage rate dependence on loading levels because of the same reason. It is assumed that the overall mechanism remains the same under all fatigue loading levels that lead to fatigue damage accumulation.

Materials and methods

The full-scale R-UHPFRC T-shaped beam was tested under four-point bending (Figure 5-1). The beam was reinforced with one Ø34 mm steel reinforcement bar of class B500B according to Swiss and European standards[42,43], anchored with 90° hooks over supports and with UHPFRC cover c_{nom} = 17 mm, thus Ø/2. A steel I-beam of high rigidity distributed the load applied with a single hydraulic actuator. The load application points were placed at 100 mm from mid-span of the tested beam, symmetrically. A hinge and a force transducer were located between the actuator and the distribution beam.

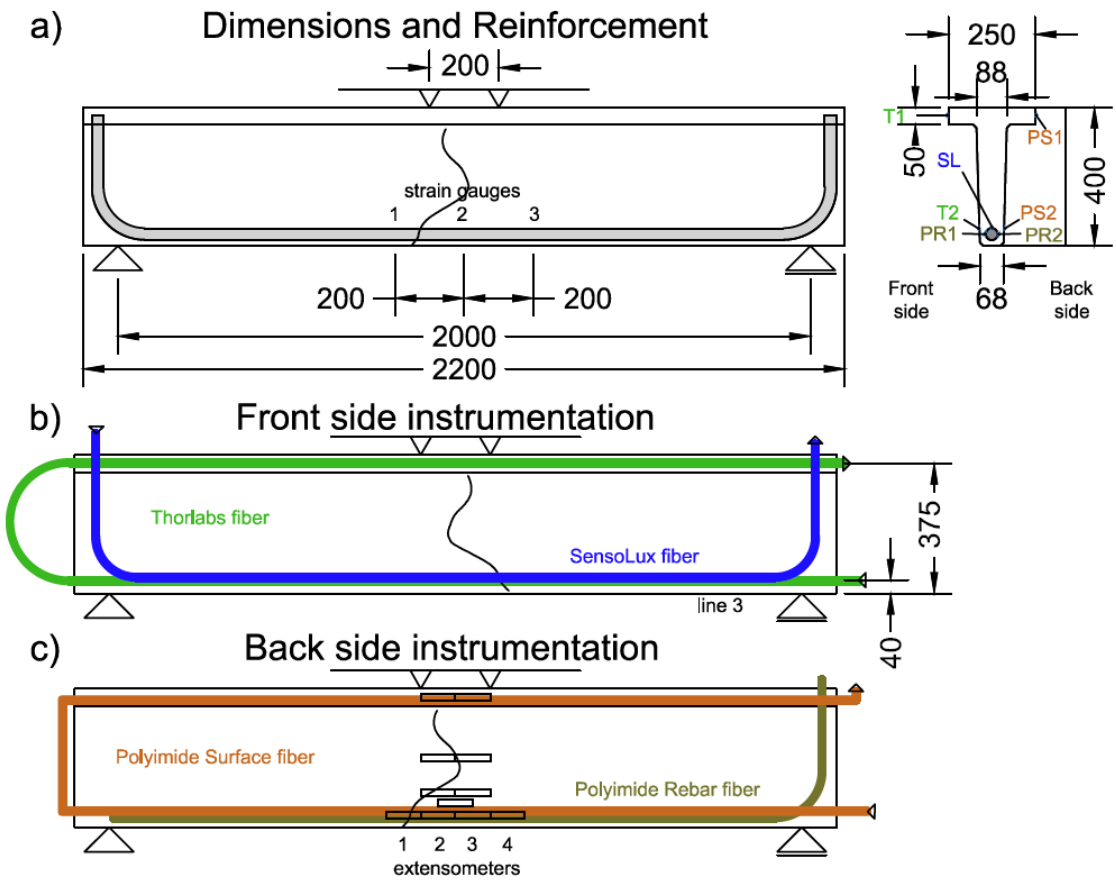

Figure 5-1. Instrumentation of the beam with location of the critical crack; DFOs types: PS – Polyimide coating fiber on surface, PR – Polyimide coating fiber on reinforcement bar, T – Thorlabs fiber, SL – SensoLux fiber.

The beam was casted with commercially available premix Holcim710® with 3.8% vol. 13 mm straight steel fibers of aspect ratio 65. The following properties were obtained from material testing according to Swiss standard[20]: elastic limit stress f_{Ute} = 5.5MPa, tensile strength f_{Utu}=11.8 MPa, modulus of elasticity E_{Ut} = 40.6 GPa, hardening strain at tensile strength ε_{Utu} = 3.5‰ and compressive strength f_{Uc} = 140 MPa. The beam for fatigue testing was casted together with an identical reference beam to obtain the resistance under quasi-static loading.

The fatigue test was preceded with quasi-static displacement-controlled pre-loading. The load was gradually increased with loading-unloading cycles until the target constant fatigue force range was obtained, with F_{min} = 20 kN and F_{max} = 250 kN. They represent respectively 4% and 53% of static resistance (S) of the reference beam. Then, the system was switched to the force-controlled mode and the fatigue test started, with a frequency of 4.2 Hz. To conduct measurements with fiber optics, the test was stopped periodically and a slow fatigue cycle (0.025Hz) executed. The DFOs measurements were performed during the 1st and 2nd cycles, then around every 10^3 cycles until 10^4 cycles (10 measurements), every 10^4 cycles until 10^5 cycles (10 measurements), every $5 \cdot 10^4$ cycles until $7 \cdot 10^5$ and finally every $1 \cdot 10^5$ cycles until failure. The test lasted for $8.76 \cdot 10^5$ cycles until failure of the beam.

The beam was instrumented with strain gauges, extensometers and fiber optics (FO) for distributed sensing (Figure 5-1). The foil strain gauges were glued at the top of the reinforcement bar before casting, at mid-span and symmetrically 200 mm from mid-span. The extensometers with measurement base of 100 mm were glued to the surface of the beam according to Figure 5-1 c). Three types of DFOs were used in this research. The Luna® High-Definition Polyimide coating fiber of diameter Ø155 µm was glued to the flat surface of longitudinal rib from both sides of rebar before casting. Same type of fiber, as well as the SMF-28 Thorlabs® Ø900 µm fiber with elastomer tubing, were glued to the surface of UHPFRC in a previously prepared groove, as described in detail in Sawicki et al.[122]. The SensoLux cable Ø2000 µm was directly embedded in UHPFRC during casting. This fiber was chosen for its mechanical resistance and was placed next to the reinforcement bar. Detailed information on all types of fibers can be found in Bassil et al.[123].

The DFOs can be used for detection and measurement of discontinuities in the cementitious matrix, i.e. microcracks. The detection is based on observation of a strain peak signatures measured at the level of the optical fiber. Part of the optical cable which spans the discontinuity is stretched. However, due to a strain lag between the optical fiber core and its surrounding layers, measured strains form an exponential peak over a certain fiber length. The width of the peak depends on the structure of the fiber optics cable and glue. It is quantified with the strain lag parameter λ [m^{-1}] determining the capacity of the fiber to measure microcracks at a certain range of crack openings[123]. The opening of discontinuity, traditionally called Crack Opening Displacement (COD), is measured by fitting the model to exponential peaks. The mechanical strain transfer equation between the UHPFRC and the core of fiber is used:

Equation 5-1

$$\varepsilon_f(z) = \sum_{i=1}^{21} \frac{\mathrm{COD}_i}{2} \lambda e^{-\lambda|z-z_i|} + \varepsilon_m(z)$$

where COD_i is the opening displacement of each discontinuity i, parameter λ is the fitted strain-lag parameter, z_i corresponds to the position of each apparent strain peak, ε_f is the apparent strain measured with DFOs, and ε_m is the strain of host material. In this work, ε_m was obtained using strain gauge measurements. The exponential equation is fitted to the most important apparent strain peaks using least square method. In this work, 21 microcracks were observed. This measurement method was developed and described in detail elsewhere[123] and demonstrated for UHPFRC by Sawicki et al.[122]. For the sake of brevity, the theoretical background is not presented here.

Deflection and strain evolution

Figure 5-2 presents the beam deflection ($\Delta\delta$) and strain ($\Delta\varepsilon$) ranges recorded with extensometers and strain gauges during the entire fatigue test. The strain range measured with strain gauges is smaller than the one measured with extensometers. This may come from the fact that strain gauges were installed at the top of the rebar while extensometers at level of axis of the rebar, thus 17 mm lower. The drops of values measured by all sensors indicate moments when the test was stopped to perform slow cycles and FO measurements.

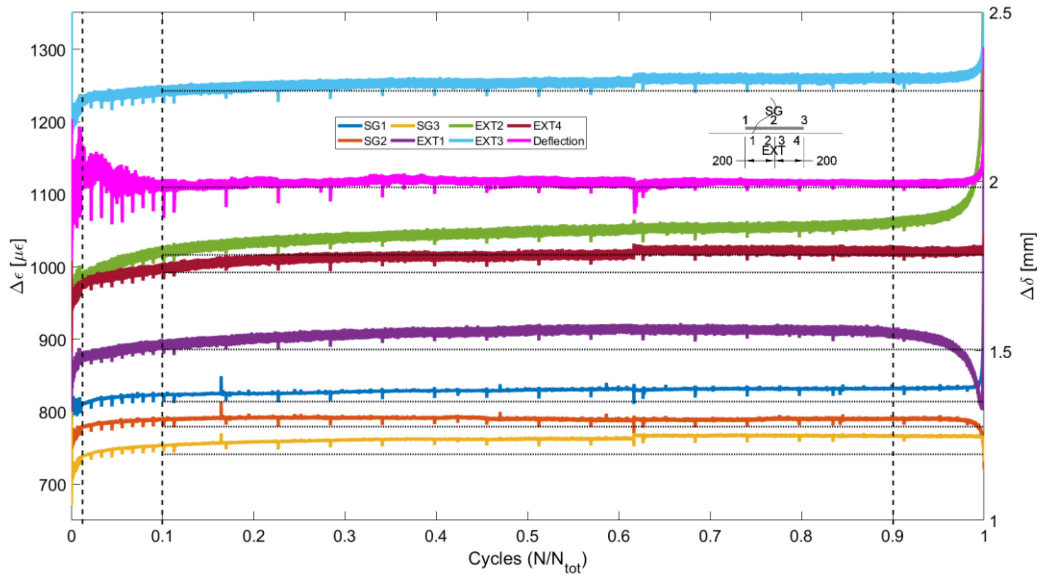

Figure 5-2. Strain and deflection ranges during the whole duration of the fatigue test.

In the first 1% of test duration, a rapid rise of strains and deflection ranges occurs. The simultaneous rise of values recorded by all sensors indicate that a volumetric phenomenon takes place, which can be associated with distributed microcracking. Before 10% of test duration is reached, strain and deflection ranges stabilize marking the end of stage I. It can be determined through observation of derivations of the recorded curves reaching zero. At 90% of test duration, a gradual rise of strain range, as well as of its derivation, in EXT2 and simultaneous fall in the neighboring EXT1 are observed, indicating the beginning of stage III. This is caused by the perturbation due to fatigue damage in that region, and possibly localized fictitious crack initiation within range of EXT2. The graph of derivations is not presented in this chapter for the sake of brevity. Evolution of strain range variation can be observed in Figure 5-2.

Figure 5-3 shows magnification of the last 10% of the fatigue test. At 95%, the fatigue process in the region of EXT1 and EXT2 accelerates. During the last percent of the test, strain range in SG1 starts to increase indicating stress transfer between UHPFRC and rebar, and possibly an onset of crack propagation in the reinforcement bar. In the last 2‰ of test duration, the strain range of SG1 starts to increase rapidly as well as strain range of EXT1. This indicates the formation of a localized fictitious crack in UHPFRC due to interaction with the rebar. At this point, the global deflection range starts to increase as well. SG2 and SG3 show a decrease of strains while EXT1 to EXT3 reveal continuous rise of strain values. This could indicate a change of the static system due to fictitious crack propagation. However, EXT4 remains within its range of strains, showing that no global modification of stress-field occurred. Therefore, the rise of strain in UHPFRC and reduction in the rebar most probably indicate unloading of the rebar.

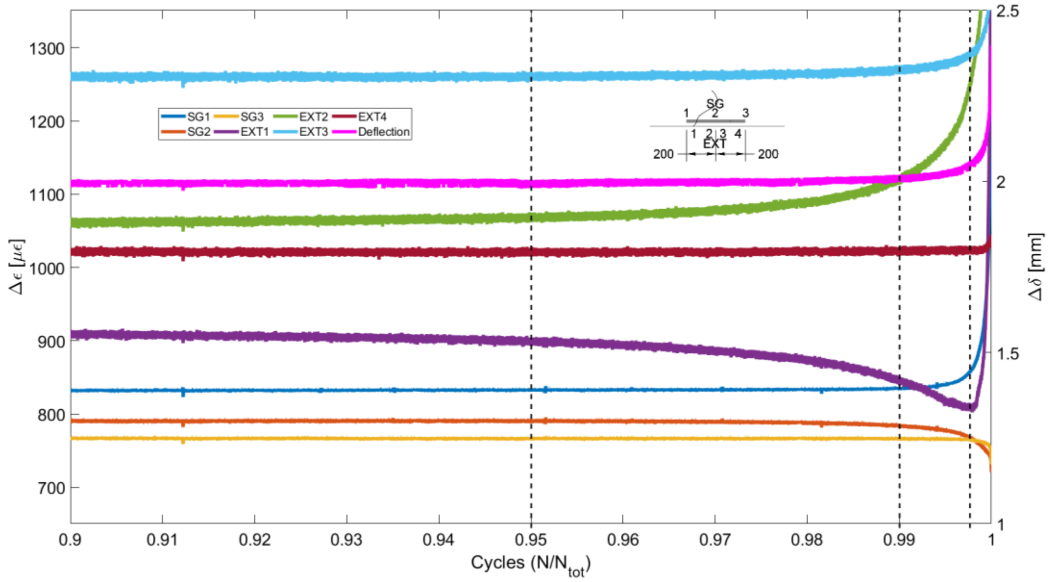

Figure 5-3. Strain and deflection ranges during the last 10% of fatigue test.

At this moment, the fatigue crack in the rebar has well propagated, and part of the force previously carried by the rebar is transmitted to the surrounding UHPFRC. According to tests by Oesterlee[89], the peak bond stress of B500B rebar and UHPFRC is $\tau = 44$ MPa, for a mix containing 3% volume of fibers, with f_{Uc}= 198.3 MPa and f_{Utu} = 10.8 MPa. The peak bond stress is slightly rising with increasing fiber content. Tests were done with Ø8 mm rebars using a specimen cross section of 50 mm x 50 mm, thus c_{nom} = 2.6Ø. As shown by Yuan and Graybeal[124], τ decreases with decrease of cover and increase of rebar diameter. For UHPFRC with 2% vol. of fibers and compressive strength after 14 days f_{Uc} = 145 MPa, the average maximum bond strength was 23 MPa and 20 MPa for rebars Ø16 mm and Ø22 mm respectively, with c_{nom} = 2.0Ø. However, for the mix with 2% vol. of fibers, f_{Utu}=11.5 MPa and f_{Uc} = 201.8 MPa, with c_{nom} =1Ø, τ = 73.25 MPa and 71.01 MPa for Ø13 mm and Ø16 mm rebars respectively were obtained[125]. Lagier et al.[126] obtained τ = 10.5 MPa for rebar Ø =25 mm, mix with 4 % vol. of fibers, f_{Uc}= 110 MPa and f_{Utu} = 12 MPa for splice joints with cover c_{nom} = Ø/2. Importantly, they tested direct rebar contact splices where the area of rebar surrounded by UHP-FRC is reduced; this was not taken into account in the calculation of bond stress.

With SG1 ε_{max} = 1200 με at F_{max}, the stress in rebar is σ_{max} = 246 MPa with E_s = 205 GPa. As the fatigue crack in the reinforcement bar is located in the middle of EXT1, the length of the zone affected by the discussed phenomenon is around 150 mm, barely reaching EXT3. Assuming complete loss of bearing capacity of reinforcement in the last stage, calculated average bond stress to transfer the total force carried by rebar to UHPFRC at this segment is τ =14.0 MPa. Taking into account small cover, large rebar diameter, and small slip of reinforcement, thus not full activation of the bond strength, the obtained value seems plausible. Therefore, it can be deduced that 2‰, i.e. around 1700 cycles, before the end of test the reinforcement bar carries almost no force since the fatigue crack has largely propagated. The stress is therefore transmitted to UHPFRC causing its fast deterioration around the crack, localizing the failure section and leading to the collapse of the beam. Importantly, the reinforcement bar ruptures completely only at the very end of the test, which is confirmed by noise. This is in accordance with observations of Makita and Brühwiler[114].

Figure 5-4 shows maximum and minimum strain in each cycle measured by four extensometers during the last 10% of the test. Slight rise of strains of EXT2 at both F_{max} and F_{min}, as well as decrease of strain of EXT1 under F_{max}, in the last 5% of the test confirm the previous observations of fatigue damage accumulation in

UHPFRC and thus loss of stiffness. During the last 2‰ of test duration, both maximum and minimum strains at EXT1 and EXT2 rise as the stress is transmitted from the rebar to the UHPFRC. The quick pace of this stress transfer indicates a high rate of fatigue crack propagation in the rebar. This is in agreement with observations of Rocha et al.[127]. Thus, the onset phase of fatigue damage of reinforcement bar takes the majority of test duration. However, once the fatigue crack is initiated, it propagates quickly up to rupture.

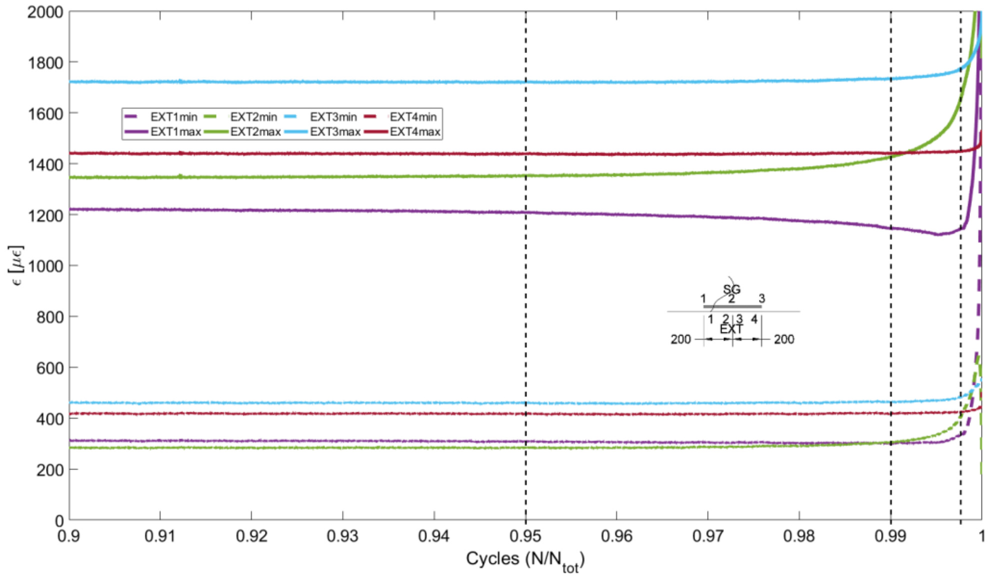

Figure 5-4. Minimum and maximum strain in a cycle measured by extensometers during the last 10% of fatigue test.

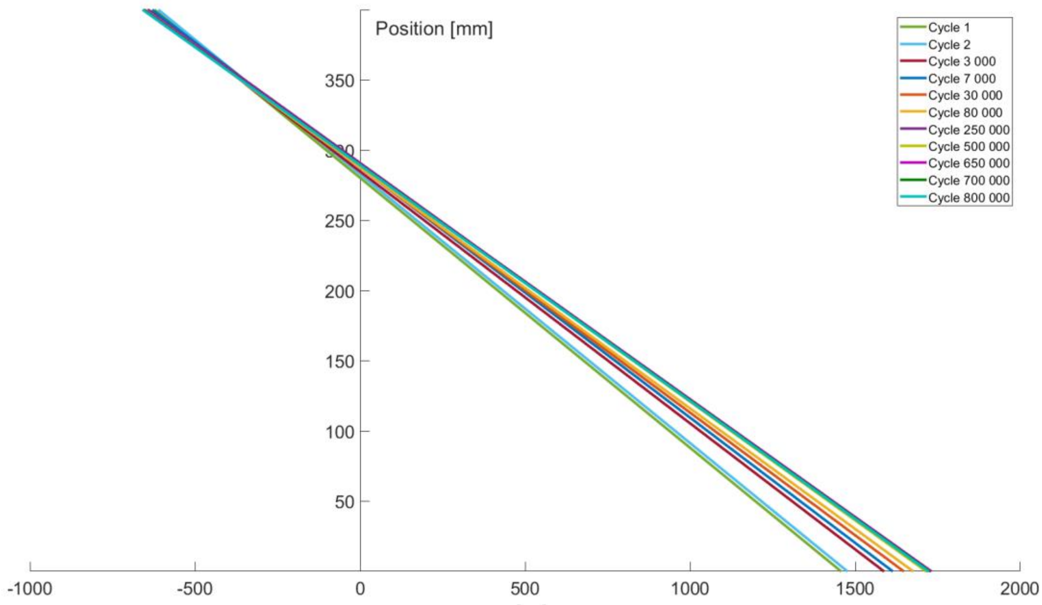

Figure 5-5. Strain slopes in constant bending moment zone of the beam during fatigue test under F_{max}.

Figure 5-5 shows the strain profiles at F_{max} as obtained by interpolation of extensometer measurements along the height of the beam (see Figure 5-1) until 90% of test. Slight increase, of almost 20%, of strain values in the tensile zone can be noticed. Overall, the strain distribution remains stable in test stages I and II.

The strain profile at F_{min}, presented in Figure 5-6, shows much more variation. Cycle 0 indicates the moment when 20kN force is reached for the first time. At the end of cycle 1, when F_{min} is attained again, the strains are much higher. This is an effect of the part of UHPFRC entering into strain-hardening under F_{max}. This loading-unloading behavior is discussed in detail in Chapter 4. After cycle 2, strains are further increasing along the whole cross-section, keeping the slope (curvature) constant. Towards the end of the test, gradual gain of strain can be noticed, with rise of the neutral axis position. Seemingly, the response of the beam under F_{min} is a much better indicator of the fatigue process than F_{max}, which is discussed later.

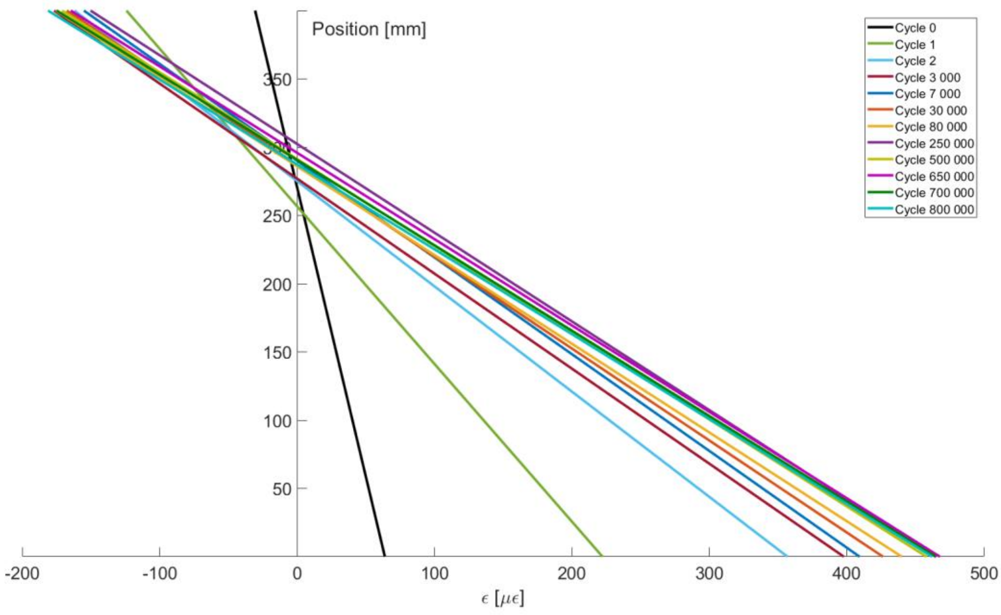

Figure 5-6. Strain slopes in the constant bending moment zone of the beam during fatigue cycles under F_{min}.

Strain distribution in the beam

The strain measured with distributed fiber optics sensors, strain gauges and extensometers while reaching F_{min} = 20 kN for the first time is presented in Figure 5-7. No peaks of strain are present in DFOs results as the cementitious matrix remains homogeneous and UHPFRC is in the elastic regime. EXT1 and EXT4 show lower strain than EXT2 and EXT3, since they lie outside of the constant bending moment zone. Strain gauges show lower strain than DFOs on rebars as they are positioned 17 mm higher, thus closer to the neutral beam axis.

Still in the first loading cycle, and under force of 45 kN, UHPFRC enters into the strain-hardening domain where distributed microcracks are formed (Figure 5-8). They are detected by regular strain peaks of external polyimide fiber measurements, with average spacing of 17 mm. Few microcracks grow at higher rate and are visible along the T2 fiber line as well. They start propagating from the surface of the beam as the polyimide fiber lines PR1 and PR2, as well as SensoLux (SL) cable keep measuring uniform strains. It is important to mention that the SensoLux cable is the least sensitive to microcracks among the chosen FO cables, as it is characterized by low value of the strain lag parameter λ [123]. The variation of strain measured with extensometers provoked by microcracking is clearly visible and in accordance with previous research[72,111,112,122]. While EXT1, 2 and 4 show good agreement with T2 fiber measurements, EXT3 shows higher strain. This extensive microcracking occurs on the surface, as it is not visible with Thorlabs fibers located on the other side of the beam.

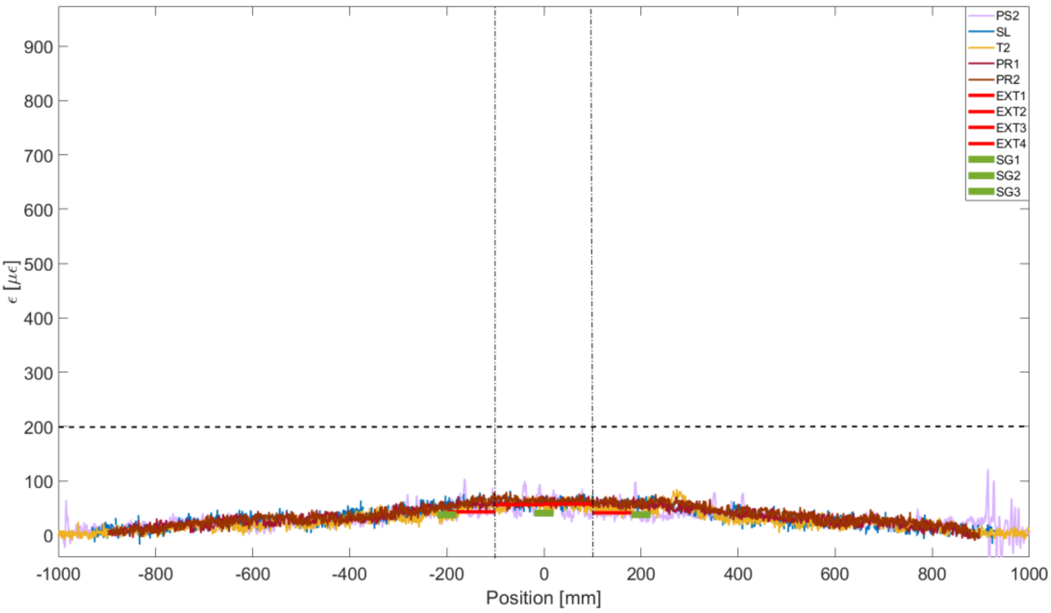

Figure 5-7. Spatial strain distribution in the beam, 1st time at force 20kN; constant bending moment zone marked with vertical dashed lines; acronyms as in Figure 5-1; 200με line for comparison.

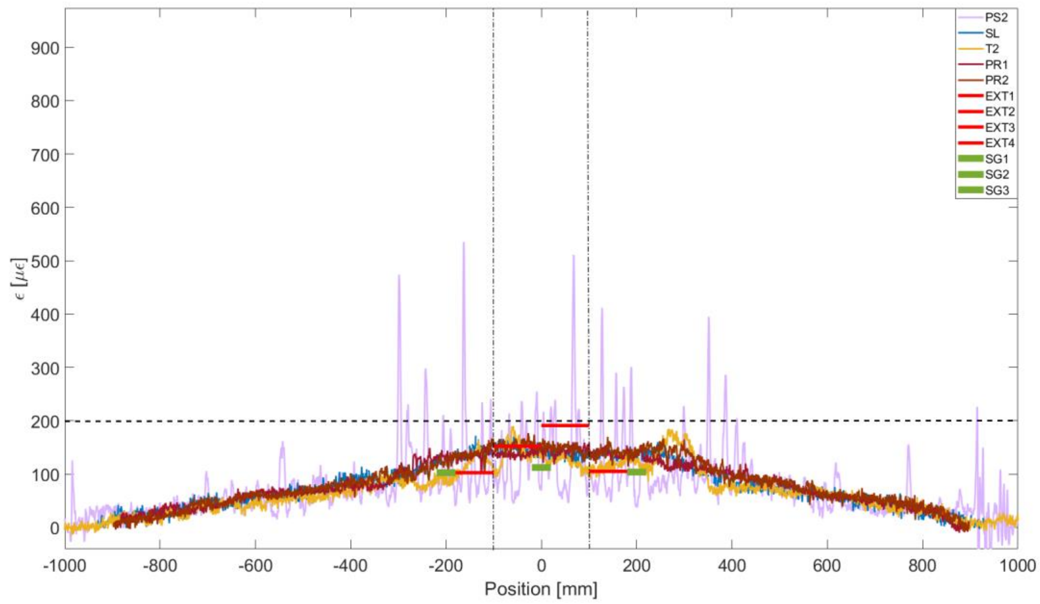

Figure 5-8. Spatial strain distribution in the beam at force 45kN; constant bending moment zone marked with dashed line; 200με line for comparison.

When maximum force F_{max}=250 kN is reached for the first time, multiple microcracks are clearly visible (Figure 5-9 , left). The most advanced one is located around position -50 mm, visible with T2, SL and PR1 lines. It is however not visible with PR2 fiber and EXT2 on the other side of the beam (Figure 5-1). This microcrack can be the reason behind fatigue damage accumulation within the range of EXT2 later on, as discussed previously. EXT3 keeps showing higher strain than the others. Since this microcracking front is not visible by any other sensor, it can be deduced that it does not reach the reinforcement bar and thus remains at the surface. Another large front is visible with Thorlabs fiber at 300 mm, but only slight increase of strain on one side of rebar can be noticed. As far as SG1 fiber glued to reinforcement measure similar strain, SG2 and SG3 are 20%

lower. Strain distribution in the reinforcement bar presents clear trapezoidal shape due to four-point bending. The strain distribution at F_{max} during the 2nd cycle is not different from the one during the 1st cycle (Figure 5-9).

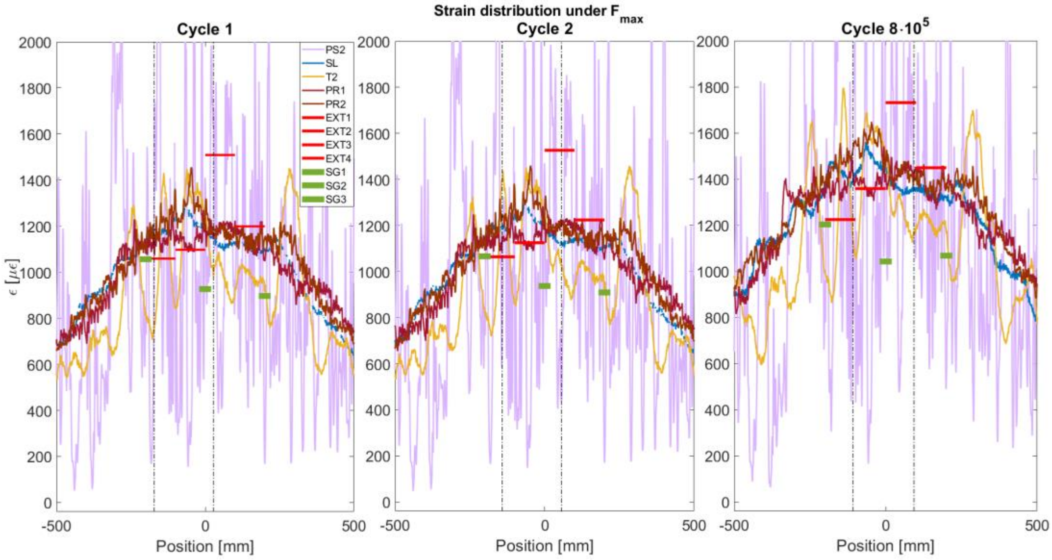

Figure 5-9. Spatial strain distribution in the beam at force 250kN (F_{max}) for 1st, 2nd and 800 000th cycle; constant bending moment zone marked with dashed lines.

The last DFO measurement was taken after $8 \cdot 10^5$ cycles, thus at 91% of the test. The overall rise in strain at F_{max} is around 20% compared to the first cycle (Figure 5-9). There is no distinct strain peak in the reinforcement bar, which indicates no advanced fracture process and continuity of reinforcement bars can be assumed at this stage.

At the end of the first full cycle, with F_{min} = 20 kN (Figure 5-10, left), the attained strains are much higher than during the first loading to this force (Figure 5-7). This is due to the fact that UHPFRC which entered the strain-hardening domain does not come back to its original state after unloading, and residual strain remains (see Chapter 4). As the microcracks close, the apparent strain peaks of Polyimide surface fiber remain in the same positions as under F_{max} (Figure 5-9), but are much narrower and isolated. The peaks shown by the Thorlabs fiber keep similar width, with smaller apparent strain value. All the sensors, except of EXT3, show good agreement. The trapezoidal shape of the reinforcement strain profile is not evident anymore. This is due to the progressive modification of cross-section towards the constant-bending moment zone, as the zone of UHPFRC which entered previously into strain-hardening, grows. The closer to the midspan, the more the effect of strain rise at unloading is pronounced, producing the concave shape of strain plot (Figure 5-11).

At the end of the 2nd cycle, further rise of strain values and convexity can be noticed. Strain in average is now about 66% higher than after the first cycle and 275% higher than at the first loading to F_{min}. The reinforcement strain peaks are much more evident at position -300 mm, -50 mm and 300 mm. The strain peaks are much better visible than after the 1st cycle, indicating that microcracks do not close completely after unloading.

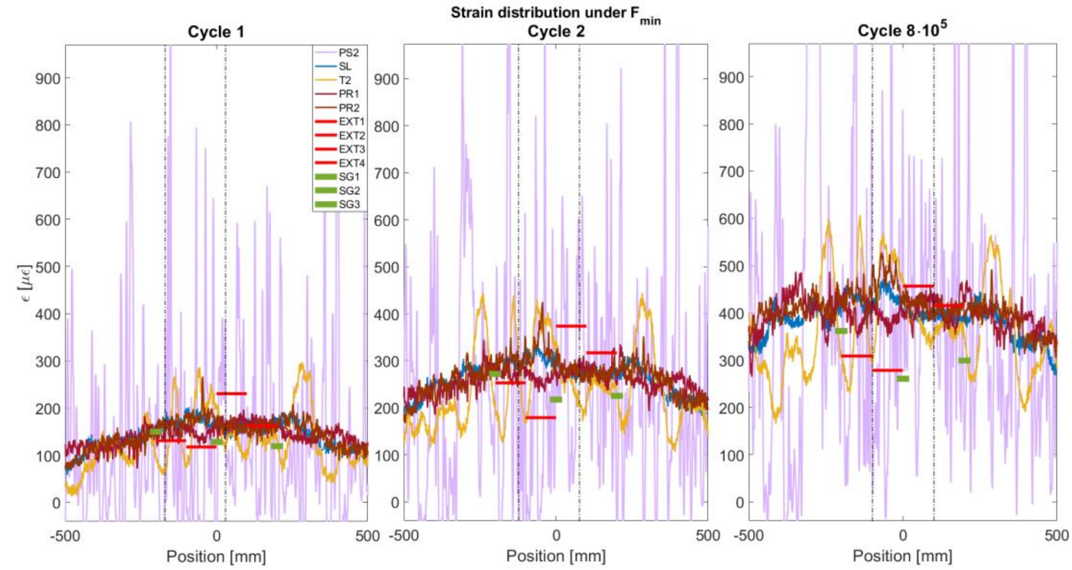

Figure 5-10. Spatial strain distribution in the beam at force 20kN (F_{min}) for 1st, 2nd and 800 000th cycle, constant bending moment zone marked with dashed line.

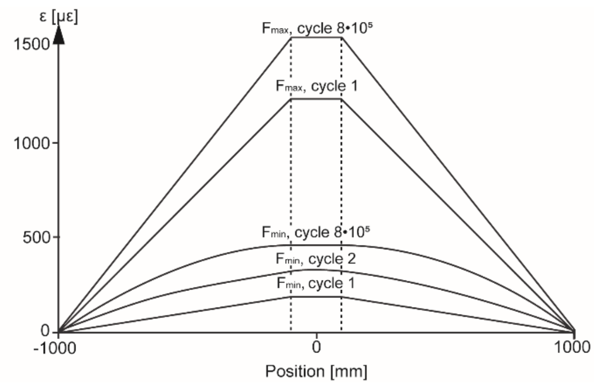

Figure 5-11. Outline of strain distribution in the reinforcement bar during fatigue test.

During unloading of the beam in the last DFO measured cycle, further increase of strain values (Figure 5-10) and concavity of strain profile (Figure 5-11) are noticed. However, the difference between $8\cdot10^5$ cycle and 2nd cycle is not as pronounced as between 2nd and 1st cycle. The strains in the constant bending moment zone measured with Polyimide fiber on the rebar, SensoLux fiber and strain gauges are around 50% higher compared to the 2nd cycle, 150% higher than after the 1st cycle and 460% compared to the 1st loading. Interestingly, the rise of strain is much less pronounced on the surface, where this rise is only about 20% compared to the 2nd cycle. Importantly, although the relative increase of strain at F_{min} is much more important than at F_{max}, the absolute values remain similar for the two loads. Therefore, the strain range during the fatigue stage II remains almost constant (Figure 5-2).

The last DFO measurement was taken after 91% of test duration, thus before rapid strain range evolution and fatigue stage III started. Therefore, it cannot be of help in analyzing this last, dynamic part of the process.

Matrix discontinuities opening displacement

The Thorlabs fiber was used for measurement of microcrack opening (COD), similarly to Sawicki et al. [122]. Figure 5-12 presents the COD evolution during the fatigue test under both F_{max} and F_{min}. The microcracks are formed in the very beginning, and their number remain constant during the whole test. The COD under F_{max}

reaches its maximum at around 500'000 cycles and is slightly reduced later, which supports observations of Makita and Brühwiler[114] regarding strain stabilization. The COD under F_{min} grows continuously throughout the test. Until the last measurement (91% of test duration) all the discontinuities remain in the microcracking domain (<50µm). This small evolution is the reason why the fatigue progress cannot be discerned through observation of microcrack propagation. At the same time, and considering that the maximum strain under F_{max} remains below 1500µε, it can be deduced[128,129] that UHPFRC under fatigue keeps its watertight performance at least for 90% of mechanical fatigue duration, i.e. strain remains smaller than 1.5‰. Importantly, even though the openings of these matrix discontinuities vary, their distribution along the beam is uniform.

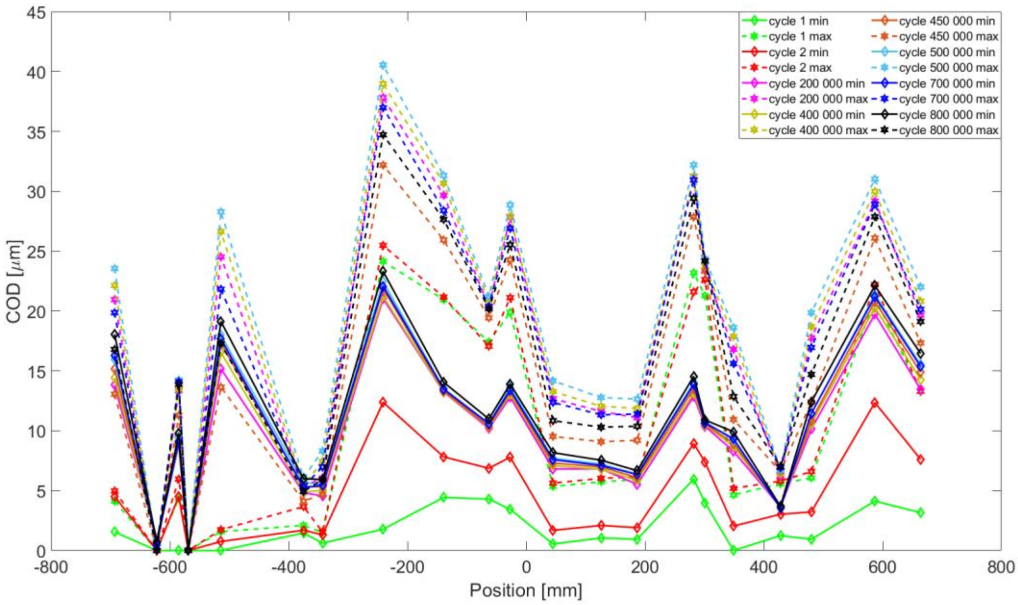

Figure 5-12. COD of microcracks along the beam length during the fatigue test.

Description of a likely fatigue damage mechanism

Due to loading-unloading cycles, part of the cross-section of the R-UHPFRC beam enters the strain-hardening phase at F_{max}, which leads to some plastic deformation. While unloaded to F_{min} the residual deformation is maintained, and compressive stress is activated in this zone (see Chapter 4). Figure 5-6 reveals slight decrease of negative strain in the top flange of the beam during the test, with continuous growth of tensile strain in the bottom portion of web and rebar under F_{min}. Consequently, assuming linear elastic steel behaviour and no reduction of reinforcement area, higher compressive stress has to be activated in the bottom part of the beam to fulfil the balance of forces in the cross section. One may suspect that this strain increase in the rebar could also be produced by a decrease of tensile bearing capacity in the UHPFRC. However, this would also affect stress distribution at F_{max}, when the tensile contribution of UHPFRC is even more important. As presented in Figure 5-5 , this is not the case and the strain profile at maximum force remains approximately constant.

The increase of compressive stress in the bottommost part of the beam may be due to spalled particles of the matrix. These specks interlock inside microcracks when they open up at F_{max} and do not allow them to close completely at F_{min}. Spalling and pulverization of matrix due to pull-out of non-axially aligned fibers during tensile fatigue tests were observed previosly[111], similarly as shown in Figure 5-13. The gradual increase in microcrack opening after unloading is observed in Figure 5-12, supporting this hypothesis regarding the effect of spalled particles on the deformational beam behavior at F_{min}.

Figure 5-13. Fatigue fracture surface of the bottom part of the beam.

As mentioned previously, at 90% of test duration, lower strain increase (of 20%) is recorded with external extensometers, compared to the 2nd fatigue cycle, than with internal DFOs (50%), thus SensoLux and Polyimide on the rebar. This indicates increasing transversal strain gradient in the beam, which again can be attributed to the accumulation of pulverized matrix particles in the microcracks. On the surface, the particles can be evacuated under F_{max} when the microcracks are opened. Indeed, during the whole test, there were flecks of cementitious matrix accumulating under the beam. However, powder particles entrapped inside the element cannot evacuate and the transversal strain gradient occurs. This is also confirmed by the smooth fatigue fracture surface of UHPFRC, as shown in Figure 5-13, mostly occurring in the middle of the web. There, the fibers are bent due to fretting as already described by Makita and Brühwiler[111].

Typical smooth surface of steel reinforcement bar due to the propagating fatigue crack is visible in Figure 5-13 as well. Small rough fracture area (around 15% of original rebar surface) indicates that reinforcement carries only little force at the moment of rupture. Assuming a rebar tensile strength f_u = 624 MPa as obtained from material testing, only 30% of the force carried in the first cycles (with σ_{max} = 246 MPa) can be transmitted by this reduced cross-section. This confirms the previously discussed stress transfer to UHPFRC during the last 2‰ of test duration.

Conclusions

This chapter discusses in detail the fatigue test on a reinforced UHPFRC beam. The T-shaped member was loaded in four-point bending, with a fatigue force range equal to 49% of static flexural beam resistance and resisting 0.88 million cycles before fracture. The beam was instrumented with external extensometers, strain gauges on rebar and distributed fiber optic sensors glued to rebars, embedded inside and mounted on the surface of UHPFRC. Analysis of test results allow to draw the following conclusions:

- The fatigue deformation behavior of R-UHPFRC beam shows three stages: Stage I (0% - 10% of total number of fatigue cycles) with rapid increase of strains; Stage II (10% - 90%) with stable behavior showing only little increase in strain, and Stage III (90% - 100%) with rapid increase of strain leading to fatigue failure.

- Fatigue failure of R-UHPFRC member is determined by the fatigue fracture of the steel reinforcement bar.

- Strain increase during Stages I and II is more important at minimum (F_{min}) rather than maximum (F_{max}) force in the fatigue cycle. This indicates that the fatigue damage of UHPFRC occurs under tensile-compressive stress reversal, possibly due to accumulation of pulverized, spalled particles of the cementitious matrix in microcracks.

- Fatigue damage occurs locally. During Stage III, local fatigue damage is visible in the strain range increase in the given section, but the reduction of stiffness is too small to influence the global member behavior, i.e. deflection.

- The fatigue damage process in UHPFRC and rebar does not necessarily take place in the same cross-section, but nearby i.e. in the range of around 100 mm. However, the advanced fatigue crack propagation causes loss of bearing capacity of the rebar just prior to failure, overloading locally UHPFRC, which leads to localizing the final rupture in the same cross-section. This process takes place during sub-stage IIIa in the last 2‰ of test duration.

- The deflection range increases only in the last Stage IIIa, when the reinforcement bar can no longer transmit the tensile force.

- Beyond Stage I, no new matrix discontinuities appear. During Stage II, the maximum opening of matrix discontinuities remains stable, while the minimum opening constantly increases. These openings remain below 50 µm, therefore continuity of UHPFRC can be assumed.

Chapter 6 Fatigue resistance of reinforced UHPFRC beams

On resistance and safe design of fatigue-sensitive R-UHPFRC elements

The content of this chapter was submitted for publication as:

Sawicki, B., Brühwiler, E. Fatigue resistance of reinforced UHPFRC beams *International Journal of Fatigue*, submitted on 18.10.2020.

Bartłomiej Sawicki was responsible for conceptualization, preparation and execution of experiments including casting of specimens; data collection, curation and analysis; conceptualization and preparation of the first draft; edition of the paper.

The reduction of CO_2 emissions, as well as energy and raw materials consumption, in the construction sector leads towards high-performance building materials, limiting their quantities necessary for erection of structures. This, in turn, increases the live-load to dead-load ratio, rising the importance of fatigue resistance. One of such materials is UHPFRC with rising use around the world.

Most of research related to the fatigue behavior of UHPFRC was concentrated on its compressive response, while it is the tensile response that is more relevant from the structural point of view[66,96,130–133]. Furthermore, the majority of fatigue tests were conducted on small specimens, whilst it can be expected that in reinforced UHPFRC (R-UHPFRC), i.e. steel reinforcement bars implemented in the UHPFRC, the capacity of stress redistribution in the structural element may be significant

This chapter reports on fatigue tests on T-shaped R-UHPFRC beams under four-point bending. The design of the specimen was inspired by the use of UHPFRC in structural applications as beams or unidirectional slabs[73,130]. Special attention is paid to the interaction of steel reinforcement bars and UHPFRC in the tensile stress region of the beam. The main goal was to explore the presence of a Constant Amplitude Fatigue Limit (CAFL) of R-UHPFRC beams with two types of rebars and under various fatigue load levels. With almost 3 m^3 of UHPFRC casted for specimen fabrication, this research seems to be the most exhaustive experimental campaign on fatigue of R-UHPFRC realized hitherto.

Fatigue of UHPFRC and R-UHPFRC

Overview

Although UHPFRC is a relatively new structural material, there have been already several experimental campaigns on its fatigue resistance reported. The majority of experimental investigations on the fatigue behavior of UHPFRC and R-UHPFRC utilized relatively small specimens, i.e. they were conducted on the material level rather than on the structural level. As far as this kind of testing is crucial for understanding the fatigue process, it does not allow for observation of stress redistribution capacity and rebar-UHPFRC interaction. Therefore, some tests were executed on full-scale structural elements as well. The run-out limits at which the test was stopped and considered as no failure were varying from 1 to 20 million. Taking into account that some of the reported failures occurred after 1 or 2 million of cycles, it can be stated that for many campaigns the runout limit was not enough to identify CAFL of UHPFRC properly, as some of run-outs would have failed soon after the test was stopped. The CAFL is a fatigue loading level that, if fatigue stresses remain below this level, no continuous fatigue damage is produced in the material. Thus, the fatigue duration of a structural element subjected to fatigue loading below the CAFL is considered as infinite.

Furthermore, to obtain fatigue failures after a relatively low number of cycles, considerably high fatigue stresses were applied. Such an elevated fatigue loading, sometimes up to 90% of the static resistance of tested elements, is not realistic, as the requirements of structural safety at the Ultimate Limit State always need to be fulfilled. In addition, no variable stress amplitude testing was performed so far.

To search literature relevant for the current research, the following boundary conditions were set: 1) content of short steel fibers above 2% by volume to assure strain-hardening response; 2) largest particle size in the cementitious matrix below 2 mm; 3) at least two fatigue tests conducted in an experimental campaign. It is commonly agreed that the fatigue resistance of UHPFRC depends on the maximum fatigue load level, denoted as S-ratio between the maximum fatigue load and the ultimate static resistance of a given element.

Axial compressive fatigue tests

The traditional type of fatigue tests on cement-based materials is in uniaxial compression. An extensive testing campaign on different types of high-strength and ultra-high-strength cementitious materials with and without fibers was performed[134] to update the model used in the *fib* Model Code[135]. One of the tested materials was a UHPFRC with maximum grain size of 0.5 mm and 2.5% in volume of straight 9.0 mm long steel fibers of an aspect ratio of 60. It was shown that the CAFL is at 0.6S with respect to a 7 million cycles runout limit.

Another experimental campaign was performed on a UHPFRC (3.8% vol. steel fibers) similar to the one used in the present research[11]. Plate specimens (30mm x 100mm x 450mm) loaded on the smaller face were tested up to 20 million cycles, and CAFL at 0.6S was confirmed. The shape of specimens was mocking-up the use of UHPFRC in thin-walled elements such as wind turbine towers.

In real structures subjected to fatigue loading, the maximum compressive stress in structural elements rarely reaches half of the compressive strength of UHPFRC[20,96,133]. Additionally, design standards claim for 'ductile' failure modes of structural elements with materials (such as steel) failing in tension.

Consequently, it is considered that the fatigue resistance of R-UHPFRC elements is controlled by the material subjected to tensile stress, similarly to reinforced concrete structures[39,136–138]. Therefore, the fatigue resistance under compressive fatigue stress is not relevant for structural elements.

Axial tensile fatigue tests

UHPFRC with 2.5% vol. of steel fibers was tested in direct tension[139] up to 5 million cycles. It was found that the material can withstand fatigue cycles higher than 0.5S. However, for specimens where the maximum stress was above the elastic limit stress f_e, gradual reduction of stiffness occurred even for runouts indicating damaging process and the likelihood of fatigue failure if the tests were continued.

An extensive campaign was conducted[111] on material with 3.3% vol. steel fibers and runout limits varying between 5 and 20 million. They linked CAFL with the maximum stress applied in the cycle and equal $0.7f_e$ (0.6S) for material in elastic domain, $0.6f_e$ (0.5S) when the specimen was pre-loaded to strain-hardening domain and $0.45f_e$ (0.4S) for specimens pre-loaded to the post-peak softening domain.

The same UHPFRC with incorporated steel reinforcement bars was also tested[114]. The authors reported that the response of R-UHPFRC subjected to direct tensile fatigue stress comprised three regimes depending on maximum fatigue force F_{max} applied: 1) F_{max}≤0.23S: both UHPFRC and rebars below the CAFL, 2) 0.23S<F_{max}≤0.54S: UHPFRC above the CAFL, but the stress amplitude in the rebar remains below the CAFL, thus the R-UHPFRC remains below the CAFL, 3) F_{max}>0.54S: both UHPFRC and rebar are above the CAFL, and thus fatigue failure occurs. In the third regime, UHPFRC acts as a stress reducing and distributing agent, increasing the element's fatigue resistance. In the first part of the test, the global deformation was growing when UHPFRC is damaged, then remains almost constant until rebar failure. Only one type of element was tested.

Bending tests

Numerous fatigue tests on UHPFRC executed under flexure are presented in Table 6-1. Although for some experimental series a surprisingly high CAFL is found, it can be taken that the CAFL lies at a fatigue loading level of about half of the ultimate static specimen resistance. All reported tests were run under low minimum force level, i.e. F_{min} < 0.1S.

Table 6-1. Summary of flexural fatigue tests on UHPFRC.

Reference	Specimen dimensions [mm]	Fibre content [% vol.]	Runout (x10^6)	CAFL (S)
Four-point bending				
Parant et al., 2007[140]	40 x 200 x 600	11	2	0.5
Lappa, 2007[141]	125 x 125 x 1000	2.5	10	0.55
Three-point bending				
Behloul et al., 2005[142]	100 x 100 x 400	2	1	> 0.5
Farthat et al., 2007[65]	35 x 90 x 360	8	20	0.85
Farhat et al., 2007[65]	100 x 100 x 500	8	1	< 0.7
Naaman and Hammoud, 1998[143]	100 x 100 x 400	2	5	0.65
Three-point bending notched				
Ríos and Cifuentes, 2018[144]	100 x 100 x 440	2.5	2	0.49
Carlesso et al., 2019[145]	75 x 75 x 275	2	2	0.65

Bi-axial bending fatigue resistance was investigated[146] with ring-on-ring fatigue tests using 50 mm thick circular UHPFRC slabs with a diameter of 1'200 mm. The utilized UHPFRC was the same mix as used by Loraux[11], with 3.8% vol. steel fibers, and similar to the one used in the present research. The authors have shown that under bi-axial fatigue stress the CAFL is similar as under uniaxial bending, thus 0.54S. Interestingly, this is the load level at which the UHPFRC reaches f_{Utu} on the bottom face of the specimen. This shows that the relative material fatigue resistance is higher in bending than under direct tensile stress which may be due to significant stress redistribution capacity of UHPFRC. The size of the specimen was sufficiently large such that it can be considered as a full-scale test mocking up the real performance of a UHPFRC slab.

Findings from the literature review

Literature review reveals that most tests have been conducted using small specimens. There were few fatigue tests on structural elements involving UHPFRC[139,147] or R-UHPFRC[113,115,148–152]. However, in most experimental campaigns only one or two specimens were tested, not allowing for closer investigation of fatigue damage mechanism and resistance of the element. All of them were run under low minimum force (F_{min} < 0.1S) and have shown that CAFL ≥ 0.5S.

Materials and methods

Experiment set-up

Three types of beams were tested: Type I with a single Ø20 mm rebar; Type II with a single Ø34 mm rebar and Type III with Ø20 mm rebar and Ø6 mm Ω shaped stirrups (Figure 6-1). The beams were casted in horizontal position (as tested), pouring the fresh UHPFRC from top at one end. Six external vibrators were used to assure good flow of the fresh UHPFRC. Each casting comprised three identical beams, two to be tested under fatigue loading and one to be tested under quasi-static loading to determine the ultimate resistance as reference value.

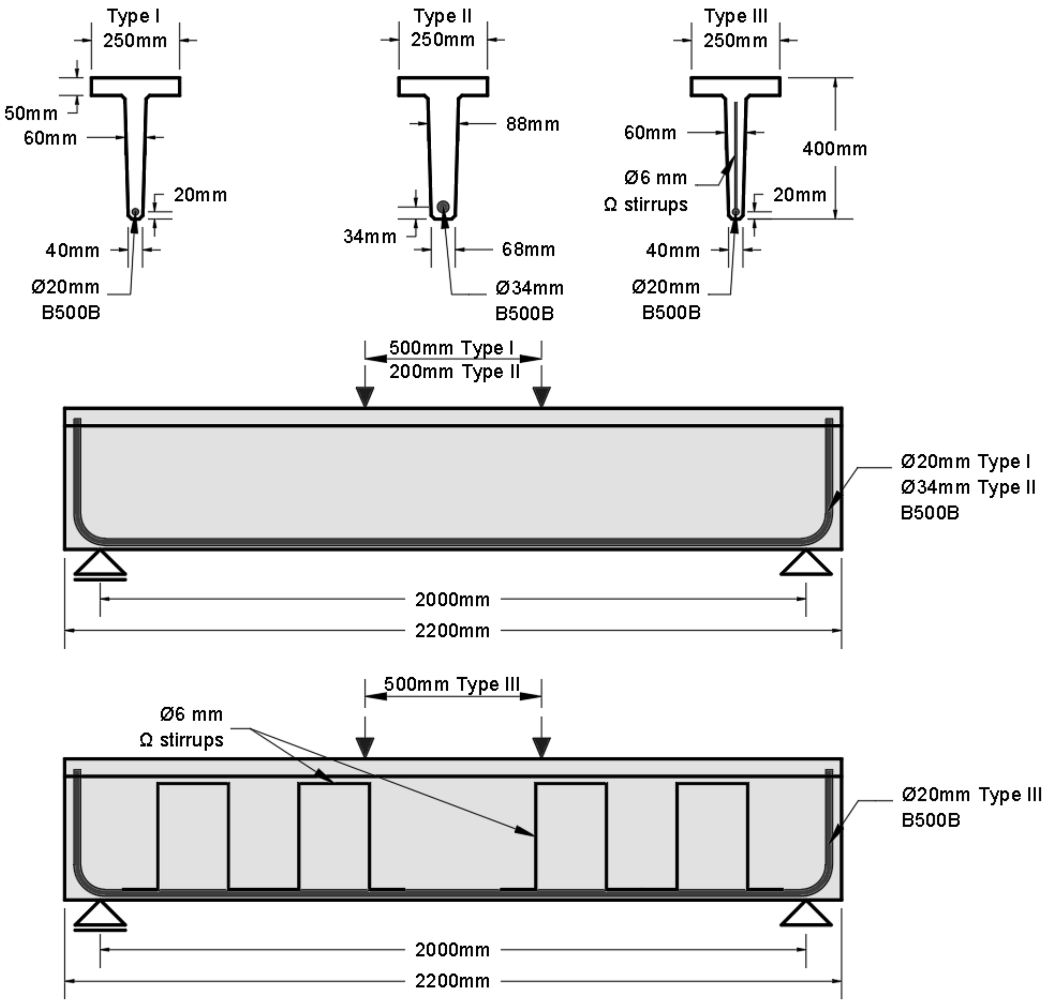

Figure 6-1. Scheme of beams under testing.

All beams were tested under four-point bending. Loading was applied using one servo-hydraulic actuator and a steel redistribution beam of high stiffness. The application points were positioned symmetrically at ±250 mm from mid-span for beams Type I and III, and at ±100 mm for Type II. Smaller spacing was adopted for Type II beams to avoid shear failure. For the same reason Type II beams were strengthened using externally mounted posttensioned stirrups. This solution was chosen to limit the size of tested element, instead of increasing the beam span. Furthermore, longer span would increase the beam deflection and thus the actuator's stroke, limiting the frequency of loading cycles and thus increasing the time necessary for testing. Since the beams were tested under four-point bending, the shear strengthening did not affect the bending strength.

All beams were instrumented with extensometers glued on the UHPFRC surface at the level of the reinforcement bar, along the constant bending moment zone. The measurement base was equal to 100 mm. The force was measured with the force cell of the actuator. Some of the beams were equipped with foil strain gauges glued on the rebar before casting.

The testing rig was able to accommodate two beams at the time, reducing the duration of the experimental campaign. Each beam was loaded with a separate actuator, and thus the two tests were conducted independently.

Materials

Commercially available UHPFRC mix Holcim710® was used, with 3.8% in volume of 13 mm long straight steel fibres with an aspect ratio of 65. The minimum age at the moment of testing was three months. The cement hydration in UHPFRC is largely advanced after 28 days and nearly complete after 90 days. Therefore, the age of testing of the R-UHPFRC beams has no notable influence on the material properties[87]. To confirm this, UHPFRC was tested in four-point bending according to Swiss standard[20] at the age of 28 and 90 days. The testing was done for four castings, leading to eight testing series, with six 30 mm x 100 mm x 500 mm plates for each series. The following properties were determined: 1) elastic limit stress f_{Ute}; 2) tensile strength f_{Utu}; 3) hardening strain at tensile strength ε_{Utu}; and 4) modulus of elasticity E_{Ut}. The average values presented in Table 6-2 show that after 28 days no significant increase in strength properties is noticed. The average compressive strength was f_{Uc} = 140MPa.

Table 6-2. Mean tensile material properties of UHPFRC based on four-point bending tests of plates.

	f_{Ute} [MPa]	f_{Utu} [MPa]	ε_{Utu} [‰]	E_{Ut} [GPa]
28 days	5.50	11.48	3.38	40.01
90 days	5.55	12.00	3.52	41.09
Average	5.52	11.75	3.46	40.59

Both longitudinal rebars and stirrups were of type B500B according to Swiss[43] and European[42] standards, with nominal yielding stress f_{sk} = 500 MPa, quenched and self-tempered. The properties of the longitudinal reinforcement bars were obtained using direct tension test and are presented in Table 6-3. The rebars used in Type I beams have higher strength. However, they still conform to the requirements of B500B reinforcement bar class. Due to large differences in strength values of reinforcement bars, Type I and III beams are treated separately.

Table 6-3. Mean tensile material properties of reinforcement bars based on axial tensile tests.

Beam type	f_s [MPa]	f_t [MPa]	ε_u [%]
Type I (Ø20mm)	600	687	9.2
Type II (Ø34mm)	525	624	9.4
Type III (Ø20mm)	512	617	9.2

Test description

In the beginning of each fatigue test, pseudo-static cycles were imposed under displacement control of the actuator. Before reaching the maximum force foreseen for fatigue testing F_{max}, gradual loading was applied. Several unloadings to the minimum testing force F_{min} were executed from increasing force levels to determine the residual strain when UHPFRC enters the strain-hardening domain. This procedure also allows comparing with the reference beam and confirming the same structural behavior and resistance.

After this initial quasi-static part, the actuator was switched to force-control mode, and the fatigue test started. Sinusoidal constant amplitude force was applied with a frequency varying between 3.3Hz and 4.5Hz, depending on the response of the testing rig under the applied loading. It may be assumed that frequencies below 10Hz have no influence on the fatigue resistance of UHPFRC[11,141,153,154]. Testing frequencies higher than 10Hz can be detrimental for fatigue resistance[155] due to increased temperature of the specimen modifying the viscoelastic behavior and thermal expansion of the cementitious matrix[156]. To guarantee that no such effect takes place, some of the beams were instrumented with thermocouples embedded in UHPFRC before casting, as well as glued on the surface. As no thermal gradient was recorded, it may be assumed that the testing frequency had no influence on the results.

Despite the relatively high frequency of fatigue cycles imposed to the beams, a test could take more than one month. For one of the beams almost 27 million fatigue cycles were reached, which may be the longest-lasting fatigue test on an UHPFRC structural element ever reported, with three months of testing duration.

All three types of beams were subjected to two groups of fatigue loading, with low minimum force (F_{min} < 0.1S) and high minimum force (F_{min} ≈ 0.35S). This range is representative for typical bridge structures.

Results

Table 6-4 presents the results of all fatigue test executed in this study, fourteen beams in total. The runouts, thus beams which did not fail under the imposed fatigue loading until end of the test, are marked with (R) next to the number of cycles. The stress in the reinforcement bar was calculated using UHPFRC properties obtained by means of an inverse analysis of the reference beam, taking into account the loading-unloading behavior due to strain-hardening as described in Chapter 4.

Table 6-4. Summary of fatigue tests; runouts are marked with (R); stress levels (σ) and stress ranges (Δσ) refer to the reinforcement bar.

№	Type	№ of cycles (M)	M_{min} (S)	M_{max} (S)	σ [MPa]	Δσ [MPa]	Stress transfer increase	Increased Δσ [MPa]
1	I	7.8 (R)	0.06	0.53	140-292	152	1.6	243
2	I	15.1 (R)	0.06	0.53	140-292	152	1.6	243
3	I	0.3	0.33	0.81	298-497	199	1.35	269
4	I	1.1	0.33	0.68	262-390	128	1.35	173
5	I	0.4	0.03	0.53	150-313	163	1.6	261
6	II	8.6 (R)	0.04	0.47	65-223	158	1.3	205
7	II	0.3	0.36	0.79	230-460	230	1.1	253
8	II	6.3	0.04	0.53	62-225	163	1.3	212
9	II	0.9	0.04	0.53	62-225	163	1.3	212
10	II	10.0 (R)	0.36	0.71	233-365	132	1.1	145
10A		1.0	0.36	0.77	245-416	171	1.1	188
11	II	1.8	0.37	0.77	261-416	155	1.1	171
12	III	2.4	0.05	0.56	131-283	152	1.6	243
13	III	0.8	0.33	0.79	285-436	151	1.35	204
14	III	26.0 (R)	0.09	0.53	131-262	131	1.6	210
14A		0.8	0.09	0.59	161-319	158	1.6	253

Global fatigue resistance

Previous studies[11,134] have shown that the CAFL of UHPFRC in compression is equal to 60% of ultimate static resistance. In the present beams, this magnitude of stress is reached only at the ultimate bending resistance. Therefore, as expected, all beams failed due to fatigue damage of UHPFRC in the bottom tensile part of the web and fatigue rupture of the reinforcement bar. No UHPFRC cracking or matrix spalling was observed in compressed portion of the member.

According to other authors[114,146,157], the fatigue resistance of UHPFRC depends on the imposed maximum fatigue stress. However, all their tests were executed in the low minimum force domain. To visualize the influence of both maximum and minimum load, the modified Goodman diagram is suitable to present results

(Figure 6-2). For each fatigue test the normalized mean cyclic load is marked on the abscissa, and both maximum and minimum loads are on the ordinate axes. Failures are marked with an X, runouts with a circle. The fatigue safe region is delimited with two straight dashed lines enclosing the runout tests and crossing in point (1,1) standing for the quasi-static ultimate resistance. Similar approach was used for reinforcement bars in other research[158].

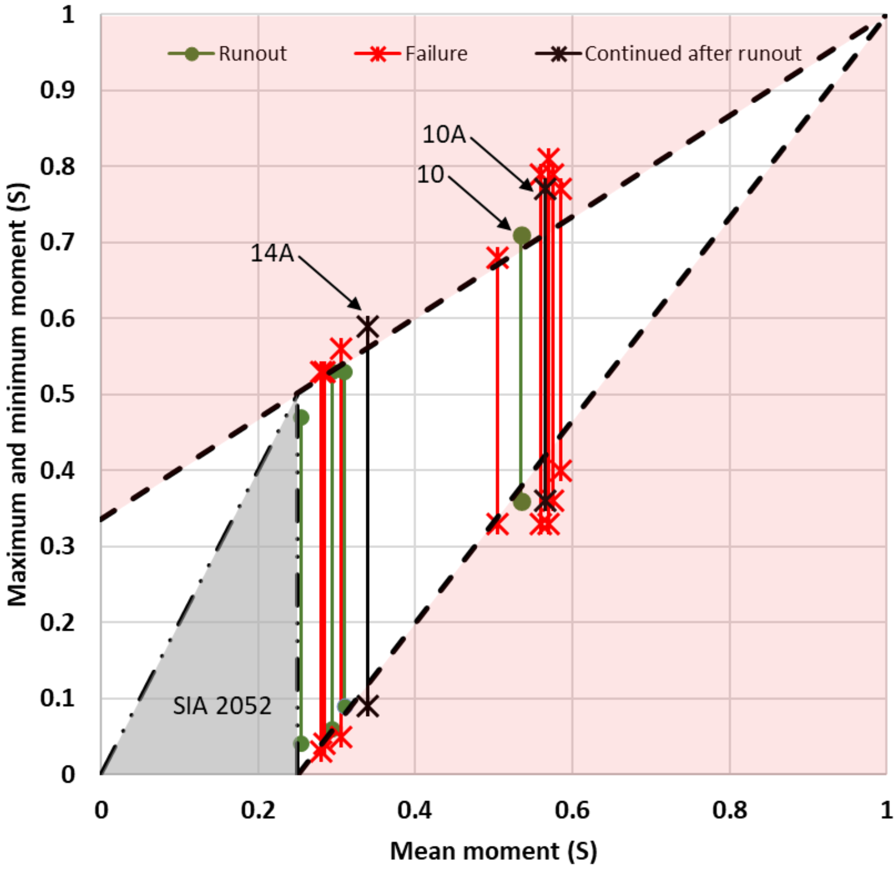

Figure 6-2. Modified Goodman diagram showing all fatigue tests results.

The results presented in Figure 6-2 show a clear delimitation between fatigue-failure and fatigue-safe domains. All fatigue tests with failure lie within the fatigue failure domain. Only Test 10 is a runout which theoretically should have failed. However, after a slight increase of F_{max}, the beam (Test 10A) failed after relatively few fatigue cycles. The scatter of results is rather limited for fatigue tests. This shows that the assumption of the fatigue safe domain is realistic. Interestingly, Test 14 was subjected to over 26 million fatigue cycles and showed no failure. After load increase into the fatigue failure domain, Test 14 specimen failed after 1 million cycles (Test 14A).

For the sake of comparison, the validity zone of fatigue design provisions for R-UHPFRC members in SIA 2052[20] is presented as shaded area. The standard suggests global fatigue verification on the member level with the CAFL in bending being equal to half of the ultimate static resistance. This relation is valid up to F_{max}=0.5S if minimum force is close to zero.

All test results follow the same trend, irrespective of type of reinforcement bar, and are consistent thanks to the normalization of the fatigue stress level with respect to the ultimate static resistance. Consequently, the presented modified Goodman diagram is applicable to any kind of R-UHPFRC member.

Fatigue stress range in the reinforcement bar

According to previous research[114,157] the strain, and therefore stress, in rebars is growing during the first 0.5 million of cycles. The degree of growth is dependent on the reinforcement ratio[157]. Therefore, the strain growth is presented separately for beams with Ø20 mm and Ø34 mm rebars. Under the assumptions of a) perfect bond between UHPFRC and reinforcement bar[89] and b) UHPFRC bulk material being a continuum before reaching ε_{Utu}, the strain increase measured on the surface of UHPFRC is identical with strain increase in the reinforcement bar.

These assumptions are confirmed by direct strain measurements on the reinforcement bar using strain gauges. In Figure 6-3, the strain ranges measured for the whole duration of the tests are presented for both failure and runout tests as well as for high and low minimum force levels. The strain range is normalized with respect to the values measured during the 1st cycle ($\Delta\varepsilon_1$) to quantify its increase during the whole test duration. The number of cycles is normalized with respect to the total number of cycles. Also, the Young's modulus of steel rebars is assumed to remain constant during the fatigue test. The strain range increases quickly during the first part of the test and remain stable for most of the time i.e., in the range from 0.1 to 0.9 of normalized cycles. The strain range is fatigue-relevant during this static part, therefore should be taken into account during fatigue resistance verification of rebars.

The strain range increase measured for beams of Type I (Ø20 mm rebars) and Type II (Ø34 mm) are presented in Figure 6-3. For all tests, the growth measured with extensometers is similar to, or larger than, the one measured with strain gauges. This may be explained either by a transverse strain gradient in the beam or by the fact that extensometers cover a much larger area of the beam while strain gauges are installed locally. Therefore, not all the regions with increased strain can be identified using strain gauges. Consequently, the values obtained with extensometers should be taken as representative for the constant bending moment zone. The increase of strain range for both failure and runout tests is similar. For beams with F_{min} <0.1S, the rise is higher than for beams on high minimum force levels. This may be due to stress redistribution and additional microcracking of UHPFRC. For highly stressed beams, this microcracking is already well developed after the 1st loading cycle, and consequently, there is a rather low energy dissipation capacity.

The decrease of strain range measured with one of the extensometers in Test 4 (Figure 6-3 b)) is probably due to rapid deterioration of UHPFRC nearby. This led to local unloading of the material and thus decrease of strain measured by the neighbouring extensometer. Importantly, despite this weakening observed, this beam survived more than 1 million fatigue cycles confirming significant redistribution capacity of UHPFRC.

From the above, it can be deduced that the maximum rise of stress range in the rebar due to fatigue of UHPFRC is equal to:

- 60% (1.6 of strain range in 1st cycle $\Delta\varepsilon_1$) for Ø20 mm bar and 30% (1.3 $\Delta\varepsilon_1$) for Ø34 mm bar for the tests with low minimum fatigue force level (F_{min} <0.1S), and
- 35% (1.35 $\Delta\varepsilon_1$) for Ø20 mm bar and 10% (1.1 $\Delta\varepsilon_1$) for Ø34 mm bar for the tests with high minimum fatigue force level (F_{min} ≈0.35S).

For both rebar diameters, the ratio of strain range increase between low and high minimum force level tests is the same. This ratio is equal to 1.18 (1.6/1.35=1.3/1.1=1.18), thus proportional to F_{min}, irrespective of beam type.

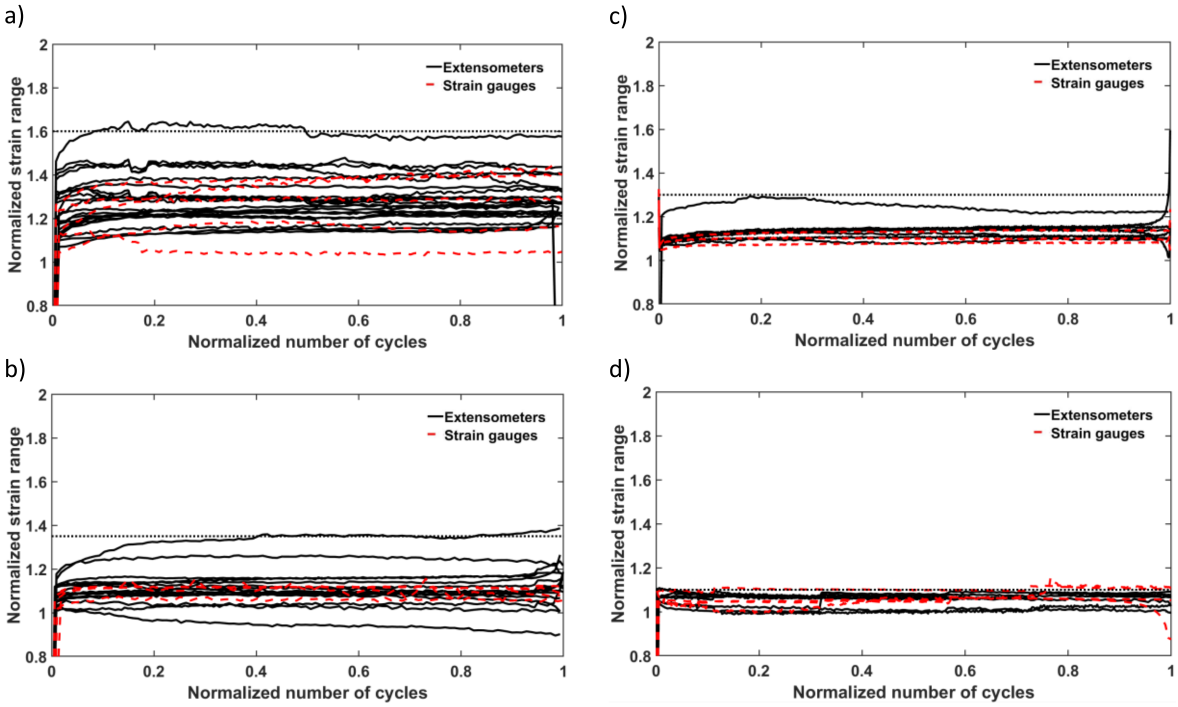

Figure 6-3. Normalized strain range variation during the fatigue test: a) Type I beams, F_{min} <0.1S (Tests 1, 2 and 5); b) Type I, F_{min} ≈0.35S (3,4); c) Type II , F_{min} <0.1S (6,9); d) Type II, F_{min} ≈0.35S (10,11).

Makita and Brühwiler[157] stated that the increase of stress range in rebars is inversely proportional to reinforcement ratio of element. In the present study, this simple rule was not confirmed. The ratio of stress range increase for Ø20 mm and Ø34 mm rebar is 23% (1.6/1.3=1.35/1.1=1.23) while the proportion of the two reinforcement ratios is 43% (1.0%/2.3%=0.43), and 1/0.43=2.33. Therefore, the present test results do not allow to define a relationship between reinforcement ratio and increase in stress range in rebar.

The obtained factors were used to calculate the acting stress range in the rebar, based on the stress range in the first cycle obtained with the inverse analysis method, as given in Table 6-1. The stress ranges in rebars calculated in this way are presented in Figure 6-4 on the S-N curves for Quenched and Self-Tempered (QST) rebars[159]. Tests that do not follow closely the results from the previous study are presented with their respective test numbers.

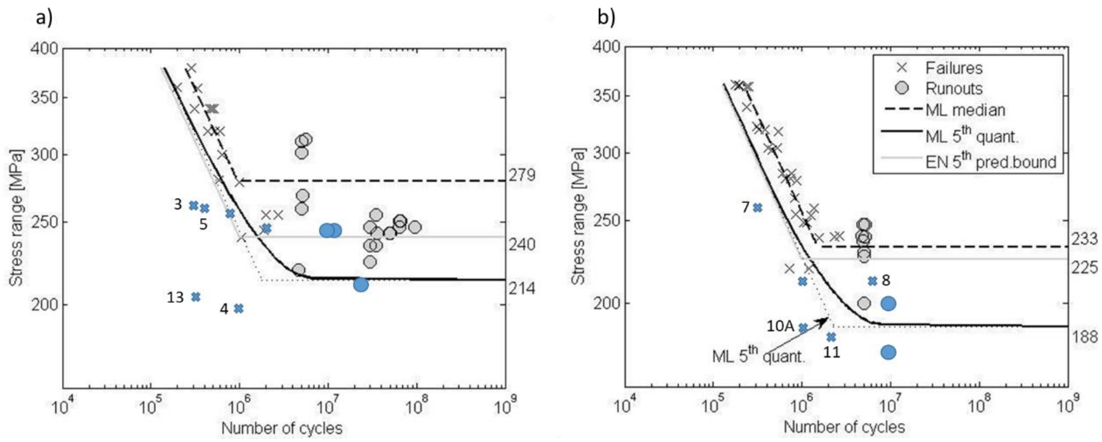

Figure 6-4. Present test results projected on the S-N curves[159] with rebar diameter a) ≤20 mm and b) >20 mm.

Figure 6-4 reveals that all tests which do not comply with results of reinforcement testing[159] ended with premature failure. If the fatigue verification of these beams had been performed only regarding stress range in rebars, unexpected structural failures would occur. This demonstrates importance of two-level fatigue verification including the global fatigue resistance check with the modified Goodman diagram.

Test 8 with fatigue failure, should have been a run-out test according to the S-N curves for rebars. This beam failed after more than 6 million cycles, while the runout limit adopted for rebar diameter larger than 20 mm was 5 million cycles. Thus, this test would have been classified as a runout.

Test 9 failed much earlier (0.9M) under same loading indicating that the scatter in R-UHPFRC beams could be higher than for rebars tested alone. This may be explained by stress localization resulting from non-uniform microcracking or localized fatigue damage of the UHPFRC.

Test 5 is the only test with low minimum fatigue stress level that failed earlier than expected when considering the stress range in the rebar. The applied loading range was ΔM = 0.5S, therefore it would comply with the fatigue provision in SIA 2052[20], while it is just outside the no failure criterion using the proposed modified Goodman diagram (Figure 6-2). This shows again that both maximum and minimum fatigue load levels need to be considered in fatigue design provisions.

All tests with high minimum fatigue load level failed earlier than expected when considering the stress range in the rebar. The stress transfer from the UHPFRC to the rebar is taken into account using the previously determined increment factors. Therefore, the obtained results suggest that the fatigue resistance of contemporary quenched and self-tempered reinforcement bars is dependent not only on the stress range, but also on the minimum stress, similarly to hot-rolled bars[158,160,161].

Discussion of Test 10

As mentioned previously, Test 10 should have failed according to the modified Goodman diagram given in Figure 6-2. That is why it needs to be discussed together with Test 10A and 11 for comparison. Test 11 was subjected to a similar fatigue stress level comparing to Test 10. The beams were casted together and can thus be considered as identical.

The calculated stress profiles in the UHPFRC under maximum and minimum fatigue load are presented in Figure 6-5. The stress values were calculated using the material properties obtained from inverse analysis of the reference beam as described in Chapter 4. However, the increase of stress range in the reinforcement bar discussed previously is not taken into account.

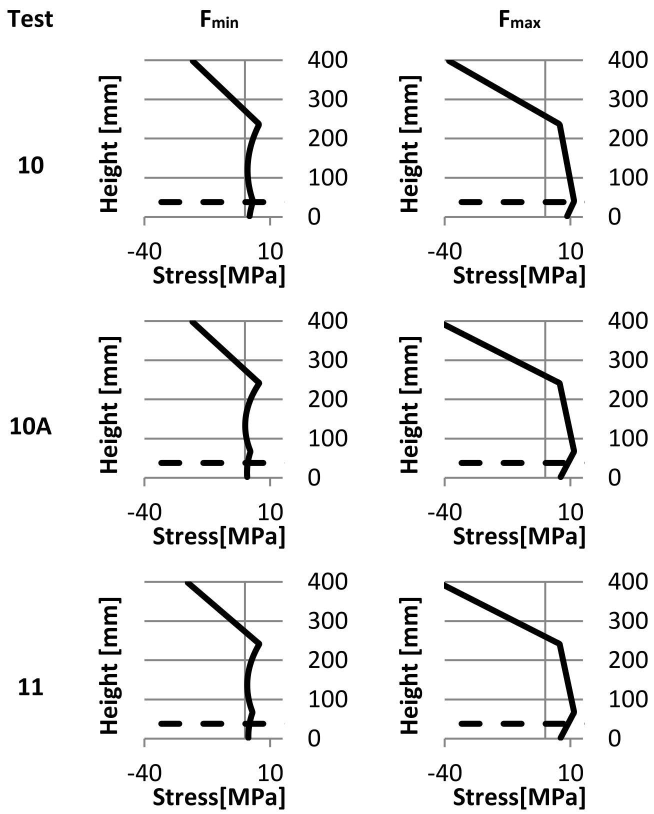

Figure 6-5. Stress profile over the beam height in the UHPFRC for Tests 10, 10A and 11. The dashed line marks the position of the rebar.

At first sight, the stress profiles of all three beams seem to be similar. Importantly, the level below which UHPFRC enters strain softening, i.e. the height at which tensile stress equal to f_{Utu} is reached, is different. In Tests 10A and 11, it lies above the rebar axis, while in Test 10 it is below. As the UHPFRC cover is thin (Ø/2), it can be assumed that the UHPFRC of the very bottom part of the beam is not fully contributing to the global response. Furthermore, the alignment of fibers in this region, due to the small spacing between rebar and formwork, probably leads to locally increased f_{Utu}[72]. Hence, UHPFRC stress in this region is below the tensile strength, contrary to results obtained for the whole beam by inverse analysis. This local variation of stress transfer capacity and tensile strength of UHPFRC may be the reason why no fatigue damage initiated and propagated. This is why Test 10 lies just in the failure domain of the modified Goodman diagram, but did not fail. To grasp local variation of tensile resistance, an inverse analysis with stratification or randomization of material properties could be performed[162]

Conclusions

This chapter presents the results of an experimental campaign on the fatigue resistance of fourteen full-size R-UHPFRC beams tested in four-point bending under both low and high minimum fatigue load levels. The following conclusions are drawn:

- The fatigue resistance of R-UHPFRC beams depends on both the minimum and maximum fatigue load level. The proposed modified Goodman diagram accordingly describes the fatigue resistance.

- Significant stress redistribution capacity takes place in the UHPFRC during fatigue loading influencing the stress range and thus the fatigue strength of steel reinforcement bars. The fatigue stress range in the rebar increases by 30% for Ø34 mm rebars and by 60% for Ø20 mm rebars, in the case of low minimum fatigue load (F_{min}<0.1S). In the case of high minimum fatigue load (F_{min} ≈0.35S), the corresponding stress increase is 10% for Ø34 mm rebars and 35% for Ø20 mm rebars. Thus, stress redistribution in the UHPFRC is less pronounced at higher stress level.

- The fatigue resistance of R-UHPFRC beams shall be verified both 1) globally with respect to beam fatigue resistance using the modified Goodman diagram, and 2) locally with respect to the fatigue stress in the reinforcement bar considering stress increase due to UHPFRC – rebar interrelation.

- No fatigue failure occurs if 1) the normalized maximum and minimum loads lie within the safe region of the modified Goodman diagram; and 2) the stress range in the steel reinforcement bar, with increase due to stress redistribution taken into account, is below the Constant Amplitude Fatigue Limit of the given rebar.

Chapter 7 Conclusions and future work

On lessons learned and knowledge gained during this research, as well as on possible ways of continuation and further development

The research presented in this manuscript was oriented towards understanding the fatigue of structural elements. It approached the problem from two sides: 1) demands that are imposed on a structure (part “S”), and 2) fatigue resistance and behaviour of Ultra High Performance Fibre Reinforced Cementitious composite (UHPFRC).

The knowledge gained in this research is presented following the areas of interest defined in Chapter 1.

Demands

To understand the nature of fatigue loading and develop better methods for monitoring of the structural response due to this type of actions, data obtained during long-term monitoring of two road bridges was used. Chillon viaduct is a massive prestressed concrete structure carrying a highway. Crêt de l’Anneau viaduct is a lightweight steel-concrete composite structure within a secondary road. The two structures are located in Western Switzerland.

Thanks to the fact that the two viaducts are constructed differently, and the traffic which they carry is of dissimilar nature due to the class of road they carry, these findings can be generalized for the whole population of road bridges.

Fatigue-relevant actions and optimal data analysis

- In massive concrete bridge structures, stress ranges due to traffic loading and temperature action can be of similar magnitude.
- Stress variation due to the partially restrained thermal expansion is fatigue relevant when combined with high traffic-induced stress cycles. The two action effects should be treated together to identify relevant combinations.
- Windowing of 24h using the rainflow counting algorithm is effective to gather thermally induced stress ranges with sufficient precision.
- The yearly and seasonal cycles of residual stresses due to restrained thermal expansion are not fatigue relevant, and thus, they do not need to be considered for fatigue safety verification.
- Measured stress values are significantly smaller than the corresponding stress values obtained from calculation using load models as defined in standards.

Influence of duration of monitoring on results

- The minimum monitoring duration for road bridges is 100 days; if the monitoring is shorter, the collected data cannot be considered as reliable.
- Since the structural response can be highly dependent on ambient temperature, the recommended season to conduct short-term monitoring is during summer months with high temperatures.
- Possible seasonal variation of traffic must be taken into account in the planning of short-term monitoring; however, the two case studies did not reveal such variation.

Translation of monitoring results to long-term behaviour

- The extrapolation of the cumulative fatigue damage obtained on the basis of monitoring of fatigue action effects should be done taking into account the duration of the monitoring campaign. This time span determines the representativity of collected data for the nature of traffic on the given road bridge. The monitoring duration-dependent Cumulative Damage correction Factor γ_{CDF} was proposed to take into account this uncertainty. The fatigue damage obtained through direct measurements should be multiplied by this factor before the extrapolation to obtain results which are on the safe side. The results are less conservative comparing to method proposed in Eurocodes, therefore lead to more economic, but safe, outcome.

- For most cases, γ_{CDF}=4 is suggested for cumulative damage extrapolation after 100 days of monitoring, and γ_{CDF}=1.3 after 1 year.

- For highly temperature sensitive structures, factor of γ_{CDF}=20 (or Eurocode method) should be used for accumulated damage after 100 days of monitoring and γ_{CDF}=2.5 after 1 year-long monitoring; to reduce these values, longer monitoring can be considered.

Resistance

To investigate the resistance of reinforced UHPFRC (R-UHPFRC) structural elements, an experimental campaign on full-scale beams was conducted. With almost 3m^3 of material casted, 14 members tested under fatigue loading and tests running up to 27 million cycles (3 months of testing) it seems to be the largest and most exhaustive campaign on fatigue of UHPFRC ever performed.

Stress distribution in R-UHPFRC element under loading-unloading

- The inverse analysis method can be used also for large elements, like full-scale beams, including elements with reinforcement bars. Thanks to that, the material properties can be precisely determined for the sake of modelling, inherently taking into account variation due to shape and size of the structural element.

- UHPFRC in the tensile zone of the R-UHPFRC member enters into compression if it was previously loaded beyond the elastic limit stress. This phenomenon leads to significantly increased tensile strain in the rebar at the unloaded state and thus influences the global response of the structural member. This increase is largely notable in particular at high loading level.

- Magnetic NDT is a reliable method allowing to determine the UHPFRC tensile strength f_{Utu} after calibration for a given UHPFRC mix. Better estimation of ultimate bending resistance of structural members is obtained than based on material testing because fibre distribution in the element is explicitly taken into account.

- Combination of material testing on smaller specimens and magnetic NDT is recommended to retrieve the full set of material properties. This method gives results comparable to UHPFRC characterization with inverse analysis of prototype element.

Fatigue behaviour and mechanism of R-UHPFRC

- The fatigue deformation behaviour of R-UHPFRC beam shows three stages: Stage I (0% - 10% of total number of fatigue cycles) with rapid increase of strains; Stage II (10% - 90%) with stable behaviour showing only little increase in strain, and Stage III (90% - 100%) with rapid increase of strain leading to fatigue failure.

- Fatigue failure of R-UHPFRC member is determined by the fatigue fracture of the steel reinforcement bar.

- Strain increase during Stages I and II is more important at minimum (F_{min}) rather than maximum (F_{max}) force in the fatigue cycle. This indicates that the fatigue damage of UHPFRC occurs under tensile-compressive stress reversal, possibly due to accumulation of pulverized, spalled particles of the cementitious matrix in microcracks.

- Fatigue damage occurs locally. During Stage III, local fatigue damage is visible in the strain range increase in the given section, but the reduction of stiffness is too small to influence the global member behaviour, i.e. deflection.

- The fatigue damage process in UHPFRC and rebar does not necessarily take place in the same cross-section, but nearby i.e. in the range of around 100 mm. However, the advanced fatigue crack propagation causes loss of bearing capacity of the rebar just prior to failure, overloading locally UHPFRC, which leads to localizing the final rupture in the same cross-section. This process takes place during sub-stage IIIa in the last 2‰ of test duration.

- The deflection range increases only in the last Stage IIIa, when the reinforcement bar can no longer transmit the tensile force.

- Beyond Stage I, no new matrix discontinuities appear. During Stage II, the maximum opening of matrix discontinuities remains stable, while the minimum opening constantly increases. These openings remain below 50 µm, therefore continuity of UHPFRC can be assumed.

Fatigue resistance of R-UHPFRC and proper design

- The fatigue resistance of R-UHPFRC beams depends on both the minimum and maximum fatigue load level. The proposed modified Goodman diagram accordingly describes the fatigue resistance.

- Significant stress redistribution capacity takes place in the UHPFRC during fatigue loading influencing the stress range and thus the fatigue strength of steel reinforcement bars. The fatigue stress range in the rebar increases by 30% for Ø34 mm rebars and by 60% for Ø20 mm rebars, in the case of low minimum fatigue load (F_{min}<0.1S). In the case of high minimum fatigue load (F_{min} ≈0.35S), the corresponding stress increase is 10% for Ø34 mm rebars and 35% for Ø20 mm rebars. Thus, stress redistribution in the UHPFRC is less pronounced at higher stress level.

- The fatigue resistance of R-UHPFRC beams shall be verified both 1) globally with respect to beam fatigue resistance using the modified Goodman diagram, and 2) locally with respect to the fatigue stress in the reinforcement bar considering stress increase due to UHPFRC – rebar interrelation.

- No fatigue failure occurs if 1) the normalized maximum and minimum loads lie within the safe region of the modified Goodman diagram; and 2) the stress range in the steel reinforcement bar, with increase due to stress redistribution taken into account, is below the Constant Amplitude Fatigue Limit of the given rebar.
- For some cases, the maximum tensile stress in UHPFRC above the elastic limit stress f_{Ute} and close to tensile strength f_{Utu} did not cause fatigue failure of a beam. This demonstrates an advantage of proposed verification method over method based on limitation of maximum stress under fatigue, as proposed by other researchers and in particular French standard [163]

Future work

The most important work to be done is implementation of the knowledge into codes and provisions, and further into practice. There is a long-known aspect of structural codes being overly conservative, regarding both load models (dynamic factors and load levels) as well as resistance of materials and structures (S-N curves for reinforcement with the fatigue resistance half as high as obtained in testing). Many practitioners are either not aware of that, or they are not willing to step outside of the simple schemes of solving the equations provided by standards. Such a behaviour leads to many unnecessary and expensive interventions on the existing structures.

Regarding the research work, there are still many interesting questions to be answered about structural response of UHPFRC, like:

- Characterisation of the response of UHPFRC which entered strain-hardening domain, and later was unloaded or loaded into compression. It is crucial for calculation of stress amplitude due to fatigue cycles and necessary to foresee the structural response under serviceability loads.
- Fatigue tests on new formulations of UHPFRC with synthetic fibres. Different fatigue behaviour of fibres and fibre-matrix interface can be expected. Thanks to normalization of fatigue resistance with regard to static resistance, the results presented in this thesis can be directly applied for other recipes of UHPFRC with steel fibres.
- Variable amplitude fatigue tests on UHPFRC. They reflect the real structural response under fatigue actions much better than the constant amplitude loading.
- Fatigue tests on prestressed and composite UHPFRC-steel elements. Although on basis of existing knowledge the behaviour of such element can be foreseen, experimental verification can be beneficial.
- Fatigue tests of steel reinforcement bars under high minimum stress. Lack of literature on influence of minimum load level on fatigue resistance of modern quenched self-tempered reinforcement bars was identified. It seems important for fatigue resistance of R-UHPFRC elements, and therefore of reinforced concrete elements as well.

Annexes

The following annexes have been prepared to support this thesis and are available under the link https://osf.io/7ap6c/?view_only=a144c41d34a84576834cf5a794c6f1f1. All data and scripts are available at request in MCS EPFL archives.

Annex A – Monitoring of Chillon viaduct

Description of monitoring system, thermal loops on chosen days, analysis of stationarity of the data and reliability of the measurement system.

Annex B – Monitoring of Crêt de l'Anneau viaduct

Monitoring report of Crêt de l'Anneau viaduct with description of the system and analysis of data. The report was prepared by Christophe Loraux, Imane Bayane and Eugen Brühwiler : Rapport n° MCS 23.16.03-1 Surveillance du Viaduc du Crêt de l'Anneau par un monitoring à longue durée.

Annex C – Bootstrapping and extrapolation of data – Chillon

Bootstrapped data and figures presenting cumulative damage, confidence interval width, return level, confidence interval width indicators and Cumulative Fatigue Damage Correction Factors for 100 permutations starting in four seasons (400 in total for each gauge).

Annex D – Bootstrapping and extrapolation of data – Crêt de l'Anneau

Bootstrapped data and figures presenting cumulative damage, confidence interval width, return level, confidence interval width indicators and Cumulative Fatigue Damage Correction Factors for 100 permutations starting in four seasons (400 in total for each gauge).

Annex E – Tests on R-UHPFRC beams

Drawings of beams, list of tests with details, test reports and instrumentation schemes for each static and fatigue test.

Annex F – Material properties

Results of testing of UHPFRC plates and cylinders, reinforcement bars and inverse analysis of R-UHPFRC beams.

Annex G – Stress profile calculation

Details of stress profile calculation for two beams presented in Chapter 4.

References

1. Gkoumas, K. et al. Research and innovation in bridge maintenance, inspection and monitoring - A European perspective based on the Transport Research and Innovation Monitoring and Information System (TRIMIS). doi:10.2760/719505 (2019).
2. ASCE. 2017 Infrastructure Report Card. https://www.infrastructurereportcard.org/cat-item/bridges/ (2017).
3. van Breugel, K. Societal Burden and Engineering Challenges of Ageing Infrastructure. Procedia Engineering **171**, 53–63 (2017).
4. Global Alliance for Buildings and Construction, International Energy Agency and the United Nations & Environment Programme. 2019 global status report for buildings and construction: Towards a zero-emission, efficient and resilient buildings and construction sector. 41 (2019).
5. Embodied Carbon in Buildings: Measurement, Management, and Mitigation. (Springer International Publishing, 2018). doi:10.1007/978-3-319-72796-7.
6. Peduzzi, P. Sand, rarer than one thinks. https://na.unep.net/geas/archive/pdfs/GEAS_Mar2014_Sand_Mining.pdf (2014).
7. Nilimaa, J. et al. More Realistic Codes for Existing Bridges. in Challenges in Design and Construction of an Innovative and Sustainable Built Environment 9 (2016).
8. Refurbishment of Buildings and Bridges. (Springer-Verlag, 2002). doi:10.1007/978-3-7091-2570-0.
9. Bertola, N. J., Papadopoulou, M., Vernay, D. & Smith, I. F. C. Optimal Multi-Type Sensor Placement for Structural Identification by Static-Load Testing. Sensors **17**, 2904 (2017).
10. Treacy, M. A. The use of monitored data in the verification of structural and fatigue safety of existing post-tensioned concrete highway bridges. (École polytechnique fédérale de Lausanne, 2014).
11. Loraux, C. Long-term monitoring of existing wind turibine towers and fatigue performance of UHPFRC under compressive stresses. (EPFL, 2018).
12. Grigoriou, V. Advanced fatigue theory and structural response monitoring for safety verification of existing RC slabs subject to railway traffic. (EPFL, 2015). doi:10.5075/epfl-thesis-6847.
13. Makita, T. Fatigue behaviour of UHPFRC and R-UHPFRC - RC composite members. (École polytechnique fédérale de Lausanne, 2014).
14. Shen, X. Static and Fatigue Biaxial Flexural Behavior of Strain-Hardening UHPFRC Thin Slab Elements. (EPFL, 2020). doi:10.5075/epfl-thesis-7460.
15. Herwig, A. Reinforced concrete bridges under increased railway traffic loads. (EPFL, 2008). doi:10.5075/epfl-thesis-4010.

16. Brühwiler, E. et al. Strengthening the Chillon viaducts deck slabs with reinforced UHPFRC. in IABSE Symposium Report vol. 105 1–8 (International Association for Bridge and Structural Engineering, 2015).

17. Martín-Sanz, H., Avendano Valencia, L. D., Dertimanis, V., Chatzi, E. & Brühwiler, E. Monitoring of Chillon viaduct after Strengthening with UHPFRC. in (2018). doi:10.3929/ethz-b-000316309.

18. Denarié, E. SAMARIS D22 - Full scale application of UHPFRC for the rehabilitation of bridges – from the lab to the field. https://infoscience.epfl.ch/record/256517 (2005).

19. Brühwiler, E. UHPFRC technology to enhance the performance of existing concrete bridges. Structure and Infrastructure Engineering **16**, 94–105 (2020).

20. SIA 2052. Technical Leaflet SIA 2052, UHPFRC - Materials, design and construction, Swiss Society of Engineers and Architects, Zurich. (2017).

21. Hajar, Z. et al. Innovative solution for strengthening orthotropic decks using UHPFRC: the Illzach bridge. RILEM-fib-AFCF Int. Symposium on Ultra-High Performance Fibre-Reinforced Concrete (2013).

22. Toutlemonde, F., Marchand, P., Gomes, F. & Dieng, L. Using UHPFRC as a topping layer for orthotropic bridge decks: prototype validation. RILEM-fib-AFCF Int. Symposium on Ultra-High Performance Fibre-Reinforced Concrete (2013).

23. Unterweger, H. & Novak, F. Strengthening of orthotropic steel decks using UHPC: UHPC-concrete instead of asphalt layer for additional at least 50 years in service. ce/papers **1**, 4502–4511 (2017).

24. Gomes, F. Influence du revêtement sur le comportement en fatigue des dalles orthotropes : étude d'une solution en BFUP. (Université Paris-Est, 2012).

25. Anderegg, P., Brönnimann, R. & Meier, U. Reliability of long-term monitoring data. J Civil Struct Health Monit **4**, 69–75 (2014).

26. Frangopol Dan M., Strauss Alfred & Kim Sunyong. Bridge Reliability Assessment Based on Monitoring. Journal of Bridge Engineering **13**, 258–270 (2008).

27. Leander, J., Andersson, A. & Karoumi, R. Monitoring and enhanced fatigue evaluation of a steel railway bridge. Engineering Structures **32**, 854–863 (2010).

28. Li, Z. X., Chan, T. H. T. & Ko, J. M. Fatigue analysis and life prediction of bridges with structural health monitoring data — Part I: methodology and strategy. International Journal of Fatigue **23**, 45–53 (2001).

29. Sousa, H., Costa, B. J. A., Henriques, A. A., Bento, J. & Figueiras, J. A. Assessment of traffic load events and structural effects on road bridges based on strain measurements. Journal of Civil Engineering and Management **22**, 457–469 (2016).

30. Brownjohn, J. M. W. et al. Structural Health Monitoring of short to medium span bridges in the United Kingdom. Structural Monitoring and Maintenance **3**, 259–276 (2016).

31. Treacy, M. A. & Brühwiler, E. Action effects in post-tensioned concrete box-girder bridges obtained from high-frequency monitoring. J Civil Struct Health Monit **5**, 11–28 (2015).

32. Massicotte, B. & Picard, A. Monitoring of a prestressed segmental box girder bridge during strengthening. PCI Journal **39**, (1994).

33. Chen, C., Wang, Z., Wang, Y., Wang, T. & Luo, Z. Reliability Assessment for PSC Box-Girder Bridges Based on SHM Strain Measurements. Journal of Sensors **2017**, 13 (2017).

34. Barr P. J., Stanton J. F. & Eberhard M. O. Effects of Temperature Variations on Precast, Prestressed Concrete Bridge Girders. Journal of Bridge Engineering **10**, 186–194 (2005).

35. Lucas, J.-M., Virlogeux, M. & Louis, C. Temperature in the Box Girder of the Normandy Bridge. Structural Engineering International **15**, 156–165 (2005).

36. Barsotti, R. & Froli, M. Statistical Analysis of Thermal Actions on a Concrete Segmental Box-Girder Bridge. Structural Engineering International **10**, 111–116 (2000).

37. Schläfli, M. Ermüdung von Brückenfahrbahnplatten aus Stahlbeton. (1999) doi:10.5075/epfl-thesis-1998.

38. SIA 269/2. Swiss standard SIA 269/2:2011 Existing structures - Concrete structures. (2011).

39. Mallett, G. P. Fatigue of reinforced concrete. vol. 2 (HMSO, 1991).

40. Kromanis, R. & Kripakaran, P. SHM of bridges: characterising thermal response and detecting anomaly events using a temperature-based measurement interpretation approach. J Civil Struct Health Monit **6**, 237–254 (2016).

41. Hoffmann, K. Applyin the Wheatstone Bridge Circuit. https://www.hbm.com/en/7163/wheatstone-bridge-circuit/ (1974).

42. EC2. Eurocode 2: Design of concrete structures-Part 1-1: Genera rules and rules for buildings. (2005).

43. SIA 262. Swiss standard SIA 262:2014 Concrete Structures. (2014).

44. Favre, R., Hassan, M. & Burdet, O. Statistical Data Combined with Linear and Non-Linear Analysis to Interpret Bridge Load Tests. 4th International Conference on Short and Medium Span Bridges 1197–1208 (1994).

45. EC1. EN 1991-2: Eurocode 1: Actions on structures - Part 2: Traffic loads on bridges. (2003).

46. SIA 269/1. SIA 269/1 Existing structures - Actions. (2011).

47. Ludescher, H. & Brühwiler, E. Dynamic Amplification of Traffic Loads on Road Bridges. Structural Engineering International **19**, 190–197 (2009).

48. ASTRA, B. für S. Statistical Annual Reports of Swiss Federal Road Office (ASTRA) on Weight In Motion results for years 2003-2011. https://www.astra.admin.ch/astra/de/home/dokumentation/verkehrsdaten/daten-publikationen/gewichtserfassung.html (2019).

49. Brühwiler, E. Learning from the past to build the future, Editorial. Proceedings of the Institution of Civil Engineers - Engineering History and Heritage **170**, 163–165 (2017).

50. Olofsson, I. et al. Assessment of European railway bridges for future traffic demands and longer lives – EC project "Sustainable Bridges". Structure and Infrastructure Engineering **1**, 93–100 (2005).

51. SIA 269. Swiss standard SIA 269:2011 Existing structures - Bases. (2011).

52. Treacy, M. A., Brühwiler, E. & Caprani, C. C. Monitoring of traffic action local effects in highway bridge deck slabs and the influence of measurement duration on extreme value estimates. Structure and Infrastructure Engineering **10**, 1555–1572 (2014).

53. Sawicki, B. & Brühwiler, E. Long term monitoring of a UHPFRC-strengthened bridge deck slab using strain gauges. in SMAR 2019 (2019).

54. Lipari, A., O'Brien, E. J. & Capriani, C. C. A comparative study of a bridge traffic load effect using micro-simulation and Eurocode load models. in 3420–3427 (CRC Press, 2012).

55. Wang, J. Y., Ni, Y. Q. & Ko, J. M. Local damage detection of bridges using signals of strain measurements. in Proceedings of the 1st International Conference on Structural Health Monitoring and Intelligent Infrastructure (2003).

56. Ahmadivala, M. et al. Application of Time Series Methods on Long-Term Structural Monitoring Data for Fatigue Analysis. SMAR 2019 Programme and Downloads https://infoscience.epfl.ch/record/270411 (2019).

57. Bayane, I., Mankar, A., Brühwiler, E. & Sørensen, J. D. Quantification of traffic and temperature effects on the fatigue safety of a reinforced-concrete bridge deck based on monitoring data. Engineering Structures **196**, 109357 (2019).

58. Brühwiler, E. "Structural UHPFRC": Welcome to the post-concrete era ! in International Interactive Symposium on Ultra-High Performance Concrete vol. 1 (Iowa State University Digital Press, 2016).

59. MCS EPFL. UHPFRC Map Switzerland. Map of UHPFRC applications in Switzerland https://www.epfl.ch/labs/mcs/mcs-laboratory-for-maintenance-and-safety-of-structures/uhpfrc-map-switzerland/ (2020).

60. Azmee, N. M. & Shafiq, N. Ultra-high performance concrete: From fundamental to applications. Case Studies in Construction Materials **9**, e00197 (2018).

61. Yoo, D.-Y. & Yoon, Y.-S. A Review on Structural Behavior, Design, and Application of Ultra-High-Performance Fiber-Reinforced Concrete. Int J Concr Struct Mater **10**, 125–142 (2016).

62. UHPFRC 2013 - Proceedings of the RILEM-fib-AFGC International Symposium on Ultra-High Performance Fibre-Reinforced Concrete. (RILEM-fib-AFGC, 2013).

63. UHPFRC 2017 - Proceedings of the RILEM-fib-AFGC International Symposium on Ultra-High Performance Fibre-Reinforced Concrete. (RILEM-fib-AFGC, 2017).

64. Abdel, M., Nagai, K. & Matsumoto, K. Simplified Design Approach of Steel Fiber Reinforced Concrete Under Flexural Load. in Proceedings of the 10th International Conference on Fracture Mechanics of Concrete and Concrete Structures 8 (IA-FraMCoS, 2019). doi:10.21012/FC10.234838.

65. Farhat, F. A., Nicolaides, D., Kanellopoulos, A. & Karihaloo, B. L. High performance fibre-reinforced cementitious composite (CARDIFRC) – Performance and application to retrofitting. Engineering Fracture Mechanics **74**, 151–167 (2007).

66. Habel, K., Denarié, E. & Brühwiler, E. Experimental Investigation of Composite Ultra-High-Performance Fiber-Reinforced Concrete and Conventional Concrete Members. SJ **104**, (2007).

67. Qiu, M., Shao, X., Wille, K., Yan, B. & Wu, J. Experimental Investigation on Flexural Behavior of Reinforced Ultra High Performance Concrete Low-Profile T-Beams. Int J Concr Struct Mater **14**, 5 (2020).

68. Huang, B.-T., Li, Q.-H., Xu, S.-L. & Zhang, L. Static and fatigue performance of reinforced concrete beam strengthened with strain-hardening fiber-reinforced cementitious composite. Engineering Structures **199**, 109576 (2019).

69. Yang, I.-H., Joh, C. & Bui, T. Q. Estimating the Tensile Strength of Ultrahigh-Performance Fiber-Reinforced Concrete Beams. Advances in Materials Science and Engineering **2019**, 16 (2019).

70. Gao, D., Gu, Z., Tang, J. & Zhang, C. Fatigue performance and stress range modeling of SFRC beams with high-strength steel bars. Engineering Structures **216**, 110706 (2020).

71. Wang, B., Fang, R. & Wang, Q. Flexural Behavior of Fiber-Reinforced Self-Stressing Concrete T-Shaped Composite Beams. Advances in Civil Engineering **2020**, e8810440 (2020).

72. Oesterlee, C., Denarié, E. & Brühwiler, E. Strength and deformability distribution in UHPFRC panels. Processing Sequence in the Production of Engineered Cementitious Composites **1+2**, 390–397 (2009).

73. Brühwiler, E., Friedl, H., Rupp, C. & Escher, H. Bau einer Bahnbrücke aus bewehrtem UHFB. Beton- und Stahlbetonbau **114**, 337–345 (2019).

74. AFGC. Ultra High Performance Fibre-Reinforced Concretes, Recommendations, Revised edition, June 2013. (Association Francaise de Genie Civil, 2013).

75. López, J. Á., Serna, P., Navarro-Gregori, J. & Coll, H. A simplified five-point inverse analysis method to determine the tensile properties of UHPFRC from unnotched four-point bending tests. Composites Part B: Engineering **91**, 189–204 (2016).

76. López, J. Á., Serna, P., Navarro-Gregori, J. & Camacho, E. An inverse analysis method based on deflection to curvature transformation to determine the tensile properties of UHPFRC. Materials and Structures **48**, 3703–3718 (2015).

77. Qian, S. & Li, V. C. Simplified Inverse Method for Determining the Tensile Properties of Strain Hardening Cementitious Composites (SHCC). Journal of Advanced Concrete Technology **6**, 353–363 (2008).

78. Baby, F., Graybeal, B., Marchand, P. & Toutlemonde, F. UHPFRC tensile behavior characterization: inverse analysis of four-point bending test results. Mater Struct **46**, 1337–1354 (2013).

79. de Oliveira e Sousa José Luiz Antunes & Gettu Ravindra. Determining the Tensile Stress-Crack Opening Curve of Concrete by Inverse Analysis. Journal of Engineering Mechanics **132**, 141–148 (2006).

80. Denarié, E., Sofia, L. & Brühwiler, E. Characterization of the tensile response of strain hardening UHPFRC - Chillon viaducts. in Proceedings AFGC-ACI-fib-RILEM Int. Symposium on Ultra-High Performance Fibre-Reinforced Concrete, UHPFRC 2017 - Pro 106 242–250 (RILEM publications S.A.R.L., 2017).

81. Baril, M. A. et al. Effect of casting flow defects on the crack propagation in UHPFRC thin slabs by means of stereovision Digital Image Correlation. Construction and Building Materials **129**, 182–192 (2016).

82. Mezquida-Alcaraz, E. J., Navarro-Gregori, J. & Serna-Ros, P. Numerical validation of a simplified inverse analysis method to characterize the tensile properties in strain-softening UHPFRC. IOP Conf. Ser.: Mater. Sci. Eng. **596**, 012006 (2019).

83. Tailhan, J.-L., Rossi, P. & Parant, E. Inverse numerical approach to determine the uniaxial tensile behaviour of a stress hardening cement composite from its bending behaviour. in 914–922 (2004).

84. Rossi, P., Daviau-Desnoyers, D. & Tailhan, J.-L. Analysis of cracking in steel fibre-reinforced concrete (SFRC) structures in bending using probabilistic modelling. Structural Concrete **16**, 381–388 (2015).

85. Shen, X., Brühwiler, E. & Peng, W. Biaxial flexural response of Strain-Hardening UHPFRC circular slab elements. Construction and Building Materials **255**, 119344 (2020).

86. Pan, R., Brühwiler, E. & Shen, X. Nonlinear numerical analysis of R-UHPFRC railway Π-beams. in (2016).

87. Habel, K., Viviani, M., Denarié, E. & Brühwiler, E. Development of the mechanical properties of an Ultra-High Performance Fiber Reinforced Concrete (UHPFRC). Cement and Concrete Research **36**, 1362–1370 (2006).

88. Denarié, E. Personal communication (e-mails, meetings) January-April 2020. (2020).

89. Oesterlee, C. Structural Response of Reinforced UHPFRC and RC Composite Members. (École polytechnique fédérale de Lausanne, 2010).

90. Leutbecher, T. & Fehling, E. Tensile Behavior of Ultra-High-Performance Concrete Reinforced with Reinforcing Bars and Fibers: Minimizing Fiber Content. SJ **109**, 253–264 (2012).

91. DIANA FEA. (DIANA FEA BV, 2017).

92. Sadouki, H., Denarié, E. & Brühwiler, E. Validation of a FEA model of structural response of RC-cantilever beams strengthened with a (R-) UHPFRC layer. Construction and Building Materials **140**, 100–108 (2017).

93. Wille, K. & Naaman, A. E. Fracture energy of UHP-FRC under direct tensile loading. in Fracture Mechanics of Concrete and Concrete Structures - Recent Advances in Fracture Mechanics of Concrete - B. H. Oh, et al.(eds) (Korea Concrete Institute, 2010).

94. Visalvanich, K. & Naaman, A. Compliance Measured Fracture Toughness of Mortar and Fiber Reinforced Mortar. in Fracture Mechanics for Ceramics, Rocks, and Concrete (eds. Freiman, S. & Fuller, E.) 141–156 (ASTM International, 1981). doi:10.1520/STP28303S.

95. Müller, S. & Mechtcherine, V. Behaviour of Strain-Hardening Cement-Based Composites (SHCC) Under Force-Controlled Cyclic Loading. in Proceedings of the 9th International Conference on Fracture Mechanics of Concrete and Concrete Structures (IA-FraMCoS, 2016). doi:10.21012/FC9.169.

96. Naaman, A. E. Fiber Reinforced Cement and Concrete Composites. (Techno Press 3000, 2018).

97. Hannant, P. J. Fibre Cements and Fibre Concretes. (Wiley & Sons, 1978).

98. Naaman, A. E. A statistical theory of strength for fiber reinforced concrete. (Massachusetts Institute of Technolog, 1972).

99. Krenchel, H. Fibre Spacing and Specific Fibre Surface. RILEM Symp, Fibre Reinf Cem and Concr 69–79 (1975).

100. Stroeven, P. Stereological principles of spatial modeling applied to steel fiber-reinforced concrete in tension. ACI Materials Journal **106**, 213–222 (2009).

101. Wille, K., Tue, N. V. & Parra-Montesinos, G. J. Fiber distribution and orientation in UHP-FRC beams and their effect on backward analysis. Mater Struct **47**, 1825–1838 (2014).

102. Bastien-Masse, M., Denarié, E. & Brühwiler, E. Effect of fiber orientation on the in-plane tensile response of UHPFRC reinforcement layers. Cement and Concrete Composites **67**, 111–125 (2016).

103. Wuest, J. Comportement structural des bétons de fibres ultra performants en traction dans des éléments composés. (2007) doi:10.5075/epfl-thesis-3987.

104. Nunes, S., Pimentel, M., Ribeiro, F., Milheiro-Oliveira, P. & Carvalho, A. Estimation of the tensile strength of UHPFRC layers based on non-destructive assessment of the fibre content and orientation. Cement and Concrete Composites **83**, 222–238 (2017).

105. Nunes, S., Pimentel, M. & Carvalho, A. Non-destructive assessment of fibre content and orientation in UHPFRC layers based on a magnetic method. Cement and Concrete Composites **72**, 66–79 (2016).

106. Pimentel, M. & Nunes, S. Determination of the fibre content and orientation in UHPFRC layers using NDT – application to the simulation of the behaviour of strengthened beams. in 7 (2016).

107. Shen, X. & Brühwiler, E. Influence of local fiber distribution on tensile behavior of strain hardening UHPFRC using NDT and DIC. Cement and Concrete Research **132**, 106042 (2020).

108. Li, L., Xia, J. & Galobardes, I. Magnetic Probe to Test Spatial Distribution of Steel fibres in UHPFRC Prisms. in 11 (2018).

109. Orange, G., Dugat, J. & Acker, P. Ductal®: New ultra high performance concretes. Damage resistance and micromechanical analysis. in 781–790 (2000).

110. Sawicki, B. & Brühwiler, E. Static behavior of reinforced UHPFRC beams with minimal cover thickness. in Proceedings of the 2IIS-UHPC - The 2nd International Interactive Symposium on Ultra-High Performance Concrete (2019).

111. Makita, T. & Brühwiler, E. Tensile fatigue behaviour of ultra-high performance fibre reinforced concrete (UHPFRC). Mater Struct **47**, 475–491 (2014).

112. Toutlemonde, F. et al. Recent experimental investigations on reinforced UHPFRC for applications in earthquake engineering and retrofitting. in UHPFRC 2013 - International Symposium on Ultra-High Performance Fibre-Reinforced Concrete 597–606 (2013).

113. Parsekian, G. A. et al. Static and Fatigue Tests on Ductal® UHPFRC Footbridge Sections. SP **253**, 273–290 (2008).

114. Makita, T. & Brühwiler, E. Tensile fatigue behaviour of Ultra-High Performance Fibre Reinforced Concrete combined with steel rebars (R-UHPFRC). International Journal of Fatigue **59**, 145–152 (2014).

115. Makita, T. & Brühwiler, E. Fatigue behaviour of bridge deck slab elements strengthened with reinforced UHPFRC. in Proceedings Bridge Maintenance, Safety, Management, Resilience and Sustainability vol. 1 1974–1980 (London, CRC Press/Balkema, 2012).

116. Meng, D., Zhang, Y. X. & Lee, C. K. Flexural fatigue behaviour of steel reinforced PVA-ECC beams. Construction and Building Materials **221**, 384–398 (2019).

117. Li, V. C. Engineered Cementitious Composites (ECC): Bendable Concrete for Sustainable and Resilient Infrastructure. (Springer-Verlag, 2019). doi:10.1007/978-3-662-58438-5.

118. Friedl, H., Río, O., Freytag, B. & Rodriguez, Á. ADVANCED BRIDGE MONITORING APPLICATION FOR ANALYSING ACTUAL STRUCTURAL PERFORMANCE OF UHPFRC CONSTRUCTIONS – WILD BRIDGE. in 6 (2010).

119. Schramm, N. & Fischer, O. Precast bridge construction with UHPFRC—Shear tests and railway bridge pilot application. Civil Engineering Design **1**, 41–53 (2019).

120. Barrias, A., Casas, J. R. & Villalba, S. Fatigue performance of distributed optical fiber sensors in reinforced concrete elements. Construction and Building Materials **218**, 214–223 (2019).

121. Gu, X., Chen, Z. & Ansari, F. Embedded Fiber Optic Crack Sensor for Reinforced Concrete Structures. SJ **97**, 468–476 (2000).

122. Sawicki, B., Bassil, A., Brühwiler, E., Chapeleau, X. & Leduc, D. Detection and Measurement of Matrix Discontinuities in UHPFRC by Means of Distributed Fiber Optics Sensing. Sensors **20**, 3883 (2020).

123. Bassil, A., Chapeleau, X., Leduc, D. & Abraham, O. Concrete Crack Monitoring Using a Novel Strain Transfer Model for Distributed Fiber Optics Sensors. Sensors **20**, (2020).

124. Yuan, J. & Graybeal, B. Bond of Reinforcement in Ultra-High-Performance Concrete. SJ **112**, 851–860 (2015).

125. Yoo, D.-Y., Kwon, K.-Y., Park, J.-J. & Yoon, Y.-S. Local bond-slip response of GFRP rebar in ultra-high-performance fiber-reinforced concrete. Composite Structures **120**, 53–64 (2015).

126. Lagier, F., Massicotte, B. & Charron, J.-P. Experimental investigation of bond stress distribution and bond strength in unconfined UHPFRC lap splices under direct tension. Cement and Concrete Composites **74**, 26–38 (2016).

127. Rocha, M., Michel, S., Brühwiler, E. & Nussbaumer, A. Very high cycle fatigue tests of quenched and self-tempered steel reinforcement bars. Mater Struct **49**, 1723–1732 (2016).

128. Charron, J.-P., Denarié, E. & Brühwiler, E. Permeability of ultra high performance fiber reinforced concretes (UHPFRC) under high stresses. Mater Struct **40**, 269–277 (2007).

129. Wang, K., Jansen, D. C., Shah, S. P. & Karr, A. F. Permeability study of cracked concrete. Cement and Concrete Research **27**, 381–393 (1997).

130. Graybeal, B. et al. International Perspective on UHPC in Bridge Engineering. Journal of Bridge Engineering **25**, 04020094 (2020).

131. Lamothe, S., Sorelli, L., Blanchet, P. & Galimard, P. Engineering ductile notch connections for composite floors made of laminated timber and high or ultra-high performance fiber reinforced concrete. Engineering Structures **211**, 110415 (2020).

132. Resplendino, J. & Toutlemonde, F. Designing and Building with UHPFRC. (Wiley-ISTE, 2011).

133. Spasojevic, A., Redaelli, D., Fernández Ruiz, M. & Muttoni, A. Influence of tensile properties of UHPFRC on size effect in bending. in Ultra High Performance Concrete (UHPC), Second International Symposium on Ultra High Performance Concrete 303–310 (2008).

134. Lohaus, L., Oneschkow, N. & Wefer, M. Design model for the fatigue behaviour of normal-strength, high-strength and ultra-high-strength concrete. Structural Concrete **13**, 182–192 (2012).

135. FIB. Model Code 2010. (2010).

136. Herwig, A. Reinforced concrete bridges under increased railway traffic loads. (École polytechnique fédérale de Lausanne, 2008).

137. Schläfli, M. & Brühwiler, E. Fatigue of Reinforced Concrete Elements without Shear Reinforcement. (1998).

138. Plos, M. et al. Structural assessment of concrete railway bridges: Non-linear analysis and remaining fatigue life. in Advances in Bridge Maintenance, Safety Management, and Life-Cycle Performance, Set of Book & CD-ROM 741–744 (CRC Press, 2006). doi:10.1201/b18175-314.

139. Hubbell, D. Design and Development of Glass-Fibre-Reinforced Polymer and Ultra-High-Performance Fibre-Reinforced Concrete Guideway Girders. (University of Toronto, 2017).

140. Parant, E., Rossi, P. & Boulay, C. Fatigue behavior of a multi-scale cement composite. Cement and Concrete Research **37**, 264–269 (2007).

141. Lappa, E. S. High strength fibre reinforced concrete: Static and fatigue behaviour in bending. (Delft University of Technology, 2007).

142. Behloul, M., Chanvillard, G., Pimienta, P., Pineaud, A. & Rivillon, P. Fatigue Flexural Behavior of Pre-cracked Specimens of Special UHPFRC. SP **228**, 1253–1268 (2005).

143. Naaman, A. E. & Hammoud, H. Fatigue characteristics of high performance fiber-reinforced concrete. Cement and Concrete Composites **20**, 353–363 (1998).

144. Ríos, J. D. & Cifuentes, H. Probabilistic fatigue analysis of ultra-high-performance fibre-reinforced concrete under thermal effects. MATEC Web of Conferences **165**, 12001 (2018).

145. Carlesso, D. M., de la Fuente, A. & Cavalaro, S. H. P. Fatigue of cracked high performance fiber reinforced concrete subjected to bending. Construction and Building Materials **220**, 444–455 (2019).

146. Shen, X. & Brühwiler, E. Biaxial flexural fatigue behavior of strain-hardening UHPFRC thin slab elements. International Journal of Fatigue **138**, 105727 (2020).

147. Hoffman, S. & Weiher, H. Innovative Design of Bridge Bearings by the use of UHPFRC. in Proceedings of the 3 rd International Symposium on UHPC and Nanotechnology for High Performance Construction Materials, Kassel, Germany. March 7 vol. 9 973–980 (2012).

148. Aaleti, S., Sritharan, S., Bierwagen, D. & Wipf, T. Structural Behavior of Waffle Bridge Deck Panels and Connections of Precast Ultra-High-Performance Concrete. Transportation Research Record: Journal of the Transportation Research Board **2251**, 82–92 (2011).

149. El-Hacha, R., Abdelazeem, H. & Cariaga, I. Performance of UHPC Crossarms for High-Voltage Transmission Lines. in Designing and Building with UHPFRC 447–466 (John Wiley & Sons, Ltd, 2013). doi:10.1002/9781118557839.ch30.

150. Sayed-Ahmed, M. & Sennah, K. Ultimate and fatigue strength of GFRP-reinforced, full-depth, precast bridge deck panels with zigzag-shape transverse joints filled with UHPFRC. in (2015).

151. Graybeal, B. Fatigue Response in Bridge Deck Connection Composed of Field-Cast Ultra-High-Performance Concrete. Transportation Research Record: Journal of the Transportation Research Board **2251**, 93–100 (2011).

152. Shao, X., Qu, W., Cao, J. & Yao, Y. Static and fatigue properties of the steel-UHPC lightweight composite bridge deck with large U ribs. Journal of Constructional Steel Research **148**, 491–507 (2018).

153. Oneschkow, N. Fatigue behaviour of high-strength concrete with respect to strain and stiffness. International Journal of Fatigue **87**, 38–49 (2016).

154. von der Haar, C. & Marx, S. Development of stiffness and ultrasonic pulse velocity of fatigue loaded concrete. Structural Concrete **17**, 630–636 (2016).

155. Grünberg, J., Lohaus, L., Ertel, C. & Wefer, M. Mehraxiales mechanisches Ermüdungsmodell von Ultra-Hochfestem Beton: Experimentelle und analytische Untersuchungen. Beton- und Stahlbetonbau **102**, 388–398 (2007).
156. von der Haar, C. & Marx, S. A strain model for fatigue-loaded concrete. Structural Concrete **1–9**, (2017).
157. Makita, T. & Brühwiler, E. Modelling of fatigue behaviour of bridge deck slab elements strengthened with reinforced UHPFRC. in Bridge Maintenance, Safety, Management And Life Extension 2472–2479 (Boca Raton, Crc Press-Taylor & Francis Group, 2014).
158. MacGregor, J. G., Jhamb, I. C. & Nuttall, N. Fatigue Strength of Hot Rolled Deformed Reinforcing Bars. JP **68**, 169–179 (1971).
159. D'Angelo, L., Rocha, M., Nussbaumer, A. & Brühwiler, E. S-N-P Fatigue Curves using Maximum Likelihood. in Proceedings of 7th European Conference on Steel and Composite Structures 705–706 (Brussels, ECCS European Convention for Constructional Steelwork, 2014).
160. Fisher, J. W. & Viest, I. M. Fatigue tests of bridge materials of the AASHTO road test. in Highway Research Board Special Report (1961).
161. Pfister, J. F. & Hognestad, E. High strength bars as concrete reinforcement, part 6: fatigue tests. (1964).
162. Rossi, P., Daviau-Desnoyers, D. & Tailhan, J.-L. Probabilistic numerical model of cracking in ultra-high performance fibre reinforced concrete (UHPFRC) beams subjected to shear loading. Cement and Concrete Composites **90**, 119–125 (2018).
163. NF P18-710. NF P18-710 Complément national à l'Eurocode 2 - Calcul des structures en béton : règles spécifiques pour les bétons fibrés à ultra-hautes performances (BFUP). (2016).

Curriculum Vitae

1. Personal information

Name:	**Bartłomiej**	**Surname:**	**Sawicki**
Birth date:	**14/09/1990**	**Nationality:**	**Polish**
ORCID:	**0000-0002-5632-3461**	**Google scholar ID:**	**EUH7zlgAAAAJ**
ResearchGate:	**researchgate.net/profile/Barttomiej_Sawicki**		
LinkedIn:	**linkedin.com/in/barteksawicki/**		

2. Education

***January 2017 – December 2020* Doctor of Science**; Swiss Federal Institute of Technology Lausanne EPFL (Switzerland), Doctoral Program in Civil and Environmental Engineering EDCE; PhD thesis title: 'Fatigue of reinforced UHPFRC members and monitoring of fatigue action effects on bridges'; advisor: prof. Eugen Brühwiler

***September 2013 – March 2015* Master of Science**; SUSCOS_M Erasmus Mundus Master Program, (Sustainable Constructions under natural hazards and catastrophic events): University of Liège (Belgium), Politehnica University of Timișoara (Romania), Luleå University of Technology (Sweden); Master thesis title: 'Structural Assessment of a Concrete Bridge. Probabilistic analysis of the shear resistance of the Kiruna Mine Bridge using in-situ material properties'; advisors: prof. Lennart Elfgren, prof. Thomas Blanksvärd

***October 2009 – July 2013* Bachelor of Science**; Warsaw University of Technology (Poland), Faculty of Civil Engineering; Bachelor thesis title: 'Numerical analyses of stress wave propagation for Impact-Echo testing procedure'; advisors: prof. Lesław Kwaśniewski, Tomasz Piotrowski, PhD

3. Employment history

***January 2017 – December 2020* Doctoral assistant;** Swiss Federal Institute of Technology Lausanne EPFL (Switzerland), the Laboratory of Maintenance and Safety of Structures (MCS); advisor: prof. Eugen Brühwiler

***July 2019 – October 2019* Seconded structural engineer**; Eiffage, Vélizy-Villacoublay, Grand Paris area (France), Engineering structures sector in Design and Engineering (BIEP) department / Innovation and materials modelling (DIRM) department

***July 2017 – August 2017* Seconded researcher**; Aalborg University (Denmark), Department of Civil Engineering, Reliability and Risk Analysis Research Group; advisor: prof. John Dalsgaard Sørensen

***February 2016 – December 2016* Assistant bridge designer;** Mosty Gdańsk sp. z o.o., Warsaw (Poland)

***September 2015 – January 2016* Site manager;** PRI DIAG-MOST sp. z o.o., Warsaw area (Poland)

***August 2013 – September 2013* Early Career Investigator at Short Term Scientific Mission**; University of Sheffield (United Kingdom), Department of Civil and Structural Engineering; advisor: prof. Ian Burgess

4. Institutional responsibilities

***January 2017 – December 2019* Early Stage Researcher;** Innovation and Networking for Fatigue and Reliability Analysis of Structures - Training for Assessment of Risk (INFRASTAR) Marie Skłodowska-Curie Action ITN 676139

***December 2012 – April 2014* Early Career Investigator;** Integrated Fire Engineering and Response (IFER) COST action TU0604

***October 2011 – July 2013* Founder member of the Numerical Modelling Scientific Group;** Warsaw University of Technology (Poland), Faculty of Civil Engineering

5. Supervision of students

February 2020 – July 2020 **Laboratory project;** Fabrication of new NDT devices with different magnetic probe sizes; Helen Krarup

September 2019 – April 2020 **Master thesis;** Fatigue Resistance of R-UHPFRC: Swiss Standard, Practice, Application and Research; Karin Hinkel (exchange student from Karlsruher Institut für Technologie (Germany))

February 2019 – July 2019 **Laboratory project;** Analysis of crack localization process in R-UHPFRC element under static loading; Gabriele Falconi and Enea Sala

September 2018 – January 2019 **Laboratory project;** Impact de la vibration sur les propriétés mécaniques du CFUP (Influence of vibrations on mechanical properties of UHPFRC); Loris Silva Brites and Pierre de Groot

February 2017 – July 2017 **Master thesis;** Examen et projet d'intervention sur le pont Eybrucke (Verification and intervention project on Eybrucke bridge); Morgan Lavanchy

February 2017 – July 2017 **Master thesis;** Etude approfondie de la sécurité structurale de ponts en beton (Advanced study on structural safety of concrete bridges); Aleksandar Trufinović

6. Teaching activities

8-12 April 2019 **Teaching assistant** INFRASTAR 1st training school, Nantes (France); Preparation and conduction of exercise sessions (with M. Nesterova) on use of probabilistic and statistical methods in structural monitoring; teacher: Franziska Schmidt, PhD

12-16 March 2015 **Teaching assistant** IFER 3rd training school, Lulea (Sweden); Preparation and conduction of exercise sessions (with M. Sitek) on use of FEM for structures under fire action; teacher: prof. Lesław Kwaśniewski

7. Prizes, awards, fellowships

January 2017 – December 2019 **Fellowship;** ESR fellow of INFRASTAR Marie Skłodowska-Curie ITN action project 676139

September 2013 – February 2015 **Fellowship;** Fellow of SUSCOS_M Erasmus Mundus Master project 520121-1-2011-1-CZ-ERA MUNDUS-EMMC

July 2013 **Prize;** Best Bachelor thesis in the Institute of Building Engineering founded by Dean of Civil Engineering Faculty of Warsaw University of technology, Mazovian Board of Civil Engineers and Polish Union of Building Engineers and Technicians

September 2011 – August 2012 **Scholarship;** Scholarship of Rector of Warsaw University of Technology for Best Students for Learning Achievements

8. Personal skills

Languages:	**Polish** (Native); **English** (Full professional proficiency, C1 CAE); **French** (Professional working proficiency, B2/C1); **Russian** (Professional working proficiency, B2)
Competencies:	**FEM** (Finite element modelling) – DIANA, ABAQUS, LS-DYNA, Robot, SOFiSTiK… **Programming** – MATLAB, C++

9. Publications

2020

B Sawicki, A Bassil, E Brühwiler, X Chapeleau, D Leduc; Detection and Measurement of Matrix Discontinuities in UHPFRC by Means of Distributed Fiber Optics Sensing; Sensors 20 (14), 3883

B Sawicki, E Brühwiler; Long-term strain measurements of traffic and temperature effects on an RC bridge deck slab strengthened with an R-UHPFRC layer; Journal of Civil Structural Health Monitoring, 1-12

B Sawicki, E Brühwiler, E Denarié; Inverse analysis of R-UHPFRC members to determine the flexural response under service loading and at ultimate resistance; Submitted to Journal of Structural Engineering

B Sawicki, E Brühwiler, A Bassil; Deformational behavior and damage mechanism of R-UHPFRC beam subjected to fatigue loading; Submitted to Materials and Structures

B Sawicki, E Brühwiler; Fatigue resistance of reinforced UHPFRC beams; Submitted to International Journal of Fatigue

B Sawicki, T Piotrowski, A Garbacz; Automation of concrete homogeneity assessment with Impact-Echo mulititransducer device; Submitted to Automation in Construction

B Sawicki, E Brühwiler; Influence of monitoring duration on measured traffic action effects on road bridges; Accepted for 10th International Conference on Bridge Maintenance, Safety and Management IABMAS 2020 (postponed to 2021)

K Hinkel, **B Sawicki**, E Brühwiler; Fatigue resistance of UHPFRC: research, practice and standardization in Switzerland; Accepted for BEI International Symposium on UHPC and Emerging Concrete 2020 (postponed to 2021)

2018/19:

B Sawicki, E Brühwiler; Static Behavior of Reinforced UHPFRC Beams with Minimal Cover Thickness; 2nd International Interactive Symposium on Ultra-High Performance Concrete

B Sawicki, E Brühwiler; Long term monitoring of a UHPFRC-strengthened bridge deck slab using strain gauges; 5th International Conference on Smart Monitoring, Assessment and Rehabilitation of Civil Structures SMAR 2019

M Ahmadivala, **B Sawicki**, E Brühwiler, T Yamalas, N Gayton, C Mattrand, A Orcesi; Application of Time Series Methods on Long-Term Structural Monitoring Data for Fatigue Analysis; 5th International Conference on Smart Monitoring, Assessment and Rehabilitation of Civil Structures SMAR 2019

B Sawicki, E Brühwiler, M Nesterova; Fatigue safety verification of a steel railway bridge using short term monitoring data; Sixth International Symposium on Life-Cycle Civil Engineering IALCCE 2018

2012-2015:

B Sawicki, J Pelczynski, L Kwasniewski; Benchmark example problems for beams at elevated temperatures; Applications of Structural Fire Engineering

B Sawicki, M Balcerzak, L Kwaśniewski, A Garbacz; Implementation and validation of numerical model of concrete plate for impact echo method; Theoretical foundations of civil engineering: 20 Polish-Ukraïnian transactions.

L Kwaśniewski, I Burgess, **B Sawicki**, P Krupa, M Sitek; Elastic-Plastic bending of beams. In: F Wald, I Burgess, L Kwaśniewski, K Horová, E Caldová, editors; Benchmark studies; Verification of numerical models in fire engineering. Prague, Czech Republic: CTU Publishing House, Czech Technical University in Prague